Computational Fluid Dynamic simulations of pulsatile flow in stenotic vessel models

Petter Holmlund

Master's Thesis in Engineering Physics, Department of Physics, Umeå University, 2013

Department of physics
Linnaeus väg 20
901 87 Umeå
Sweden
www.physics.umu.se

Computational Fluid Dynamic simulations of pulsatile flow in stenotic vessel models

Petter Holmlund
peho0022@student.umu.se

NOV 2013

Supervisors:
Anders Eklund Ph.D.
Sara Qvarlander M.Sc.

Examiner:
Krister Wiklund Ph.D.

Abstract

Within the past decades, Computational Fluid Dynamics (CFD) has become a useful tool for investigations of physiological flows (flows within the human body). The main advantage of utilizing CFD is that it can increase our understanding of these flows without the risks involved in complicated in vivo measurements, i.e. measurements within the living organism.

The purpose of this thesis was to investigate the CFD capabilities of *COMSOL Multiphysics*® (version 4.3b), and its CFD module, when applied to fluid flow in stenotic vessels (narrowed vessels). This was accomplished by investigating pressure variations within two axisymmetric artery stenosis models and a simplified model of the cerebral aqueduct, a canal connecting the third and fourth ventricles within the human brain, when being subject to pulsatile water flow (net flow in one direction). Laboratory experiments were performed in order to validate the CFD simulations and the hypothesis was that *COMSOL's* CFD module can be used to correctly describe fluid flow in stenotic vessels of arbitrary geometry. Both laminar flow simulations and turbulence model simulations were performed, separately, where the standard $k-\omega$ turbulence model, with wall functions, was utilized for the turbulence modelling. The work was also meant to yield further understanding of pressure behavior inside stenosed regions, building off of a previous study where the pressure distributions inside two rigid artery stenosis models were investigated experimentally when applying a pulsatile water flow. This thesis focused on investigating the pressure behavior along a central line through the stenosis models as well as variations in the total pressure drop over the stenosis, introduced due to the oscillating flow rate. In addition, the total pressure drop dependence on geometric properties was investigated, with a focus on the stenosis inlet and outlet as well as the stenosis diameter.

When comparing the experimental measurements with the CFD simulations, the results showed that neither the laminar nor turbulence model simulations yielded fully satisfying results when describing the pressure and velocity distributions along the stenosis models. The results led to the conclusion that a method that can solve both types of flow is required to fully describe the flow, for the problem investigated. To this end an additional turbulence model was tested: the low Reynolds $k-\varepsilon$ turbulence model. This model showed promise when predicting flow behavior along the entire stenosis models and warrants further investigation.

For all measurements and simulations, the results showed a considerable pressure decrease over the stenosis and a small pressure recovery downstream of the stenosis outlet. In addition, flow separation was observed at the stenosis outlet, for all flow rates and stenosis models tested. The peak-to-peak pressure drop, related to the flow rate oscillations, was shown to increase for increasing mean flow rates, despite keeping the inserted pulse volume and oscillation rate constant. However, the results also indicated that the magnitude of the pulsations through the stenosis models was severely diminished in the experiments, compared to what was expected, implying that the experimental measurement method should be evaluated further. The results indicated no major differences in the pressure drop for different stenosis inlet and outlet shapes, for the contractions/enlargements tested, though the CFD simulations implied that the pressure drop was strongly dependent on the stenosis diameter. Thus a correct determination (or estimation) of the stenosis diameter is of utmost importance when comparing the velocity and pressure distributions for different stenosis models.

Sammanfattning

De senaste decennierna har Computational Fluid Dynamics (CFD) blivit ett användbart verktyg vid studier av fysiologiska flöden (flöden i människokroppen). En fördel med CFD är möjligheten att öka vår förståelse för dessa flöden utan att behöva utföra komplicerade mätningar i känsliga områden i kroppen.

Syftet med detta projekt var att undersöka hur väl *COMSOL Multiphysics*® (version 4.3b), och dess CFD-modul, kan tillämpas vid beskrivning av flöden i kärl med stenoser (förträngda kärl). Detta uppnåddes genom att undersöka tryckfördelningarna i två axisymmetriska modeller av förträngda artärer samt en förenklad modell av den cerebrala akvedukten, en kanal som förbinder tredje och fjärde ventriklarna i hjärnan, när de utsattes för ett pulserande vattenflöde (nettoflöde i en riktning). Laborationsexperiment utfördes för att kunna utvärdera CFD-simuleringarna och hypotesen var att CFD-modulen i *COMSOL* kan användas till att beskriva vätskeflöden i förträngda kärl av godtycklig geometri på ett korrekt sätt. Simuleringar genomfördes både för laminärt och turbulent flöde, var för sig, där turbulens hanterades med en standardmodell av typen $k-\omega$, med wall functions. Arbetet var också tänkt att ge ytterligare insikt i hur trycket förändras i stenosregioner och utgjorde en fortsättning på en tidigare vetenskaplig studie där ett pulserande vattenflöde tillämpades på två rigida artärstenosmodeller varvid trycket undersöktes experimentellt. Detta examensarbete fokuserade på att beskriva trycket längs med stenosmodellerna och variationerna i det totala tryckfallet över modellerna, som det oscillerande flödet gav upphov till. Slutligen jämfördes det totala tryckfallet för olika stenosgeometrier, där stenosens in- och utgång samt diameter låg i fokus.

När experimenten och CFD-simuleringarna jämfördes så visade resultaten att varken den laminära modellen eller turbulensmodellen som tillämpades gav helt tillfredställande resultat vad gäller beskrivningen av tryck- och hastighetsfördelningarna längs med stenosmodellerna. Resultaten antydde att det undersökta problemet kräver en CFD-modell som kan hantera både laminärt och turbulent flöde. Testsimuleringar utfördes med en så kallad low Reynolds number-modell, av typen $k-\varepsilon$, som visade lovande resultat vad gäller återskapandet av flödesbeteendet hela vägen genom stenosmodellerna och borde undersökas ytterligare.

För samtliga mätningar och simuleringar så visade resultaten på en tydlig tryckförlust över stenosen, samt en liten återhämtning i trycket nedströms stenosutgången. Förutom detta så observerades flödesseparation vid stenosutgången för samtliga modeller och volymflöden. Variationerna i det totala tryckfallet över stenosmodellerna, som orsakades av det pulsativa flödet, ökade vid ökat medelflöde trots att volymen på pulserna och pulsationshastigheten hölls konstanta. Resultaten visade dock på en tydlig minskning av pulsationerna i de experimentella mätningarna, jämfört med den förväntade magnituden, vilket antyder att den experimentella metoden måste utvärderas ytterligare. Resultaten visade inte på någon större förändring i det totala tryckfallet vid ändring av stenosens ingångs- och utgångsgeometrier, för de in- och utgångar som testades i detta arbete, men CFD-simuleringarna visade dock på ett starkt beroende mellan tryckfallet och stenosdiameterns storlek. Detta resultat antyder att en korrekt uppskattning av diametern på stenosen är av yttersta vikt för att kunna jämföra olika stenosmodeller med avseende på hastighets- och tryckfördelningar.

Preface

This Master's thesis work was done in collaboration with the Department of Biomedical Engineering and Informatics at Umeå University Hospital, Sweden, and I would like to thank my supervisors at the department, Sara Qvarlander and Anders Eklund, for their support and useful input during the work with this thesis. I also thank Professor Michael Henein at the Heart Center, Umeå University Hospital, for providing the catheter tip pressure sensors used for the experimental measurements. Thanks also to Krister Wiklund at the Department of Physics, Umeå University, for taking the time to read my report and being my examiner.

Table of Contents

1 Introduction

This section provides a brief introduction to the subject of this thesis and the motivations behind it. Specific goals are provided in a list for easy accessibility.

1.1 Background

Atherosclerosis of the arteries is one of the main causes of death in the world today [1, 2]. It is caused by plaque forming at the walls of the artery, creating a narrowing of the vessel (artery stenosis). Such obstructions can eventually lead to cardiovascular disease such as myocardial infarction and stroke, if the blood flow is severely reduced. The formation of plaque is believed to be connected to wall shear stress at the vessel walls [3], which is directly related to the dynamics of blood flow, making investigations of hydrodynamic properties in stenosis regions an important area of research. Studies of flow and pressure distributions in the arteries could give us information of where stenoses are likely to appear but also how to prevent plaque formation. A recent study theorized that the hydrodynamic pressure increase on the artery walls during regular exercise could have a positive mechanical effect on soft plaque similar to treatment by percutaneous coronary intervention [4]. The problem of obstructed flow is not only limited to the circulatory system of blood, but also poses a threat in other physiological systems. The circulation of cerebrospinal fluid (CSF) within the brain is one such system, where obstructed flow might lead to non-communicating hydrocephalus (water on the brain) [5], and altered CSF dynamics are believed to relate to normal pressure hydrocephalus [6].

One problem with physiological flow systems is the difficulty of performing pressure and velocity measurements in vivo, especially when looking for small spatial variations. Computational Fluid Dynamics (CFD) has become a promising tool for research within the field of bio-fluid mechanics, since it allows for fluid flow properties to be approximated numerically without having to resort to complicated in vivo measurements. CFD simulations of physiological flows have been performed on several occasions in the past, yielding promising results both within studies of artery stenosis [7, 8] as well as studies of the CSF-system [9].

1.2 Purpose

The Department of Biomedical Engineering and Informatics at Umeå University Hospital conducts research and development in medical technology in close collaboration with medical researchers. Among other projects, one research group within the department is involved in research of the CSF-circulation where flow measurements are performed by Magnetic Resonance Imaging (MRI). While fluid velocity is easily measured, detailed knowledge about pressure gradients is more difficult to obtain. A specific area of interest is the narrow passage connecting the third and fourth ventricles within the brain, known as the cerebral aqueduct (or the aqueduct of Sylvius). The research group is now searching for ways to describe hydrodynamic properties, such as pressure gradients, for patient specific geometries with the help of proper software. One of the tools up for investigation is *COMSOL Multiphysics*® (version 4.3b) and its CFD module.

This thesis work was meant to act as a first step in evaluating *COMSOL*'s CFD module by performing CFD simulations of fluid flow through stenosis models of simple geometry and comparing the results with acquired experimental data. The hypothesis was that *COMSOL*'s CFD module can be used to accurately describe physiological flows in (stenotic) vessels of arbitrary geometry. The thesis was also meant as a continuation of a recent project in collaboration with the Heart Centre and the Department of Public Health and Clinical Medicine, at Umeå University Hospital, where two artery stenosis models being subject to pulsatile fluid flow were investigated in order to characterise the pressure behavior in the proximity of the stenoses [4]. The experimental method of that study was used to perform additional measurements on a new stenosis model, representing the cerebral aqueduct, as well as recreating the acquired results for the artery stenosis models. The results from these measurements served as a basis for comparison with the CFD simulations.

1.3 Objective

The main objective of this thesis was to investigate the fluid pressure behavior in three axisymmetric stenosis models subjected to pulsatile water flow by comparing experimental measurements with CFD simulations, focusing on the following properties:

- Investigate the pressure behavior inside the stenosis models at predetermined points along the symmetry axis.
- Pulsatile flow effects.
- Differences in the pressure drop, over the stenosis, for different stenosis shapes.

To achieve this aim, the work was divided into separate stages:

1. Perform experimental measurements of fluid flow through two axisymmetrical artery stenosis models of stenosis diameter 1.0 mm and 1.5 mm with rigid walls and identical inlet and outlet shapes.
2. Perform CFD simulations of pulsatile flow through the artery models and compare the results with the experimental measurements and with previously measured bench data [4].
3. Perform experimental measurements on a simplified aqueduct model, with differing stenosis inlet and outlet shapes.
4. Compare the experimental measurements for the aqueduct model with new CFD simulations.

2 Theory

This chapter includes the theory relevant to this thesis work. It contains general theory of fluid dynamics and CFD, such as the Navier-Stokes equations and turbulence model theory. Common hydrodynamic relations used within the study of blood flow (hemodynamics) are presented, and the pressure drop over a stenosis is approximated. The chapter concludes with theory regarding the Finite Element Method.

2.1 Hemodynamics

Hemodynamics is the study of blood flow in biomechanical systems. It is a complicated science, partly due to the composition of blood (consisting of both blood cells and plasma) but also due to the geometric complexities of the circulatory system and the pulsatile nature of blood flow. Thus for many hemodynamic studies, approximations are made in order to apply simple hydrodynamic relations to describe the flow of blood. For one, even though blood behaves like a non-Newtonian fluid, in many situations it is sufficient to approximate it as Newtonian. Blood flow is also commonly modeled as incompressible, i.e. local density variations are neglected, and approximated as flow through cylindrical tubes/pipes. These assumptions may seem crude, but help describe the flow, pressure and resistance within the blood vessels in a convenient way that can yield qualitative information about blood flow behavior. In this thesis, only incompressible Newtonian fluid flow through rigid vessels is considered.

2.1.1 The Reynolds number

As a natural phenomenon in fluids, the characteristics of the flow can change drastically under certain conditions, for example at really high velocities. Various quantities can be used to characterize flow in different situations. One of the most well known, and widely used, is the Reynolds number. This dimensionless quantity relates the inertial forces to the viscous forces within a fluid, and is defined as

$$Re = \frac{inertial\ forces}{viscous\ forces} = \frac{\rho w L}{\mu} \qquad (2.1.1)$$

where ρ is the fluid density, μ the dynamic fluid viscosity, w the mean velocity of the fluid and L a typical length scale of the flow (e.g. the hydraulic diameter for pipe flow). For low Reynolds numbers, the inertial forces are negligible compared to the viscous forces and flow is characterized by smooth and organized layer motion [10]. Flow of this kind is said to be within the laminar regime. At higher Reynolds numbers, inertial forces dominate the viscous forces, creating chaotic eddies, vortices and other flow instabilities of widely different length and time scales [10]. In this regime the flow is referred to as turbulent and is much more difficult to predict. At moderately high Reynolds numbers, the flow starts changing from laminar to turbulent. This regime is known as the transitional regime, where the flow might show characteristics of both laminar and turbulent flow. For a cylindrical pipe, the transition from laminar to turbulent flow usually occurs for Reynolds numbers slightly above 2000 (see *Table 2.1-1*) but it depends on problem specifics such as surface roughness and geometry variations. In summary, the Reynolds number is helpful in order to get a sense of the fluid flow behavior.

Table 2.1-1: Flow characterization within a pipe by the Reynolds number [11].

Reynolds number	Flow regime
< 2000	Laminar flow
> 4000	Turbulent flow
2000< Re <4000	Transitional flow

2.1.2 Basic hydrodynamics

For isothermal fluid flow, i.e. flow of constant temperature, through systems of vessels/pipes, the physical quantities of interest are most often the velocity and pressure of the fluid, and their respective distributions. A first estimation of the average velocity behavior can be found by measuring the volumetric flow rate (or just flow rate) going through the system. The volumetric flow rate is the volume of fluid passing a cross-sectional area per unit time, and can be described by

$$Q = wA \tag{2.1.2}$$

where A is the cross-sectional area of the vessel. For incompressible fluid flow, the mass flow rate, and thus the (volumetric) flow rate, can be considered constant within the vessel due to mass conservation. For a vessel with a local stenosis, (2.1.2) yields

$$Q = w_1 A_1 = w_2 A_2 \tag{2.1.3}$$

where w_1 is the mean velocity in the vessel, $A_1 = \pi d_1^2/4$ is the vessel cross-sectional area, w_2 is the mean velocity inside the stenosis region and $A_2 = \pi d_2^2/4$ is the stenosis cross-sectional area (see *Figure 2.1-1*). Thus once the flow rate is known, the mean flow velocities in different parts of the flow system can be determined, if the corresponding cross-sectional areas are known. This is also useful when approximating the Reynolds number in different parts of the flow system.

For frictionless flow, the total pressure along a streamline (curve instantaneously tangent to the velocity vector) fulfills the following relation

$$p_1 + \frac{\rho u_1^2}{2} + \rho g h_1 = p_2 + \frac{\rho u_2^2}{2} + \rho g h_2 \tag{2.1.4}$$

where p is the pressure at a given point along a streamline, u is the instantaneous velocity, h is the corresponding height of the point in question and g is the gravitational acceleration at sea level. The second term on both sides of (2.1.4) is often referred to as the dynamic pressure, describing the kinetic energy of the fluid. (2.1.4) is known as the Bernoulli equation, which is valid for incompressible flow and compressible flow of low velocity. Bernoulli's equation describes the shift from kinetic to potential energy (dynamic to static pressure) for frictionless fluid flow. Equation (2.1.4) is commonly generalized to include the cross-sectional mean flow velocities, w_1 and w_2, instead of the instantaneous ones [12].

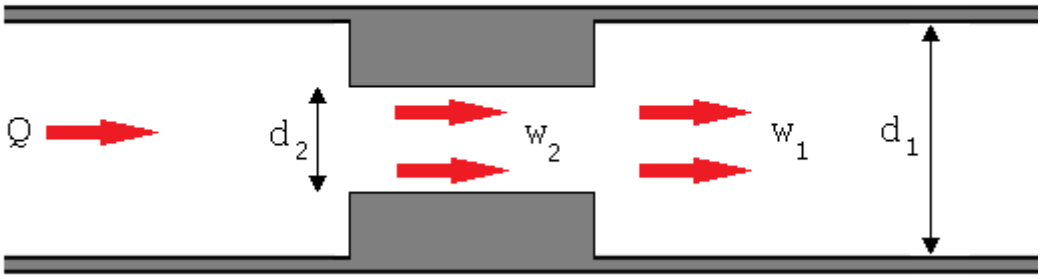

Figure 2.1-1: A pipe with a local stenosis. Here d is the diameter and the mean velocity is denoted w, which is higher in the smaller part of the pipe ($w_1 < w_2$) due to conservation of the flow rate Q throughout the channel.

2.1.3 Flow resistance in straight channels

For flow within a pipe (or vessel), frictional losses are generated due to viscosity of the fluid and a no-slip condition at the walls. Because of this flow resistance, the Bernoulli equation must be complemented by irreversible pressure losses to fully describe the pressure changes for pipe flow. The pressure drop for fully developed flow in a straight channel can be described by the Darcy-Weisbach equation

$$\Delta p = f_D \frac{L}{D} \frac{\rho w^2}{2} \tag{2.1.5}$$

where L is the length of the pipe, D is the hydraulic diameter of the pipe and f_D is the Darcy friction factor. The friction factor is dependent on the wall roughness of the pipe and the Reynolds number of the flow. For fully developed laminar flow in a smooth cylindrical pipe, known as Poiseuille flow, the pressure drop is described by the Poiseuille formula

$$\Delta p = \frac{128 \mu L}{\pi D^4} Q. \tag{2.1.6}$$

Thus, for laminar flow, the friction factor is $f_D = 64/Re$, and the pressure drop is linearly dependent on the flow rate. For higher Reynolds numbers (other flow regimes) the friction factor can be determined by using Moody diagrams [13]. For fully turbulent flows, the pressure drop exceeds that of laminar flow [14].

For flow through annulus geometries, the pressure drop is a bit more complicated. The pressure drop for fully developed flow in a straight annulus can be found to be

$$\Delta p = \frac{8 \mu Q L}{\pi (r_2^2 - r_1^2)} \left[\frac{\ln\left(\frac{r_2}{r_1}\right)}{(r_1^2 + r_2^2) \ln\left(\frac{r_2}{r_1}\right) - (r_2^2 - r_1^2)} \right] \tag{2.1.7}$$

$$r_1 \leq r \leq r_2$$

where r_1 and r_2 are the smaller and larger radius, respectively (see the derivation in *Appendix A*). This expression for the pressure drop is only valid for laminar flow.

2.1.4 Enlargements and contractions

When flow encounters obstructions, the pressure will further decrease. In the case of sudden contractions and enlargements of the pipe, the fluid will not be able to follow the vessel walls, resulting in flow separation (see *Figure 2.1-2* and *Figure 2.1-3*). This results in the dissipation of mechanical energy due to the formation of a recirculation region just downstream of the point of flow separation [15]. The pressure losses, for contractions/enlargements, can be described as part of the dynamic pressure

$$\Delta p = k_{dis}\frac{\rho w^2}{2} = k_{dis}\frac{8\rho Q^2}{\pi^2 D^4}, \tag{2.1.8}$$

where k_{dis} is a pressure loss coefficient that is dependent on the shape of the contraction or enlargement, the Reynolds number of the flow, as well as the stenosis to vessel diameter ratio [16]. This coefficient is usually determined empirically, but can be approximated in certain cases.

For sudden enlargements, the discharge coefficient can be approximated with the Borda-Carnot relation [17] resulting in the following expression for the discharge coefficient

$$k_{dis} = \left(1 - \frac{A_1}{A_2}\right)^2 \tag{2.1.9}$$

where A_1/A_2 is the ratio of the cross-sectional areas of the stenosis region and the vessel. The approximation of (2.1.9) is best applied for flows of higher Reynolds numbers, i.e. turbulent flows [16][1].

The coefficient for sudden contractions is different than the one for enlargements. Due to flow separation the flow area becomes even smaller than the cross-sectional stenosis area downstream of the contraction (*Figure 2.1-3* and *Figure 2.1-4*). The point of minimum area for the flow is known as the vena contracta, and it is the expansion of the flow from this point, where flow decelerates to fulfill (2.1.3), that stands for the biggest loss of mechanical energy [19]. Thus the discharge coefficient depends on the ratio of the flow area at the vena contracta and the cross-sectional area of the stenosis. However, the discharge coefficient will still depend on the ratio of the stenosis and vessel cross-sectional areas since this relationship affects the resulting flow area at the vena contracta.

In addition to the irreversible pressure drop in contractions and enlargements, the pressure also changes due to conversions between static and dynamic pressure. In the case of contractions, the velocity increases to fulfill (2.1.3), resulting in a reversible pressure drop. For enlargements, the velocity decreases, resulting in pressure recovery (unless the discharge losses are bigger than the pressure gained from the kinetic to static pressure conversion), hence the word reversible.

[1] For a thorough investigation of pressure losses due to enlargements/contractions for turbulent pipe flow, the book *Pipe flow: A practical and comprehensive guide* [18] is suggested.

Equation (2.1.8), together with (2.1.6) and (2.1.7) for Poiseuille and annulus flow respectively, shows that the total irreversible pressure drop is dependent on the flow rate in a non-linear fashion. Combining these equations yields

$$\Delta p = k_1 Q^2 + k_2 Q. \tag{2.1.10}$$

where everything except for the flow rate has been included in the coefficients k_1 and k_2. The form of (2.1.10) is the same for both cylindrical and annulus pipe flow, but with different coefficients. It is important to note that the coefficients will be dependent on the Reynolds number, thus it will vary for different Reynolds number regions[2]. In addition, for the specific problem of a stenosis, where both a contraction and an enlargement is present, the flow effects at the stenosis inlet also affect the pressure drop (or the discharge coefficient) at the outlet, due to the non-linearity of the fundamental equations of fluid dynamics. This further complicates the behavior of the pressure losses compared to cases where only an enlargement or a contraction is present.

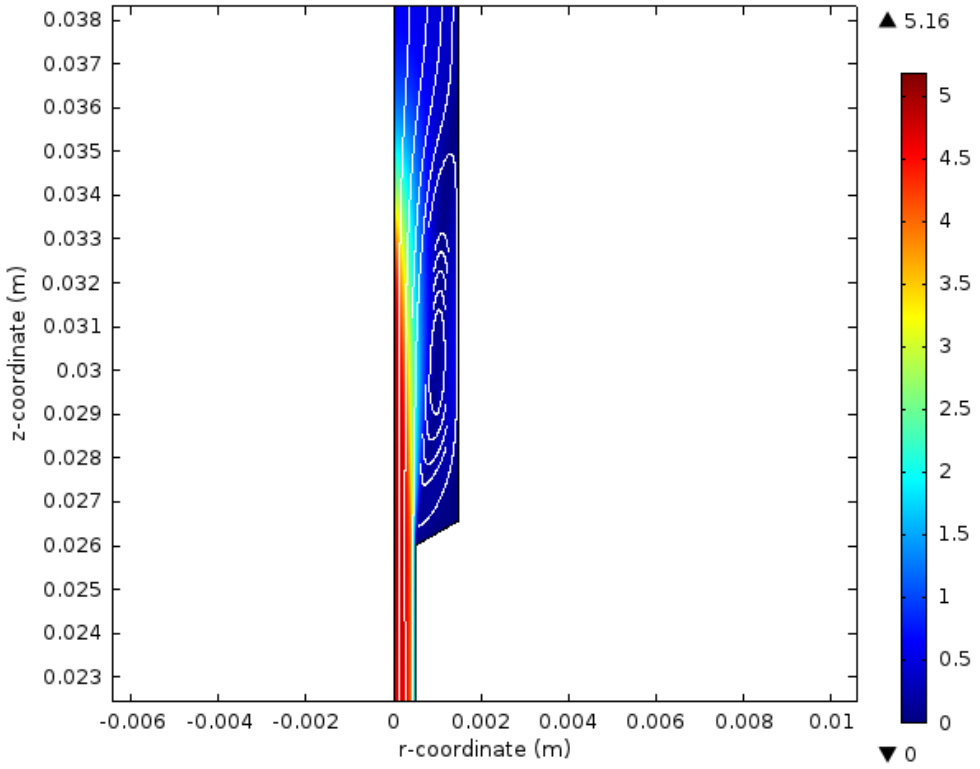

Figure 2.1-2: Flow separation due to the enlargement of a pipe. Velocity field (colored surface) and velocity stream lines (white lines) are presented for a cross-section of a 2D-axisymmetric geometry (a cylinder). The direction of the flow is in the positive z-direction and the color scale represents the velocity magnitude where red is high and blue is low.

[2] To find out more about pressure drops for laminar flow in enlargements, the following articles are recommended: *Pressure drop coefficient of laminar Newtonian flow in axisymmetric diffusers* [16] and *A general correlation for the local loss coefficient in Newtonian axisymmetric sudden expansions* [20].

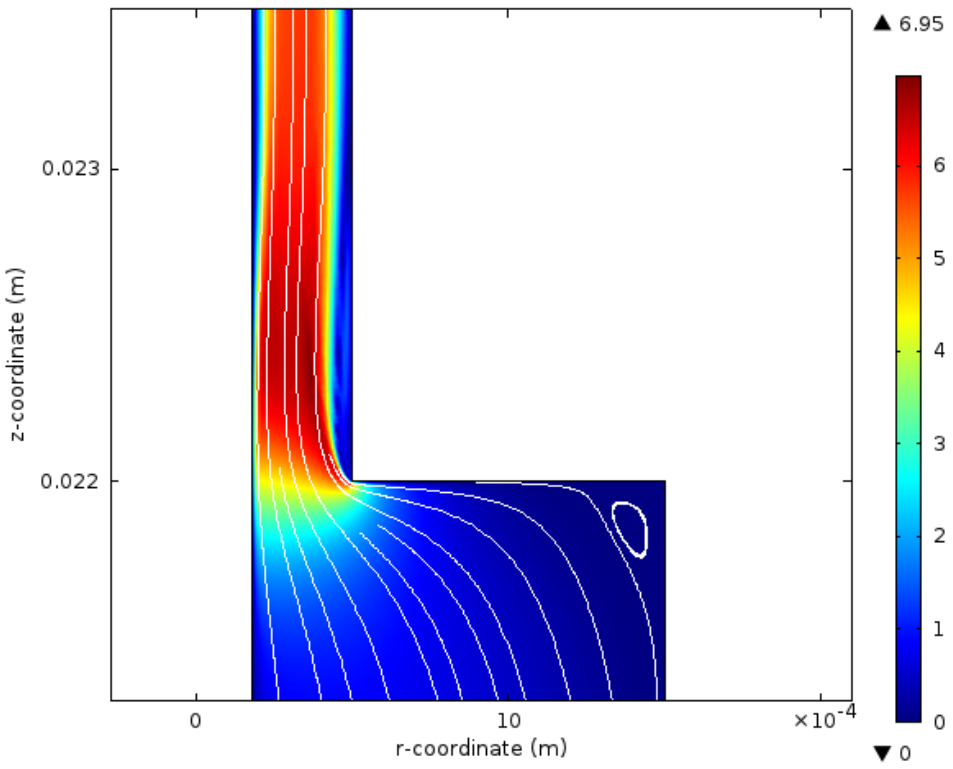

Figure 2.1-3: Flow separation due to the contraction of a pipe. Velocity field (color) and velocity stream lines (white lines) are presented for a cross-section of a 2D-axisymmetric geometry (an annulus). The direction of the flow is in the positive z-direction and the color scale represents the velocity magnitude where red is high and blue is low.

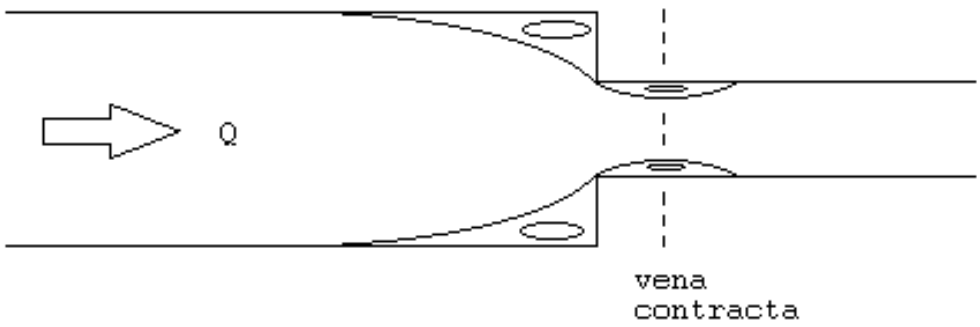

Figure 2.1-4: Flow separation, and vortex formation, due to the contraction of a pipe. The point of smallest flow area is the vena contracta. Q is the flow rate.

2.1.5 Velocity profiles

For fluid flow within a pipe, the velocity profile is an important property of interest. For fully developed flow in a cylindrical pipe of constant diameter, the corresponding expressions for the velocity profiles are

$$u_{laminar}(r) = u_{max}\left(1 - \left(\frac{r}{R}\right)^2\right)$$
$$u_{turbulent}(r) = u_{max}\left(1 - \frac{r}{R}\right)^{1/7} \qquad (2.1.11)$$

for laminar and turbulent flow respectively, where $u_{max} = 2u_{mean}$ for laminar flow and $u_{max} \approx 1.22u_{mean}$ for turbulent flow. The laminar profile can be derived by fundamental principles of fluid flow and corresponds to that of Poiseuille flow. The velocity profile for turbulent flow seen in (2.1.11), sometimes referred to as the $1/7^{th}$ power law, is an empirically determined relation [12] and is only a model (one out of many). It is one of the most commonly used models, but depending on the situation, other models might describe the velocity profile for turbulent flow more accurately.

The velocity profile for fully developed laminar flow in an annulus can be found to be

$$u(r) = \frac{2Q}{\pi(r_2^2 - r_1^2)} \frac{(r_2^2 - r_1^2)\ln\left(\frac{r}{r_1}\right) - (r^2 - r_1^2)\ln\left(\frac{r_2}{r_1}\right)}{(r_1^2 + r_2^2)\ln\left(\frac{r_2}{r_1}\right) - (r_2^2 - r_1^2)} \tag{2.1.12}$$

(see *Appendix A* for the derivation). The acquired expression for the annulus velocity profile has its maximum slightly shifted towards the wall of smaller radius, which is in contrast to cylindrical pipe flow where the maximum is in the centre of the pipe. The turbulent velocity profile has no well known formulation for flow within an annulus.

2.1.6 Pulsatile flow

Pulsatile flow can be described by the dimensionless quantity known as the Womersley number. This quantity relates the oscillatory frequency of the pulsatile flow to viscous effects [21] and is defined as

$$\Omega = a\sqrt{\frac{\omega\rho}{\mu}} = a\sqrt{\frac{\omega}{\nu}} \tag{2.1.13}$$

where ω is the angular frequency of the oscillations, a a typical length scale (commonly the radius for a pipe) and $\nu = \rho/\mu$ is the kinematic viscosity. The Womersley number appears when the linearized Navier-Stokes equations are solved for oscillatory, laminar, pipe flow [21]. The Womersley number determines how much the flow in a pipe is affected by the oscillation frequency of the pulsations. For a Womersley number lower than unity, the flow is almost fully developed at each instant of the oscillatory cycle, and the flow rate and the pressure gradient driving the flow ($\Delta p/L_{pipe}$) will be changing almost in phase. The flow is then very close to oscillatory Poiseuille flow, which means that the velocity profile can be described by the first equation of (2.1.11) at each instant in time corresponding to the instantaneous pressure gradient. With increasing values of the Womersley number, the flow and pressure gradient become more and more out of phase due to inertia of the fluid. Furthermore the flow does not have time to reach its fully developed form at each instant in time, resulting in a damping of the flow rate oscillations compared to that of oscillatory Poiseuille flow under the same pressure gradient variations [21].

When adding symmetric pulsations to a constant stream, there will be a net flow in the direction of constant flow. If the pulsatile flow rate is known, then the maximum and minimum flow rates can be used to approximate the difference in the pressure drop for a system, over an oscillatory cycle. For a pulsation amplitude of ΔQ, equation (2.1.10) gives the maximum and minimum pressure drops over a stenosis (according to the systolic and diastolic stages respectively)

$$\Delta p = k_1(Q + \Delta Q)^2 + k_2(Q + \Delta Q)$$
$$\Delta p = k_1(Q - \Delta Q)^2 + k_2(Q - \Delta Q). \quad (2.1.14)$$

Taking the difference of these two equations yields

$$\Delta p_{sys} - \Delta p_{dia} = 4k_1 \Delta Q Q + 2k_2 \Delta Q. \quad (2.1.15)$$

Equation (2.1.15) shows that the pressure drop oscillates with an amplitude whose size is depending on the mean flow rate Q, according to the first term on the right hand side (RHS). Thus for increasing (mean) flow rates, the size of the variations in pressure drop (over one cycle) will also increase, despite keeping the size of the flow rate pulsations constant ($\Delta Q = const$). It is worth noting that k_1 and k_2 are dependent on the Reynolds number, which means that the flow rate dependency is different for different Reynolds number regions. Observe that (2.1.15) only holds as long as the oscillatory flow rate is of the same amplitude for all flows, i.e. the whole pulse is pressed through the stenosis for all flows, which is the case for a rigid tube but not necessarily so when dealing with elastic vessels. Since (2.1.15) does not include any time-dependency, the equation might also be affected for pulsatile flow of sufficiently high frequency, where the flow deviates far from oscillating Poiseuille flow ($\Omega > 1$).

2.1.7 Limitations of analytical theory

While the theory described above is useful, it only describes parts of the flow behavior, thus it is only approximate. To get a full description, the fundamental governing equations of fluid flow have to be solved. These equations are highly non-linear and can seldom be solved analytically. This is why numerical methods are used for most fluid flow problems, hence the need for CFD.

2.2 The Governing Equations

The motion of a fluid is governed by the Navier-Stokes system of equations. They are derived by applying the three laws of conservation to fluid flow. In component form, these equations can be written as

$$\frac{\partial \rho}{\partial t} + \frac{\partial (\rho u_j)}{\partial x_j} = 0 \tag{2.2.1}$$

$$\rho \left(\frac{\partial u_i}{\partial t} + u_j \frac{\partial u_i}{\partial x_j} \right) = -\frac{\partial p}{\partial x_i} + \frac{\partial \tau_{ji}}{\partial x_j} + f_i \tag{2.2.2}$$

$$\rho \frac{\partial \varepsilon}{\partial t} + \rho u_j \frac{\partial \varepsilon}{\partial x_j} + p \frac{\partial u_j}{\partial x_j} = \tau_{ji} \frac{\partial u_i}{\partial x_j} - \frac{\partial q_j}{\partial x_j} + \rho r \tag{2.2.3}$$

where ρ is the fluid density, x_i the position vector components, u_i the components of the velocity vector, p the pressure, τ_{ij} the viscous stress tensor, ε the internal energy per unit mass, q_i the heat flux, r the heat supply per unit mass, and f_i represents body forces per unit volume acting on the fluid, such as gravity forces. The index j indicates summation over all components. The first of these equations results from conservation of mass and is known as the continuity equation. The second is a set of equations (one equation for each dimension) that describes linear momentum conservation; this equation is often referenced as the Navier-Stokes equation(s). Finally the third equation describes energy conservation. In 3D, this system involves six scalar variables (ρ, p, ε and a velocity component u_i for each dimension) and only five equations. To close the system, an equation of state is needed. This equation of state relates the pressure to the density and temperature

$$p = p(\rho, T) \tag{2.2.4}$$

where T is the temperature of the gas/fluid. Since the internal energy per unit mass is related to temperature

$$\varepsilon = \varepsilon(\rho, T) \tag{2.2.5}$$

it can be replaced and T becomes the new unknown variable. The problem boils down to six unknowns (ρ, p, T and all u_i) and six equations (2.2.1-2.2.4). To fully describe the motion of fluid flow, for a specific problem, the Partial Differential Equations (PDEs) of (2.2.1-2.2.3) must be complemented with the appropriate boundary and initial conditions.

Under certain circumstances the governing equations can be simplified. In reality, fluids and gases are compressible, but for velocities much lower than the speed of sound within the medium, fluid flow can be considered incompressible (i.e. local density variations are neglected). When dealing with incompressible flows of Newtonian fluids, the momentum and mass equations above reduce to

$$\frac{\partial u_j}{\partial x_j} = 0 \tag{2.2.6}$$

$$\rho\left(\frac{\partial u_i}{\partial t} + u_j \frac{\partial u_i}{\partial x_j}\right) = -\frac{\partial p}{\partial x_i} + \mu \frac{\partial^2 u_i}{\partial x_j \partial x_j} + f_i. \tag{2.2.7}$$

Equation (2.2.6) implies that the mass flux for a volume element must be equal to zero. The left hand side (LHS) of (2.2.7) describes the acceleration of the fluid, while the RHS describes pressure, viscous, and other body forces. The second term on the RHS of (2.2.7) is the resulting viscous stress when assuming that the shear stress is linearly dependent on the velocity gradients (which is the case for a Newtonian fluid) and the dynamic viscosity of the fluid. The non-linear term in (2.2.7) is the convective acceleration, which is the acceleration in space that is time-independent, such as acceleration due to changing geometry. Because of the constant density, the equation of energy conservation is decoupled from the mass and momentum equations, thus (2.2.6) and (2.2.7) are enough to describe the fluid motion if temperature effects are neglected, which is the case in this thesis. The reduced system, (2.2.6) and (2.2.7), consists of four equations (one for mass and three for momentum conservation) and four unknowns ($\vec{u}, p$).

2.2.1 Boundary Conditions

Two of the most common boundary conditions are the Dirichlet and the Neumann boundary conditions. The former specifies the value of a variable at a boundary while the latter specifies the derivatives of a variable. They are both special cases of the more general Robin boundary condition, which is a combination of the two [22]. Common boundaries to fluid flow are walls confining the fluid, inlet/outlet boundaries and free surfaces (the latter is beyond the scope of this thesis). Since the fluid cannot flow through walls, the normal component of fluid velocity, relative to the wall, must be zero there. The tangential component of velocity relative to the wall, for viscous fluid flow, must also be zero, which is a result of friction between the fluid and the wall due to the viscosity of the fluid. This is known as the no-slip condition, which is a Dirichlet condition on the velocity ($\vec{u} = \vec{u}_{wall}$).

For CFD simulations, the inlet and the outlet conditions are most often specified either by velocity, mass flow rate, or pressure. For most fluid flow problems, at least one of these properties is known. Velocity conditions are usually inlet conditions, whereas pressure is commonly applied at the outlet of a system [23]. Mass flow can be applied when the velocity profile is unknown. Another CFD boundary condition is the symmetry boundary condition. Since the flow variables must be continuous over the symmetry plane, the velocity normal to this plane must vanish there. In addition, the normal derivative of the velocity component along the symmetry plane must be zero as well (no tangential viscous stress at the plane of symmetry) [24].

2.3 Turbulence modeling

While the Navier-Stokes equations (2.2.7) are still valid for turbulent flow, it is not feasible to solve these equations exactly (in most cases) due to the vastly different length and time scales present. Thus finding a solution using Direct Numerical Simulations (DNS), even for simple geometries/problems, can become difficult once turbulence is involved. An additional problem occurs when trying to approximate the solution to a fluid flow problem by any laminar physics model. While all laminar flow models utilize the Navier-Stokes equations, they only yield the same result as DNS when all the different length scales are resolved, i.e. the computational mesh is fine enough. If all scales are not resolved, there is a risk that the solution acquired is physically unrealistic, despite numerical convergence, but it is also likely that the approximation diverges due to sharp gradients. As a result of these difficulties, turbulence must be modeled for most industrial problems.

2.3.1 RANS Equations

One of the most common ways of approximating turbulence is to average out fluctuating quantities of the Navier-Stokes equations by separating the flow variables into a time-average and an oscillating part. This separation is known as the Reynolds decomposition. Applying this method to (2.2.7) yields what is known as the Reynolds-Averaged Navier-Stokes equations (here in component form)

$$\rho \frac{\partial \bar{u}_i}{\partial t} + \rho \bar{u}_j \frac{\partial \bar{u}_i}{\partial x_j} = \bar{f}_i + \frac{\partial}{\partial x_j}\left[-\bar{p}\delta_{ij} + \mu\left(\frac{\partial \bar{u}_i}{\partial x_j} + \frac{\partial \bar{u}_j}{\partial x_i}\right) - \rho\overline{u_i' u_j'}\right] \qquad (2.3.1)$$

where δ_{ij} is the kronecker delta function, $\bar{u}$ denotes the time average of the velocity and u' the fluctuating part. The last term within the brackets on the RHS of (2.3.1) is known as the Reynolds stress term and it is the only part of the RANS equations that includes the fluctuating part of the velocity. The RANS equations, as they are, will not constitute a closed system of equations and the Reynolds stress term has to be modeled by additional equations in order to close the system of equations. In the past, there have been many different attempts to model this stress term, resulting in a variety of different turbulence models. The first one to accomplish this was Boussinesq (1877), through the Boussinesq approximation. The idea is to model the momentum transfer caused by turbulent eddies by introducing the concept of eddy viscosity. There are several turbulence models based on this approximation, such as zero-equation models, one-equation models and two-equation models. This thesis is limited to the following standard two-equation models: the $k-\varepsilon$ and the $k-\omega$ models.

2.3.2 The $k-\varepsilon$ and $k-\omega$ models

The $k-\varepsilon$ model is one of the most commonly used turbulence models in engineering applications, most frequently for "low-speed incompressible flows in isotropic turbulence" [25]. The model includes two turbulence quantities needed to describe the turbulent aspects of the flow; the turbulence kinetic energy k and the turbulence dissipation rate ε. To account for the new turbulence quantities, two additional transport equations are added, hence the name two-equation model. This model has been documented to yield good results for free flow simulations, but is known to perform more poorly in the case of wall bounded flows and adverse pressure gradients (i.e. increasing pressure in the direction of the flow) [26].

The $k-\omega$ model is also a widely used turbulence model. In addition to the turbulent kinetic energy k, the specific turbulence dissipation rate (or vorticity) ω is used to describe the turbulent flow properties. This model performs better than the $k-\varepsilon$ model for a variety of flows [26]. The disadvantages include higher sensitivity to vorticity inlet conditions for free stream flow (flow free from the effects of walls) and lower robustness than the $k-\varepsilon$ model [26].

2.3.3 Boundary layers

Due to the no-slip condition at boundary walls, boundary layers are created adjacent to the walls where viscous effects become more dominant. Because of the creation of boundary layers, velocity gradients normal to the surface are very sharp, requiring dense meshing close to the walls in order to be resolved. To account for this fact, the method of wall functions can be applied for turbulent flow [25]. These wall functions are based on empirical laws and can be used to analytically describe the flow behavior in parts of the boundary layers, yielding boundary conditions some distance away from the wall, thus removing the need for excessive meshing.

The innermost boundary layer can be divided into three sub-layers [25]: the viscous (or laminar) layer, the buffer layer, and the log-law layer (see *Figure 2.3-1*). The log-law layer is described by what is known as the law of the wall. This law states that the tangential component of the mean velocity of turbulent flow is proportional to the natural logarithm of the distance to the wall. The velocity in the log-law layer can be written as

$$u^+ = \frac{1}{\kappa} ln y^+ + C^+ \tag{2.3.2}$$

where $u^+ = \bar{u}/u_\tau$ is the dimensionless relative velocity, tangent to the wall, $y^+ = y u_\tau / \nu$ the dimensionless relative wall distance, κ the von Karman constant, u_τ the friction (or shear) velocity and C^+ a constant whose value depends on the model approach. This approximation is valid at a distance of $y^+ > 30$ from the wall but deviates considerably when reaching values around 500. Closest to the wall is the viscous sub-layer where

$$u^+ = y^+, \tag{2.3.3}$$

which is valid for $y^+ < 5$. For $5 < y^+ < 30$ neither (2.3.2) nor (2.3.3) approximates the velocity profile satisfactorily. This intermediate region is known as the buffer layer. If there were no buffer layer, then (2.3.2) and (2.3.3) would meet at $y^+ \approx 11.6$. For values of $y < 11.6$, the viscous model works better, while the log law is superior for $y^+ > 11.6$, though none of the two models yields good results close to $y^+ = 11.6$. In addition to the velocity, the turbulence quantities are also given corresponding boundary conditions away from the wall.

The boundary conditions at the walls can vary depending on the implementation of the wall functions. One common approach is to divide the boundary layers at $y^+ = 11.6$, where the law of the wall is used above $y^+ = 11.6$ and below this limit the velocity and the turbulence quantities are based on viscous sub-layer constraints [25]. Other models incorporate all three sub-layers, where the buffer layer is modeled between $5 < y^+ < 30$. In contrast, the simplest wall function approach directly makes use of the law of the wall, without taking the other sub-layers into account.

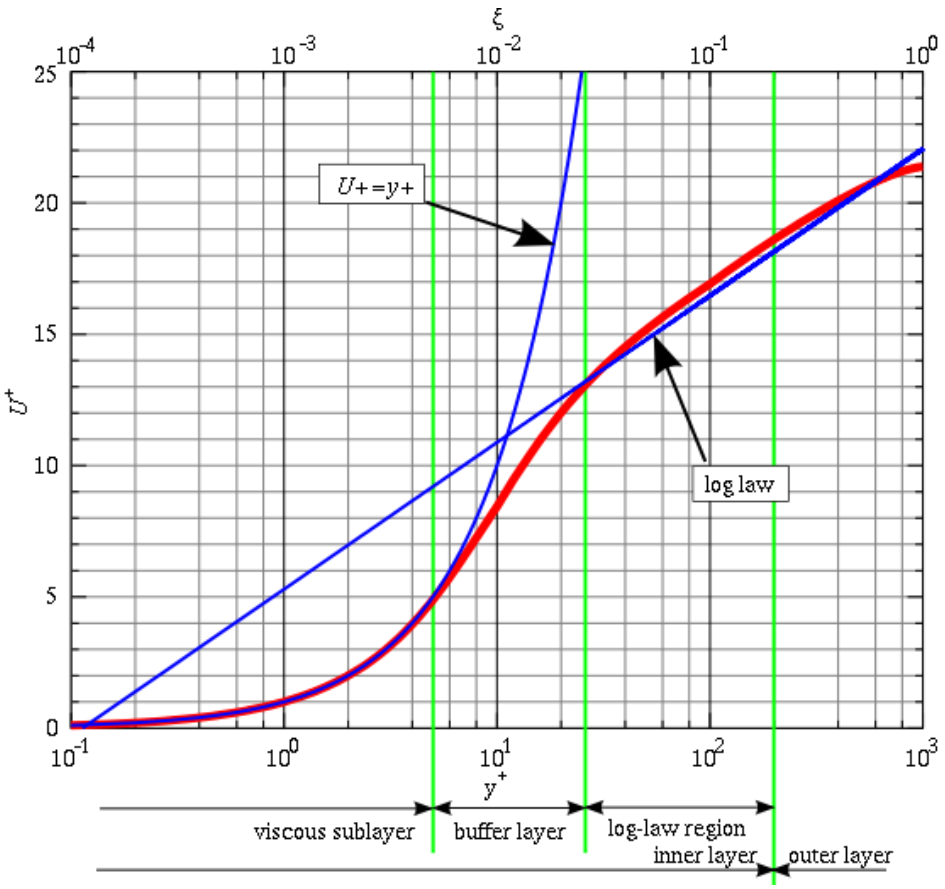

Figure 2.3-1: The boundary layers for turbulent flow. y^+ is the dimensionless relative wall distance and U^+ is the dimensionless relative velocity tangent to the wall. The figure is from an external source, by another author, and is published under the following license [27].

There are also low Reynolds number versions of the two-equation RANS models, meant to better resolve boundary layer flows (i.e. flows of lower Reynolds numbers) [28]. For these models the boundary layer is resolved all the way into the viscous sub layer ($y^+ < 5$), without relying on wall functions. This means that the quality of the boundary layer mesh is of utmost importance for low Reynolds number models.

2.3.4 Turbulence intensity and length scale

When modeling turbulence, the turbulence quantities must also be set at the inlet to the flow system to generate the correct degree of turbulence. However, it is usually very difficult to estimate the magnitude of the turbulence quantities. Instead, it is common to describe turbulence by the turbulence intensity and turbulence length scale. For fully developed turbulent pipe flow, the turbulence intensity is usually within 5-10 % and the turbulence length scale, describing the size of the eddies that are modeled, is commonly set to 7% of the hydraulic diameter of the pipe for 2D flows [29].

2.4 The Finite Element Method

The Finite Element Method (FEM) is a numerical method used to find approximate solutions to boundary value problems. It is commonly used in various fields of engineering. The main idea is to divide the domain of the problem into many smaller elements where the main PDEs can be approximated locally. The element equations are then combined into a global system of equations, over the entire domain. It is an approach based on the variational theory of calculus where an error function is minimized to yield the best approximation to the solution.

By applying variational calculus to the PDEs in question, all spatial derivatives are removed, approximating the PDEs, over each element, as ordinary differential equations in time, or just algebraic equations for steady state problems. The resulting system of equations is then solved by numerical linear algebra for steady state problems and time dependent problems are solved by numerical integration schemes. Non-linear equations, such as the Navier-Stokes equations, yield non-linear equations that have to be linearized in order to be solved. The local (element) equations are combined into a global system of equations to approximate the solution on the entire domain.

The resulting FE approximation, to the solution, is built out of linear combinations of basis functions, where each function is connected to a node point of the elemental grid/mesh (see an example in *Figure 2.4-1*). These basis functions are usually polynomials where the order can be increased to improve accuracy, but this also increases the computational complexity of the problem. When solving the Navier-Stokes equations, it is important that the basis functions describing the velocity are, at least, one order higher than those describing the pressure [30].

There are many advantages with the FEM since complex geometries can be described with non-uniform meshes (unlike finite difference methods where the mesh elements are of uniform size). The downside is that it is mathematically complex compared to other methods such as the Finite Volume Method (FVM), another common (numerical) method often used for fluid flow problems.

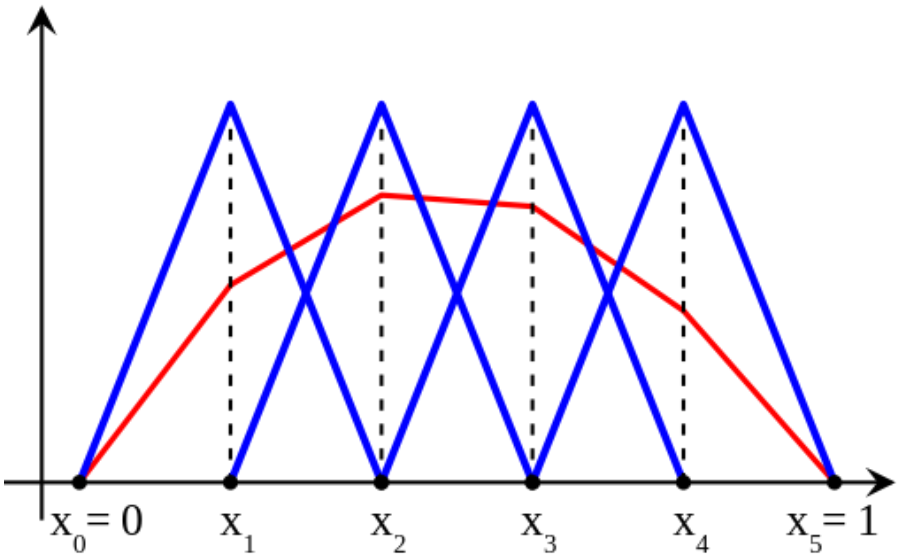

Figure 2.4-1: An example showing a 1D FE-approximation (red) created using a linear combination of piecewise linear basis functions (blue). The six points located at $x_0, x_1 \dots x_5$ represent the node points of the computational mesh, with mesh elements in between. The figure is from an external source, by another author, and is published under the following license [31].

3 Method

This section covers the approach of the experimental measurements and CFD simulations. The first part includes the setup and measurement approach for the experimental measurements, as well as providing a description of the three stenosis models. The latter part involves the CFD simulations in COMSOL, where the settings are explained in steps and the methods are motivated. The chapter ends with a short explanation of what tests were made to compare the CFD simulations with the experimental results.

3.1 Experimental measurements

The aim of the experiments was to characterize the pressure behavior in three different plastic tube stenosis models being subject to a pulsatile flow of water. The experimental setup and method correspond to the ones utilized in the article Natural angioplasty: A mechanical effect of exercise [4].

3.1.1 Experimental setup

The experimental setup (*Figure 3.1-1*) was identical for all measurements and all stenosis models. To create a constant fluid flow through the system, a peristaltic pump (Ismatec BVK, Zurich, Switzerland) was connected to the stenosis model in question by a system of elastic tubes. These tubes were extended to a length of 17 meters in order to dampen possible disturbances in the flow. The pump was also connected to a container of water that fed fluid to the system, and the flow rate was regulated by 6 taps connected to the peristaltic pump. Pulsations were added by connecting a syringe pump to the flow system, upstream of the stenosis, pumping at a frequency of 1 Hz (to simulate the heart beat). The pulsations were added at an angle of 90 degrees to the constant flow stream. For this reason, the syringe pump was connected some distance away from the stenosis in order for the flow to become fully developed before reaching the model inlet. The syringe pump was programmed using the software *LabVIEW* (National Instruments Corporation, Austin, Texas, U.S.) to create a volume curve that was triangular in shape with a volume difference of approximately 0.4 ml peak-to-peak. To remove the effects of the hydrostatic component of the pressure, the system was placed horizontally. No flow was used as zero reference pressure, and the end of the flow line was open to air (open outflow).

To measure the pressure, a RadiAnalyzer^{TM} Xpress measuring system (Radi Medical, Uppsala, Sweden), displaying the maximum (systolic), minimum (diastolic) and mean pressure, was connected to the system utilizing a Pressure Wire Certus catheter system 12006 (St Jude Medical Systems, Uppsala, Sweden) that included a catheter tip pressure sensor and a fluid catheter sensor. Both the reference pressure (at the model inlet) and the pressure at discrete points inside the stenosis could then be measured simultaneously. The catheter tip sensor was inserted through the elastic tube upstream of the stenosis models and was fed through the stenosis, little by little, during the measurements. Due to the construction of the catheter tip pressure sensor, where the point of measurement was positioned 3.05 cm from the endpoint of the sensor, the catheter tip was occupying the stenosed region at all times. In addition, the rigid stenosis model was extended at the model end by an additional elastic tube (10.5 cm in length) in order for the catheter tip sensor to be fully submerged during the measurements. The resolution for the pressures displayed by the RadiAnalyzer was 1 mmHg.

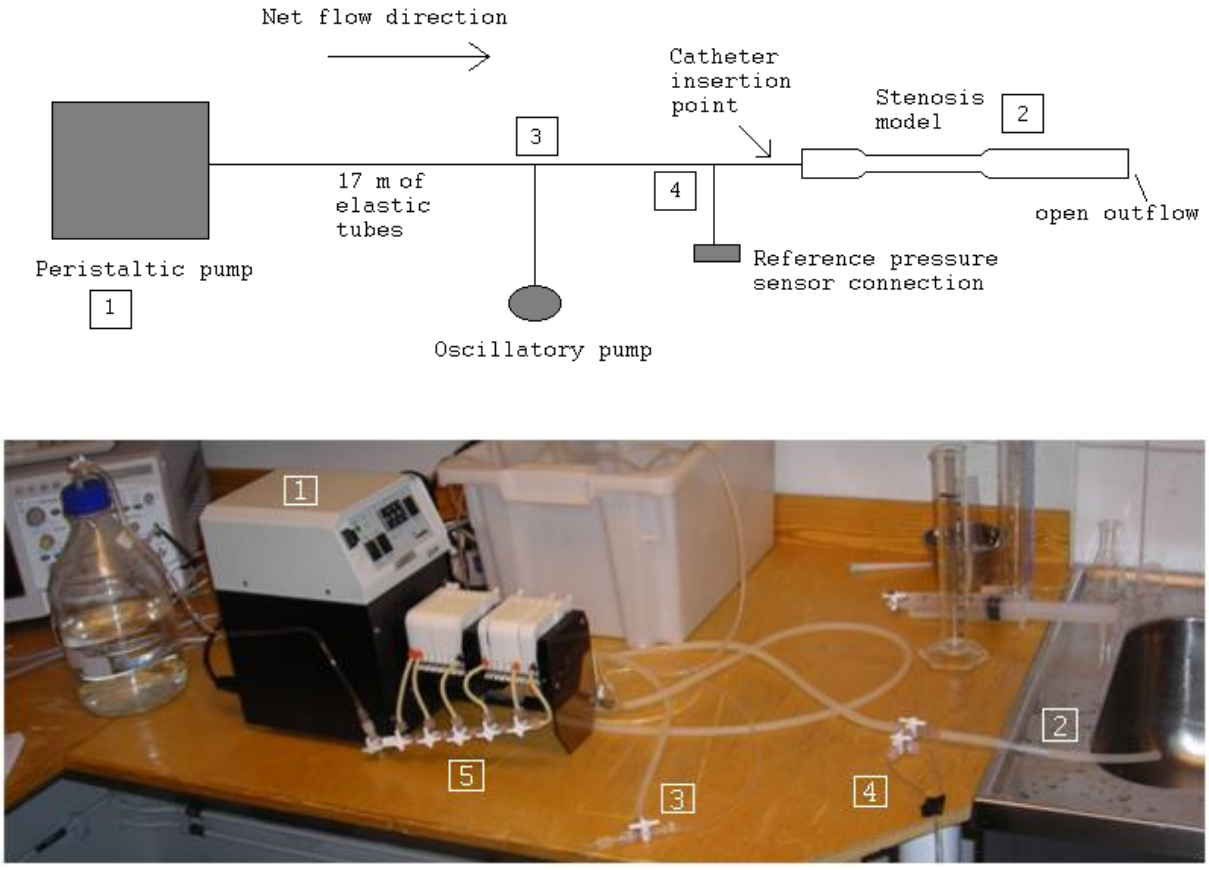

Figure 3.1-1: The experimental setup (bottom) and the corresponding schematic sketch (top). The peristaltic pump (1) is connected to the stenosis model (2) by 17 m of elastic tubes. Additional connections are those of the oscillatory (syringe) pump (3) and the reference pressure sensor (4). The taps regulating the flow can be seen in the photo (5).

3.1.2 The stenosis models

Three axisymmetrical stenosis models of slightly different geometries were used during this project. Each model consisted of a Plexiglas tube with an inner diameter of 3 mm and a stenosed region (or a constriction) of different length, diameter and inlet/outlet shapes (*Table 3.1-1*). Two of the models were artery stenosis models and the third was a simplified model of the cerebral aqueduct (*Figure 3.1-2*). All models had a length of 57 mm, without the elastic extension of 10.5 cm. It is important to note that in the previous study [4] an extra resistance was added downstream of the stenosis models (to increase the pressure at the model inlet), something that was not included in this thesis.

Table 3.1-1: The geometric parameters of the three stenosis models.

Model	Stenosis length (mm)	Stenosis inner diameter (mm)	Inlet/outlet angles α (degrees)
Artery stenosis 1	7.0	1.0	120/120
Artery stenosis 2	8.0	1.5	120/120
Aqueduct	7.0	1.0	60/180 or 180/60

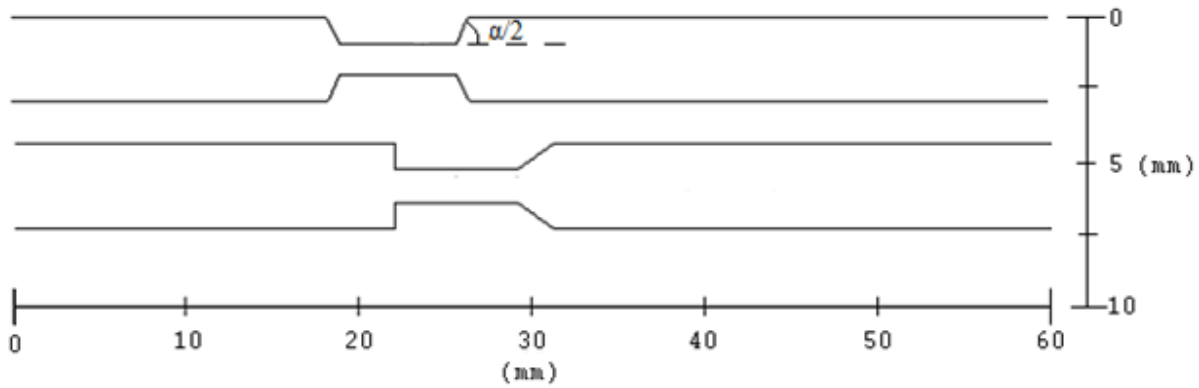

Figure 3.1-2: Cross-sections of the stenosis models. The artery models (top) and the aqueduct model (bottom). Half the inlet/outlet angle (α) is shown in the upper model.

3.1.3 Measurement method

Both constant and pulsatile flow measurements were performed. For the pulsatile flow measurements, pulsations were added to the constant flow, resulting in a net flow in the direction of the constant flow. The pulsatile part of the flow was kept at constant pulsation rate and volume (the same settings for all measurements) and only the constant flow rate was varied. For the artery stenosis models, the pressure was measured in six points (*Figure 3.1-3*) with the catheter tip pressure sensor, while ten points were used for the aqueduct model (*Figure 3.1-3*). For each measurement, the systolic, diastolic and mean pressures were documented, both in the reference point (at the model inlet) and in the measurement point inside the stenosis model in question. All pressure measurements under pulsatile flow were performed six times per measurement point, resulting in six measurement series, and once per measurement point for the constant flow measurements. The mean flow rate was measured by collecting the volume of water passing the stenosis model in intervals of 20 and/or 30 seconds. For the pulsatile flow measurements, the flow rate was measured two or three times per measurement series, and six times per flow rate for the constant flow rate measurements. During the measurements, the water was kept at a temperature between 23 and 24 degrees centigrade (measured with a Delta OHM thermometer HD 9214, 0.1°C resolution).

While the constant flow measurements were done for several different flow rates for each stenosis model, the pulsatile measurements were only done for the following (mean) flows and models:

- 129 ml/min for the 1.0 mm artery stenosis model
- 130 ml/min and 173 ml/min for the aqueduct model when using the smooth narrowing as inlet
- 131 ml/min and 172 ml/min for the aqueduct model when using the abrupt narrowing as inlet

The pulsatile flow measurements with the artery stenosis model were performed to recreate the results of the previous study [4]. Measurements with the aqueduct model were performed for both directions to investigate possible differences due to differing stenosis inlet/outlet shapes.

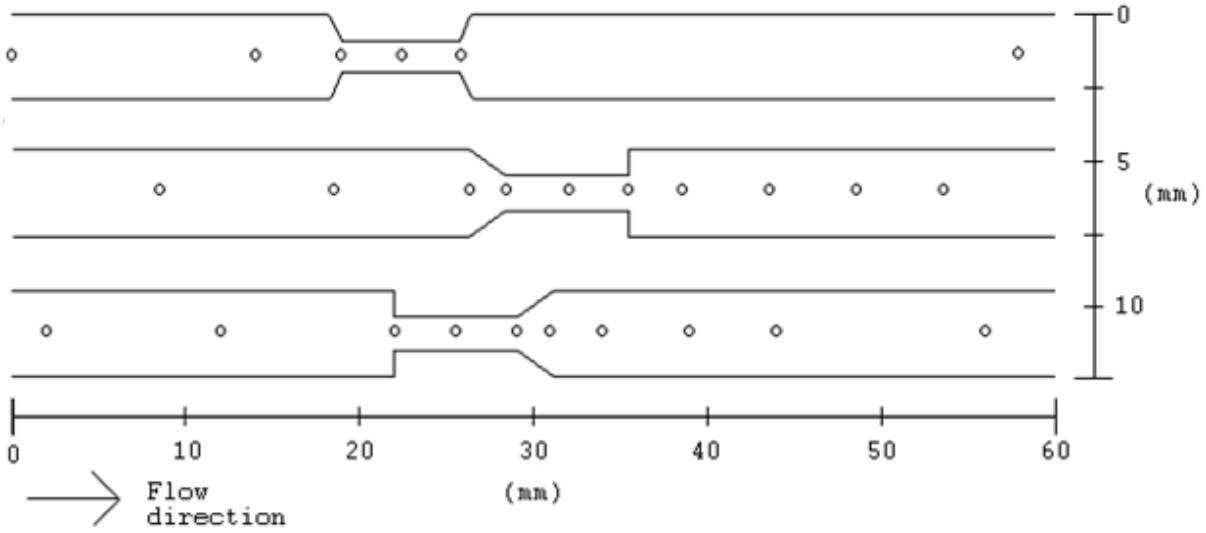

Figure 3.1-3: Pressure measurement points for the artery models (top), the aqueduct model with the smooth narrowing proximal to the flow (middle), and distal to the flow (bottom).

3.1.4 Additional measurements: Removing the catheter sensor

Pressure measurements were also performed with an infusion system, *Likvor CELDA® System* (Likvor AB, Umeå, Sweden), replacing the catheter pressure system, in order to remove the effects of the inserted catheter tip on the flow. Due to time constraints, only measurements with the 1.0 mm artery model were performed using the *CELDA* system. For these additional measurements, only the total pressure drop over the stenosis model was measured (from the model entrance to the end of the elastic extension), for pulsatile flow, and the mean flow rate was measured three times per flow rate.

3.2 CFD in COMSOL

The experimental measurements were compared to CFD simulations run with the software *COMSOL Multiphysics*® (Version 4.3b) and its CFD module. *COMSOL* is based on the FEM (see *Section 2.4*), which is well suited for fluid flow problems. In *COMSOL* it is possible to create 1D, 2D, 2D-axisymmetric and 3D models, where the geometry, physics (equations and boundary conditions) and the mesh can be defined, all without the need for any additional software. *COMSOL* also includes various study options (such as solver methods) and post processing alternatives.

3.2.1 2D versus 3D

Since turbulence is a 3-dimensional phenomenon it is desirable to utilize 3D when solving problems of fluid flow. However, due to the increase in computational cost between 2D and 3D, in both memory and processing time, it was decided to start with 2D simulations since it should still capture the main features of the flow, but to a lower computational cost. Since the geometries of the model stenoses were axisymmetric, a 2D-axisymmetric geometry could be used, which is close to a 3D representation.

3.2.2 Geometry: Including the pressure catheter sensor

The geometry of each CFD model consisted of the stenosis model, plus the additional extension of 10.5 cm, and the catheter sensor. Since the pressure was expected to change very little in regions away from the stenosis, the elastic extension was modeled as rigid in the CFD simulations to simplify the numerical calculations. The catheter was approximated as a rigid stationary cylinder placed inside the stenosis model, along the axis of symmetry, creating the geometry of an annulus as opposed to a cylindrical geometry. During the experiments, the catheter was observed to fluctuate as well as shifting shape when bent against the walls of the model, which introduced effects not accounted for in the simulations. However, since the catheter was mostly positioned in its central position, and the flow area was the same, this simplification was deemed reasonable.

3.2.3 Laminar and turbulent physics

For all simulations of this thesis, the water density was set to $1000\ kg/m^3$ and the viscosity to $0.00095\ Pa \cdot s$ (the same values as used in the theoretical model of [4]). The Reynolds number was approximated to be below 2000 in the pipe and larger than 2000 in the stenosis region for nearly all of the experimental measurements (see *Appendix C*). For cylindrical pipe flow, this includes the transitional regime where flow behavior is difficult to analyze. Because of this fact, both laminar physics simulations and simulations including the modeling of turbulence were tested. *COMSOL*'s CFD module gives the option to model laminar as well as turbulent flow with already implemented physics models. For the turbulence model, the choice fell on the RANS $k-\omega$ model due to it being one of the most prominently used turbulence models within the field of CFD today. The $k-\omega$ model implemented in *COMSOL*, at the time, was the revised Wilcox model with wall functions [26]. For the laminar model, the incompressible Navier-Stokes equations (2.2.7) and the corresponding continuity equation (2.2.6) were used to solve for the velocity vector and the pressure (in cylindrical coordinates). For the turbulence model, the RANS equations (2.3.1) were solved with two equations added for the turbulence quantities, k and ω, to close the system of equations.

In addition, a low-Reynolds number model was also tested to better describe the gradients close to the walls, instead of relying on wall functions. Since the low Reynolds $k-\omega$ model was not implemented in *COMSOL* at the time, the low Reynolds number $k-\varepsilon$ model was applied, but with no success for annulus flow (no convergence in the solutions). For cylindrical flow (no catheter), the low-Re model was applied successfully and was included in the analysis of the additional measurements (the *Likvor CELDA® System* measurements). For this model, two equations, one for k and one for ε, were added to the RANS equations.

Regarding discretization, *COMSOL* makes use of several stabilization techniques in order to discretize flow problems using first order (P1) basis functions for both the velocity and the pressure, instead of using higher order basis functions for the velocity. The default settings include two consistent stabilization techniques: streamline and crosswind stabilization [32]. The number of degrees of freedom is severely reduced by using P1-P1 elements, but it may result in poor resolution of steep gradients. For most simulations, this setting was used to improve simulation speed, although the P2-P1 discretization was tested but did not yield any noticeable change in the results.

3.2.4 Boundary conditions

A velocity condition was set at the model inlet for all simulations. The mean velocity was computed from (2.1.2), since only the flow rate was known (measured). For laminar inflow, (2.1.11) and (2.1.12) could be used for the cylindrical and annulus flow, respectively, to get the corresponding velocity profiles for constant flow. For the turbulence simulations, the turbulence quantities were defined by the turbulence intensity and turbulence length scale. The intensity was set to 5 % and the length scale to 0.07 hydraulic diameters, which is recommended for fully developed turbulent pipe flow [29].

To introduce pulsations to the flow, an oscillating flow rate was applied at the inlet in the form of a sinusoidal wave, representing the motion of the syringe pump supplying a volume of 0.4 ml at a frequency of 1 Hz (see *Section 3.2.5*). This means that a volume of 0.4 ml was added and withdrawn every second. The pulses were added as uniform velocity, and the geometry was prolonged upstream of the stenosis region to let the flow develop properly before reaching the stenosis inlet.

The boundary conditions for the rigid walls were set to no-slip in the laminar simulations. For the turbulence $k-\omega$ model, boundary flow was handled by using wall functions [33]. In *COMSOL*, the distance from the wall to the computational domain (or wall lift-off) is automatically calculated so that the dimensionless wall distance (or wall lift-off in viscous units) is 11.06. The buffer layer is ignored and the entire viscous sub-layer is represented analytically. Since the viscous and buffer layers are very thin, for fully turbulent flow, it is important that the wall distance is very small compared to the dimensions of the geometry. It is also important that the dimensionless distance is 11.06 everywhere on the walls, or close to it, in order for this wall function approach to be valid. This was investigated for all simulations where the turbulence $k-\omega$ model was used (see *Appendix D*). For the low Reynolds number turbulence model, a no-slip condition was set at the walls.

At the outlet, a simple Dirichlet condition was set for the pressure, since it was open to atmospheric pressure (open outflow). Due to the fact that only the change in pressure over the stenosis was of interest, and not the absolute pressure, the value of the pressure was set to zero at the outlet (instead of atmospheric pressure).

3.2.5 Adding Pulsations

To add pulsations, the oscillatory flow had to be described by a varying flow rate, which was then converted to velocity through (2.1.2). Since the volume inserted/removed every half second was known to be 0.4 ml, the pulsations could be estimated by integrating the sought after flow rate over half a second and setting it equal to the inserted volume. Mathematically this can be described as

$$V_{inserted} = \int_0^{T/2} Q(f,t)dt \tag{3.2.1}$$

where Q is the oscillating flow rate, f the frequency of the oscillations, T is the oscillation period and $V_{inserted}$ is the volume inserted. The programmed motion of the syringe pump was described by a triangular function of frequency 1 Hz, but under the experiment the profile was observed to be more sinusoidal. For this reason the periodic flow rate was approximated as a sine function yielding

$$V_{inserted} = \int_0^{T/2} A_{osc} \cdot sin(2\pi f t)dt \tag{3.2.2}$$

where A_{osc} is the amplitude of the flow rate oscillations. Then, using the fact that $T = 1/f$, the amplitude becomes

$$A_{osc} = \frac{V_{inserted}}{\left[-\frac{\cos(2\pi f t)}{2\pi f}\right]_0^{1/2f}} = V_{inserted}\pi f. \tag{3.2.3}$$

Adding this to the constant flow yields the final expression for the inflow

$$Inflow = Q_{mean} + V_{inserted}\pi f \sin(2\pi f t). \tag{3.2.4}$$

3.2.6 Meshing

A free triangular mesh was used within the flow stream away from the walls while boundary layers were added close to the walls. Since the velocity changes very rapidly in the direction normal to the wall, close to the boundary, and very little in the tangential direction of the wall, the boundary layers were made to consist of quadrilateral elements tightly packed in the direction normal to the wall and more sparsely in the tangential direction (see *Figure 3.2-1*). Mesh refinements were added for all sharp edges and the line of flow separation.

A mesh analysis was made where the number of finite elements was increased with the aim to find a fine enough mesh where no change in the quantities of interest occurred for any additional increase in the number of elements, or until the variations were negligible. The quantities of interest were the pressure drop over the stenosis and the recirculation length of the separation zone. The mesh study was done for all three stenosis models (see *Appendix B*). For the laminar model, the recirculation length required a large number of mesh elements in order to remain constant. In addition, when the number of elements was increased, the resulting recirculation length moved even further from the expected results. Because of this, the pressure drop was the main deciding factor when creating the mesh (for the laminar model simulations).

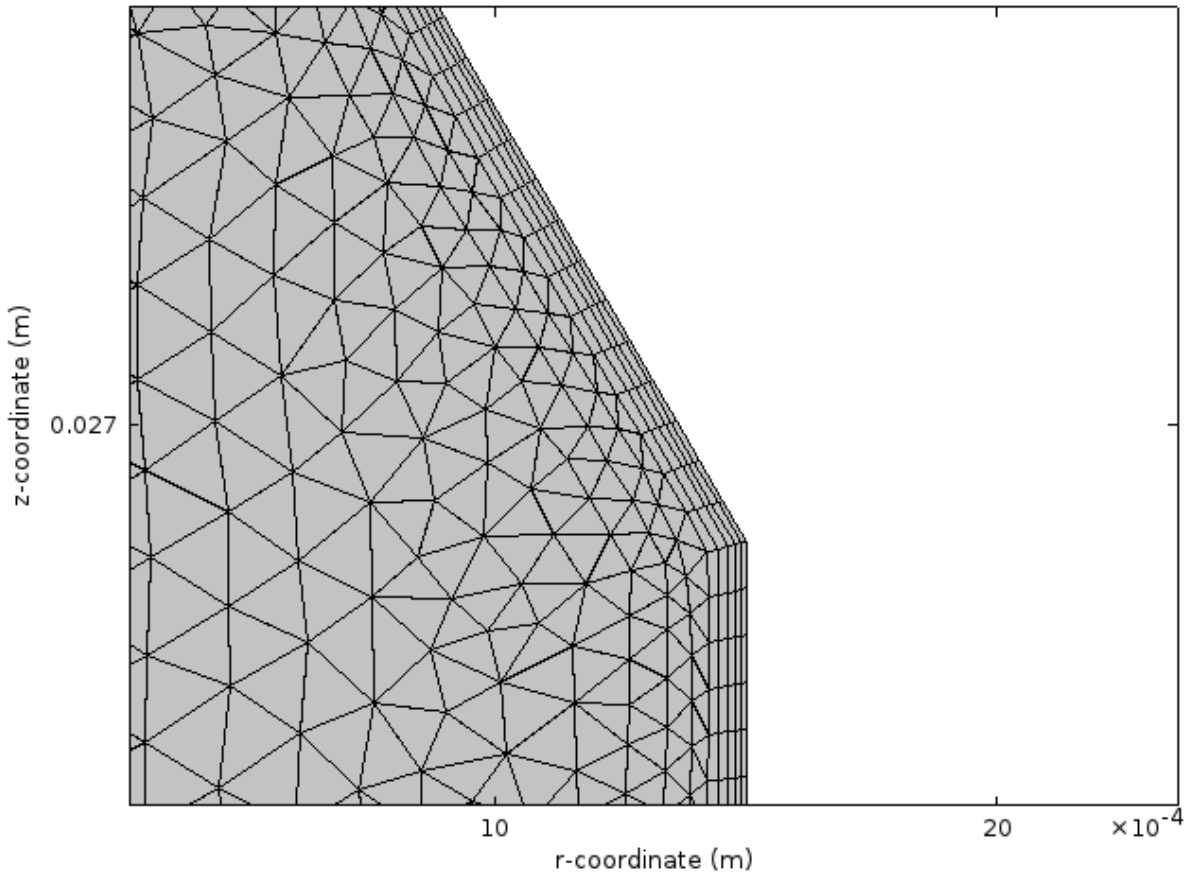

Figure 3.2-1: The computational mesh with triangular elements on the inner domain and wall boundary layers consisting of quadrilateral elements tightly packed in the direction normal to the wall.

3.2.7 Stationary and transient solvers

For the stationary solver, *COMSOL* uses Newton's method (Newton-Raphson) to solve the non-linear Navier-Stokes equations [34]. The non-linear solver iterates to find the solution, and for each iteration the non-linear system of equations is linearized and solved using a linear solver [34]. These linear solvers are either direct or iterative [35]. For most simulations of this thesis, a direct linear solver was used due to them being more robust than iterative solvers. This was also the default choice made by *COMSOL* for most simulations. The direct solver makes use of Gaussian elimination, or LU factorization, to solve the linearized matrix system. For the simulations with the $k-\omega$ turbulence model, the turbulence quantities were solved separately from the velocity and pressure by using a segregated solver, and the default solvers chosen by *COMSOL* were always used. The low Reynolds $k-\varepsilon$ model simulations were solved using a segregated solver as well.

Two time-dependent solvers are available in *COMSOL:* the BDF and Generalized Alpha solvers [36]. The time-dependent simulations, of this thesis, were handled by the BDF time solver, a solver based on backward differentiation formulas. This method is more stable than the Generalized Alpha, something that was often needed for the problem of interest, though damping of fast oscillations might be introduced, which is an unfortunate property of the backward differentiation methods. The Generalized Alpha solver was used for comparison, when possible, but this did not impact the results, regarding the quantities of interest.

3.2.8 Studies and post processing

The main CFD studies involved simulations of the experimental measurements described in *Section 3.1*, and also those of the previous study [4]. The CFD results were analyzed with focus on:

- Pressure behavior along the stenosis models.
- Pulsatile flow effects.
- The total pressure drop dependence on the shape of the stenosis.

Since the pressure was mostly uniform in the radial direction, the pressure along the pipe was investigated along a central line through the stenosis model, and not averaged in separate cross-sections. For total pressure drop measurements, the spatial (cross-sectional) average pressure at the model inlet was calculated. Since the pressure was set to zero at the outlet, the inlet pressure corresponded to the total pressure drop. The pulsatile effects on the pressure were investigated by looking at the total pressure drop at different points in time, mainly comparing the systolic and diastolic pressure drops. To investigate the effects of different stenosis shapes the pressure drop was compared for the different stenosis models. In addition, a separate angle study was performed where the stenosis inlet and outlet angles were varied while the effects on the total pressure drop were studied. The inlet and outlet angles were varied separately and the angle held constant was set to 20 degrees. The pressure drop dependence on the stenosis diameter was investigated by simply varying the diameter.

In addition to the main studies, several shorter studies were made to further evaluate the validity of the CFD simulations (see *Appendix D*). These studies were meant to investigate:

- The velocity profiles right before the stenosis inlet.
- The pressure drop corresponding to (2.1.6) and (2.1.7) for cylindrical and annulus pipe flow, respectively.
- The effects of the manual catheter adjustments made during measurements.
- Wall lift-off and wall lift-off in viscous units for the turbulence model simulations that utilized wall functions.

4 Results

The following section contains all collected results related to the specific aims of the project. The pressure behavior inside the models is presented for the catheter measurements, as well as the total pressure drop as a function of flow rate. The pressure drop dependence on the geometry of the stenosis (inlet, outlet and diameter) and pulsatile flow effects are investigated. The chapter ends with a presentation of the no-catheter measurement results in order to determine the effects introduced by the inclusion of the catheter pressure sensor.

4.1 Pressure behavior

4.1.1 Pressure along the stenosis models

The time-averaged pressure behavior along the 1.0 mm model for pulsatile flow (mean flow rate of 129 ml/min) is presented in *Figure 4.1-1* and *Figure 4.1-2*. The results for the laboratory experiments showed a major pressure decrease over the stenosis region and pressure recovery downstream of the stenosis outlet. The pressure decrease was the largest at the stenosis inlet, partly due to the static to kinetic pressure conversion, but the pressure also decreased considerably inside the stenosis. The laminar CFD results agreed with the experimental results up to the stenosis outlet, but downstream of this point the observed pressure recovery was slower than in the experiments. However, when looking at the total pressure drop (the irreversible pressure loss over the entire model plus the added extension), the results showed that the laminar simulation predicted the expected pressure recovery (approximately) but further downstream than in the experiments. The turbulence model simulation, on the other hand, severely underestimated the total pressure drop, but showed a much faster pressure recovery at the outlet, more in line with the experiments. The length of the separation zones (at the stenosis outlet) for the 1.0 mm artery model can be seen in *Figure 4.1-3* and *Figure 4.1-4* for the laminar simulations and the turbulence $k-\omega$ simulations, respectively. For the turbulence model, the recirculation length was slightly longer than one centimeter, while the laminar model simulation yielded a recirculation length that extended up to more than ten centimeters. Flow separation was also observed at the stenosis inlet (in the CFD-simulations) where a slight pressure recovery can be seen (*Figure 4.1-2*). The CFD simulations corresponding to the previous study, [4], were very similar to the ones presented here, thus only the total pressure drop results are presented for those simulations (see *Table 4.1-1*).

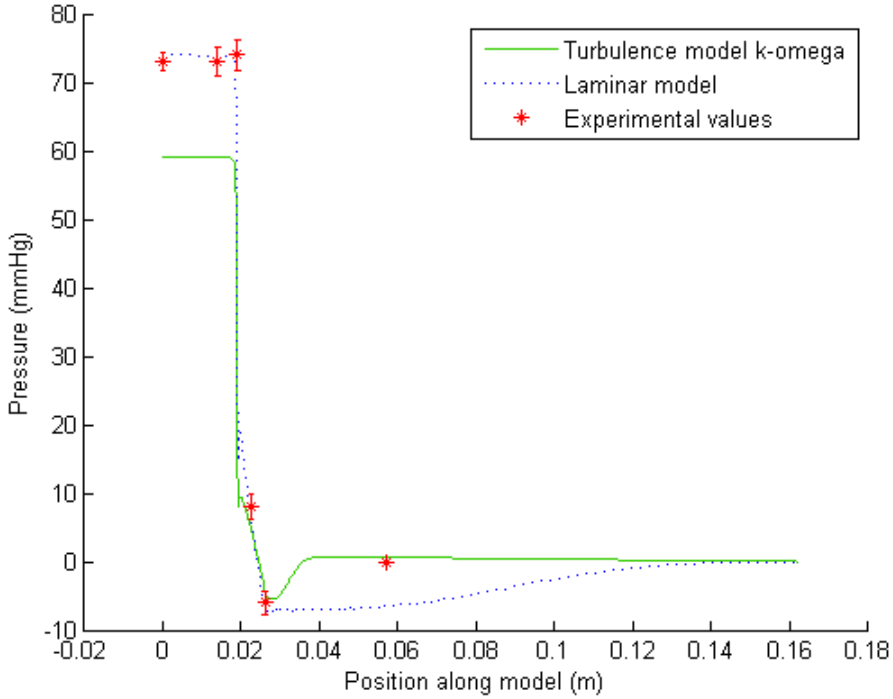

Figure 4.1-1: Time-averaged pressure along the 1.0 mm artery stenosis model for pulsatile flow (mean flow rate of 129 ml/min). The CFD simulations are compared to the experimental values. The error bars show the standard deviations for the mean pressure measurements.

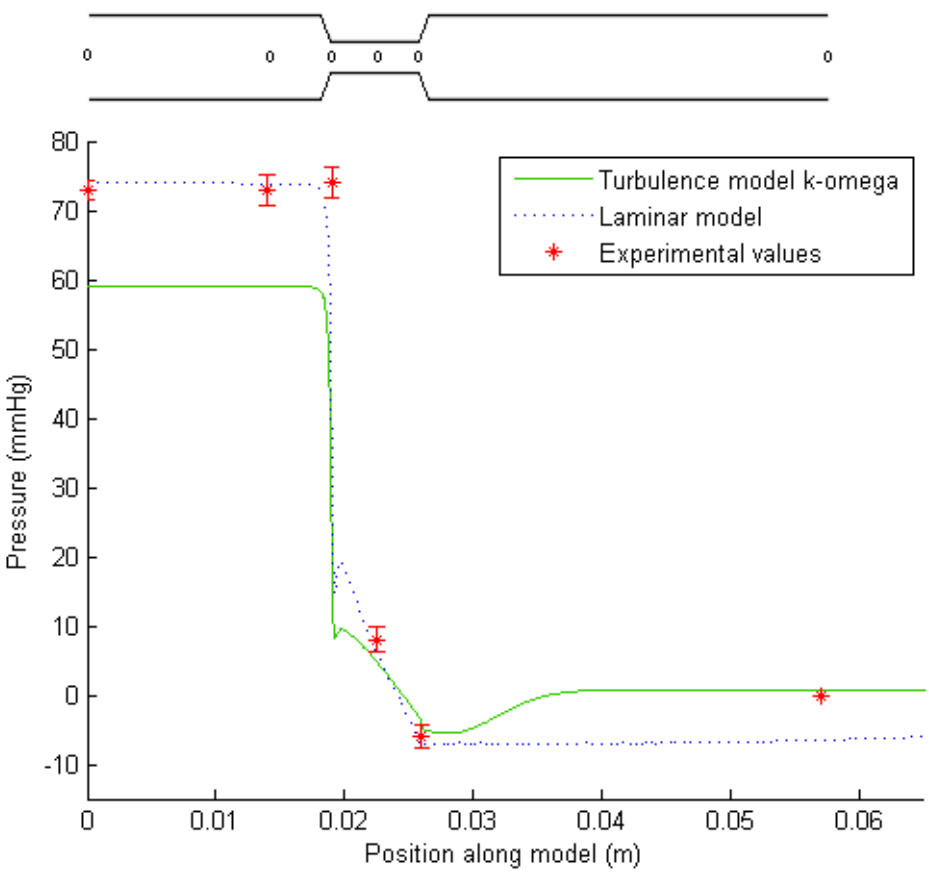

Figure 4.1-2: Closer look at the pressure along the 1.0 mm artery stenosis model for pulsatile flow (mean flow rate of 129 ml/min). The CFD simulations are compared to the experimental values. The error bars show the standard deviations for the mean pressure measurements.

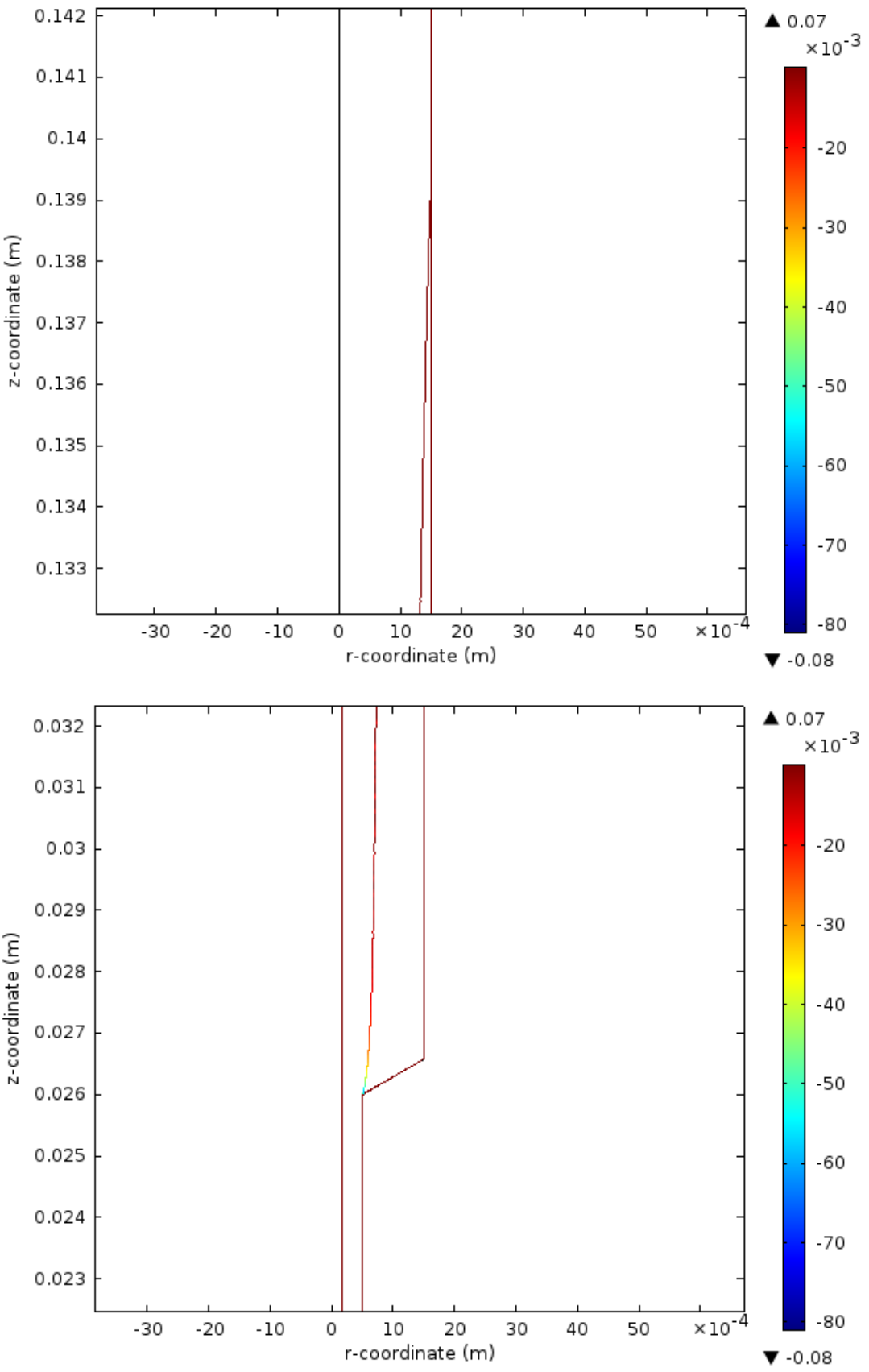

Figure 4.1-3: Contour plot, where the z-velocity component is zero, showing the boundaries of the separation zone for the laminar flow simulation (1.0 mm artery model). The color scale represents the radial velocity. The lower plot shows the point of flow separation and the upper plot shows the point of reattachment. The mean flow was 129 ml/min.

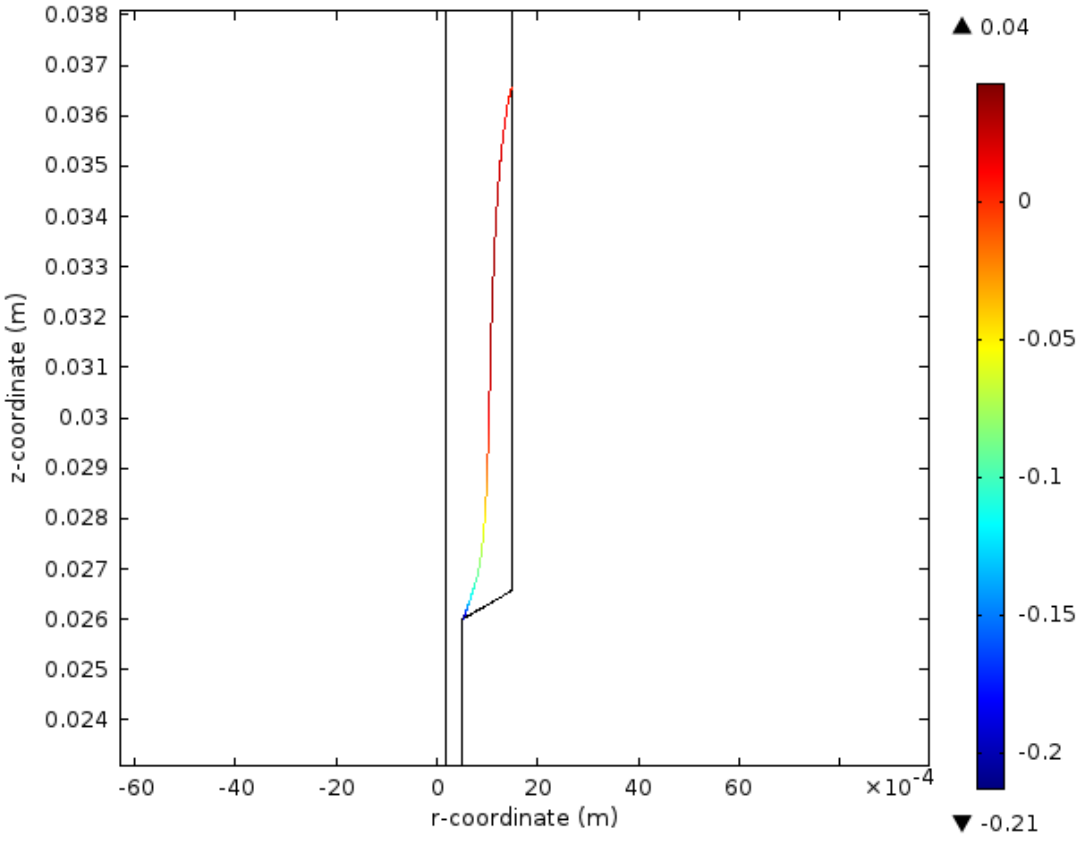

Figure 4.1-4: Contour plot, where the z-velocity component is zero, showing the boundaries of the separation zone for the turbulence model $k-\omega$ simulation (1.0 mm artery model). The color scale represents the radial velocity. The mean flow was 129 ml/min.

The corresponding results for the aqueduct model can be seen in *Figure 4.1-5* and *Figure 4.1-6*. The experimental results showed a smaller total pressure drop compared to that of the 1.0 mm artery model, for approximately the same flow rate. The experimental results also showed that the pressure recovery occurred within 1-2 centimeters downstream of the stenosis outlet, for both flow directions. The laminar simulations overestimated the total pressure drop while (still) underestimating the adverse pressure gradient. However, the laminar simulation results were still relatively close to the experimental results inside the stenosis region. The turbulence model simulations were in much closer agreement with the experiments regarding both the pressure drop and the adverse pressure gradient, though the length of the separation zone was slightly underestimated for the smooth inlet simulation (early pressure recovery). In addition, the turbulence model simulation with the abrupt stenosis inlet predicted a larger pressure decrease at the stenosis inlet than expected, resulting in lower pressure inside the stenosis region, and quick pressure recovery right at the stenosis outlet, something that was not seen in the experiments. The results for the higher flow rate (≈170 ml/min) yielded similar results, thus only the total pressure drop data is presented for those measurements (see *Table 4.1-1*).

When comparing the experimental results for the two flow directions (*Table 4.1-1*), no major difference could be seen in the total pressure drop between the two, only a slight difference of 2 mmHg for the increased flow rate (≈170 ml/min). The laminar simulations yielded a slightly larger pressure drop for the abrupt stenosis inlet, for both flow rates investigated, while the turbulence model showed minimal differences. The experimental data, from the pulsatile flow measurements, can be found in *Appendix E*.

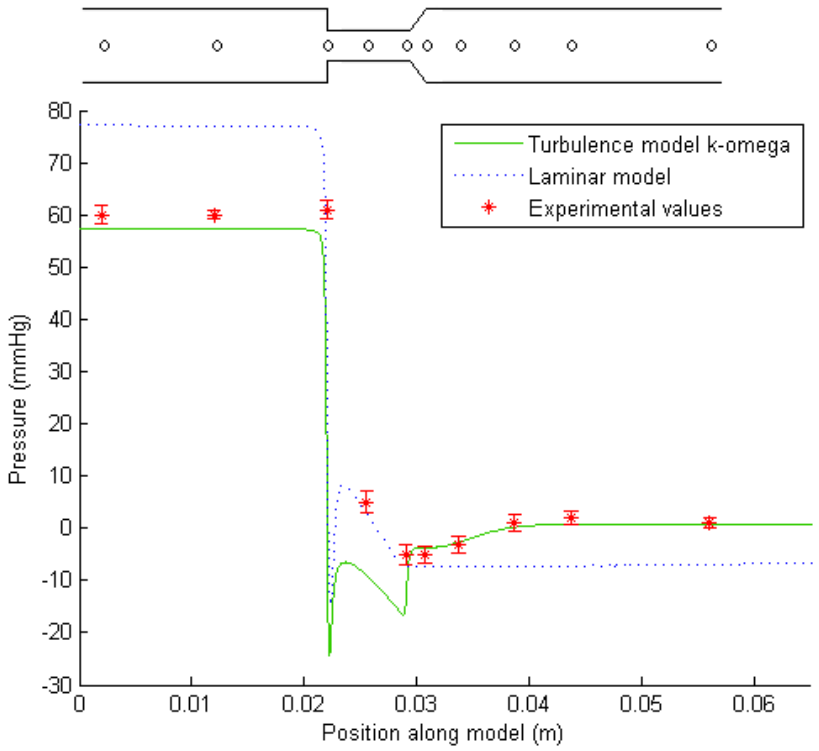

Figure 4.1-5: Time-averaged pressure along the simplified aqueduct model (abrupt narrowing proximal to the flow) for pulsatile flow (mean flow rate of 131 ml/min). The CFD simulations are compared to the experimental values. The error bars show the standard deviations for the mean pressure measurements.

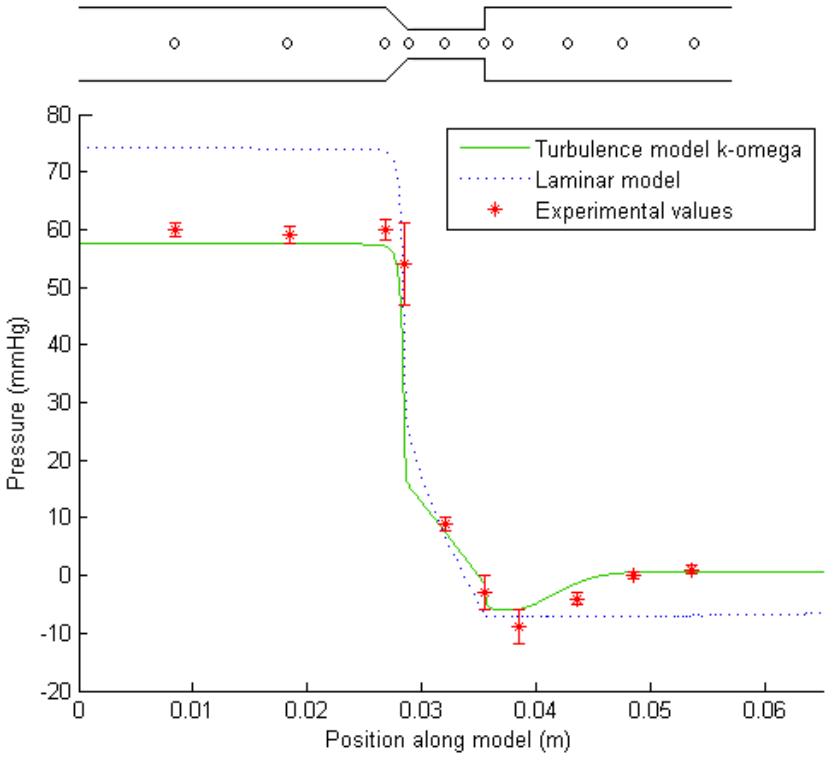

Figure 4.1-6: Time-averaged pressure along the simplified aqueduct model (smooth narrowing proximal to the flow) for pulsatile flow (mean flow 130 ml/min). The CFD simulations are compared to the experimental values. The error bars show the standard deviations for the mean pressure measurements.

Table 4.1-1: The total pressure drop under pulsatile flow for the different stenosis models and mean flow rates. The numbers in parenthesis represent data from the previous study [4].

Stenosis model	Mean flow rate (ml/min)	Average total pressure drop, experiments (mmHg)	Average total pressure drop, laminar model (mmHg)	Average total pressure drop, turbulence model (mmHg)
Artery model 1.0 mm	129	73.0	74.0	58.4
Artery model 1.0 mm	(126)	(70.5)	71.0	55.8
Artery model 1.0 mm	(173)	(123.5)	122.5	105.1
Aqueduct model, smooth inlet	130	60	74.3	57.6
Aqueduct model, abrupt inlet	131	60	77.2	57.3
Aqueduct model, smooth inlet	173	92	122.5	99.8
Aqueduct model, abrupt inlet	172	94	126.7	98.5

4.1.2 Total pressure drop as a function of volumetric flow rate

To investigate the total pressure drop, from the model inlet to the end of the extension, and its dependence on the flow rate, the results from several constant flow measurements were compared. The results for the 1.0 mm artery stenosis model can be seen in *Figure 4.1-7*. The results showed good agreement between the laminar simulations and the experimental values for intermediate flows, while the difference was larger for the lowest and highest flow rates. The turbulence model predicted a lower pressure drop than expected for the 1.0 mm artery model, with the lowest flow rate of 58 ml/min being the only exception. The same investigation was made for the 1.5 mm artery stenosis model which showed a similar behavior (*Figure 4.1-8*). The point corresponding to the lowest flow rate indicated a negative pressure drop in the experiments, which is unrealistic. This measurement error was likely caused by a drift in the pressure sensor signal. When comparing the results for the two artery models, it is clear that the increase in stenosis diameter, from 1.0 mm to 1.5 mm, yielded a considerable decrease in the pressure drops. For the aqueduct model, the turbulence model simulations yielded results that were closer to the experimental results than the laminar simulations (*Figure 4.1-9* and *Figure 4.1-10*). The laminar simulations overestimated the pressure drop for all flow rates investigated, and the turbulence model simulations agreed well with experiments for low and intermediate flow rates. The difference between experiments and simulations increased for increasing flow rates, for both CFD approaches. The results also showed that the pressure drop was slightly non-linear in its dependence on the flow rate for all stenosis models (see *Appendix F*). The pressure drop data, for the constant flow measurements, can be seen in *Appendix E*.

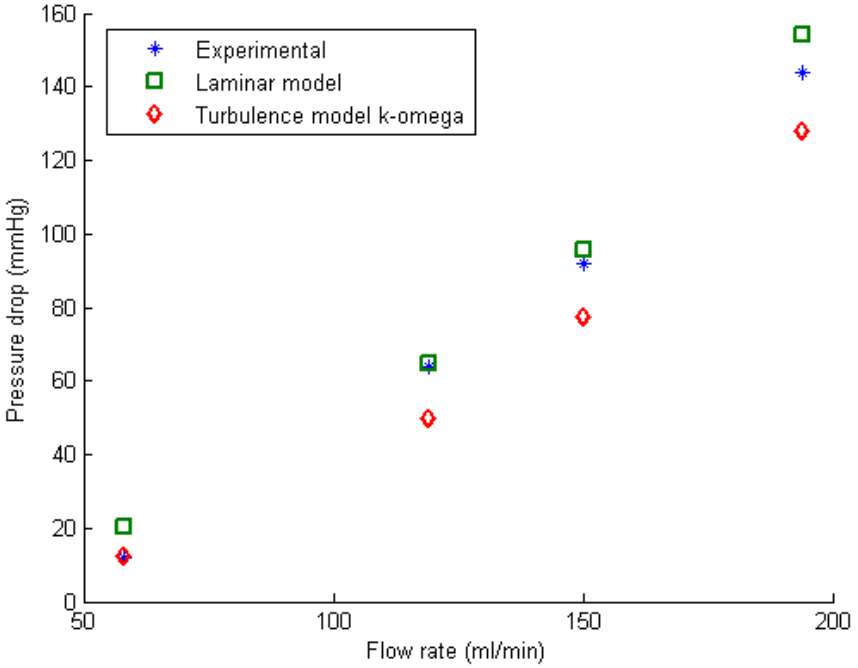

Figure 4.1-7: The total pressure drop as a function of flow rate for the 1.0 mm artery stenosis model. CFD simulations are compared to the experimental results.

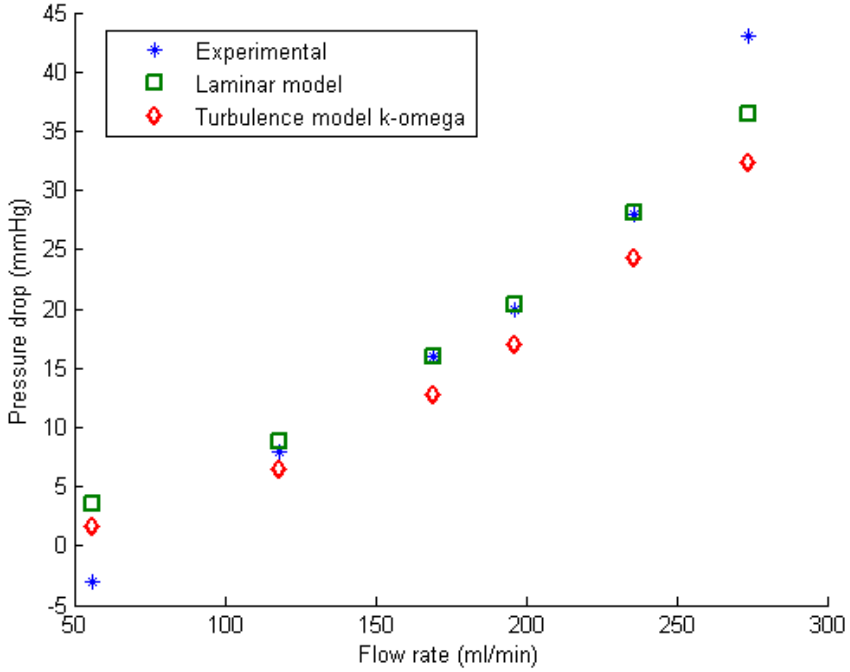

Figure 4.1-8: The total pressure drop as a function of flow rate for the 1.5 mm artery stenosis model. CFD simulations are compared to the experimental results. The first experimental measurement point indicates a measurement error since it shows an increase in pressure over the stenosis, which is physically unrealistic.

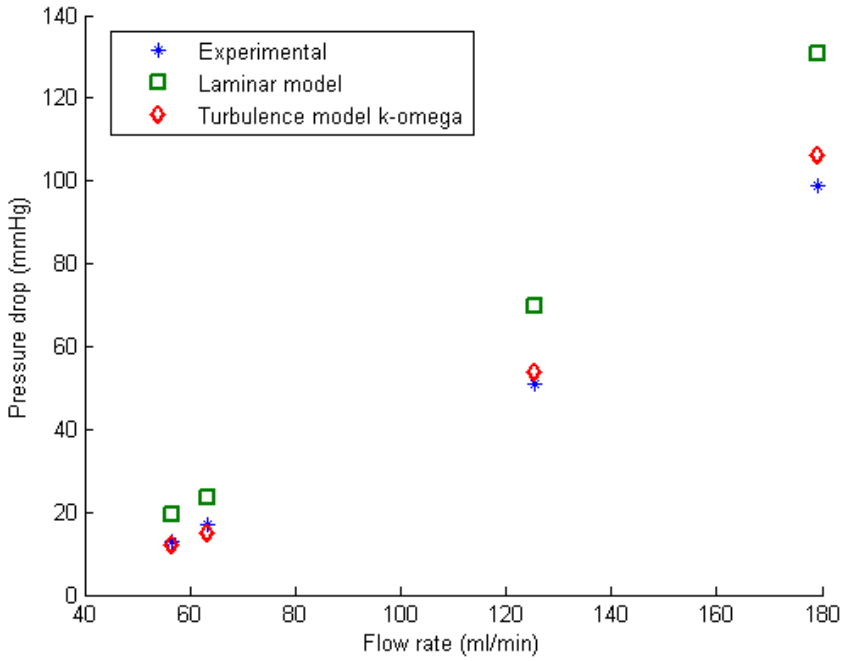

Figure 4.1-9: The total pressure drop as a function of flow rate for the aqueduct model, with the smooth narrowing proximal to the flow. CFD simulations are compared to the experimental results.

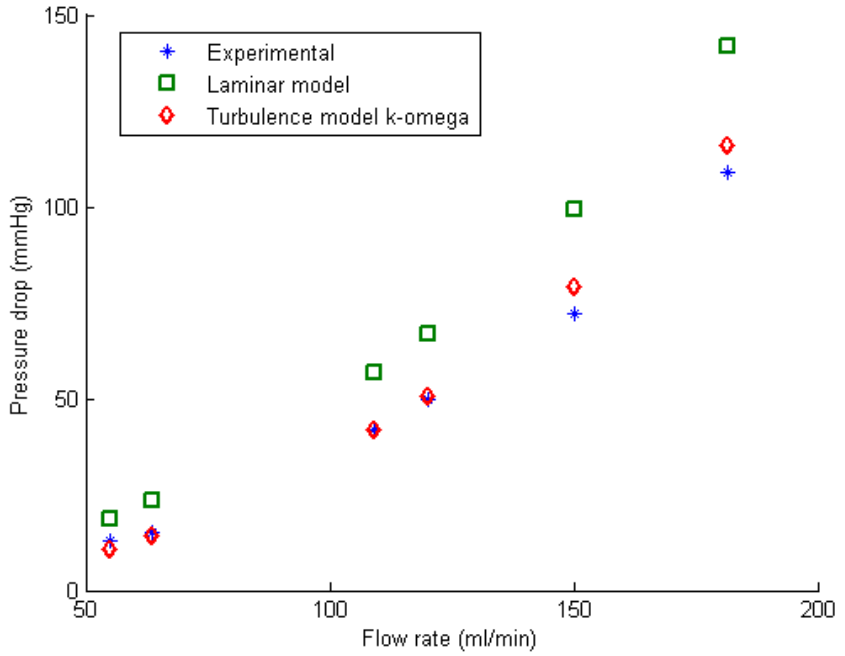

Figure 4.1-10: The total pressure drop as a function of flow rate for the aqueduct model, with the abrupt narrowing proximal to the flow. CFD simulations are compared to the experimental results.

4.2 Geometry Parameter Study

In the CFD simulations, the stenosis inlet and outlet angles were varied in order to investigate the resulting effects on the total pressure drop. The resulting pressure drops as a function of the outlet and inlet angles, respectively, can be seen in *Figure 4.2-1* and *Figure 4.2-2* for the laminar simulations and different Reynolds numbers. The results show that the total pressure drop increased for increasing values of the outlet angle. For larger angles, the outlet angle dependency diminished, resulting in approximately the same total pressure drop for angles over 40-50 degrees. The Reynolds number, within the tested range (450-1200), seemed to have an influence on the magnitude of the difference only, while the shape of the curve remained the same. This was in contrast to the results for the inlet angle investigation, where the pressure drop seemed to fluctuate slightly for different angles but showed no clear trend until the flow rate (or Reynolds number) was increased. For higher Reynolds numbers, the pressure drop was generally more sensitive to changes in the inlet and outlet angles. The turbulence model simulations yielded similar results as the laminar simulations, and are not presented.

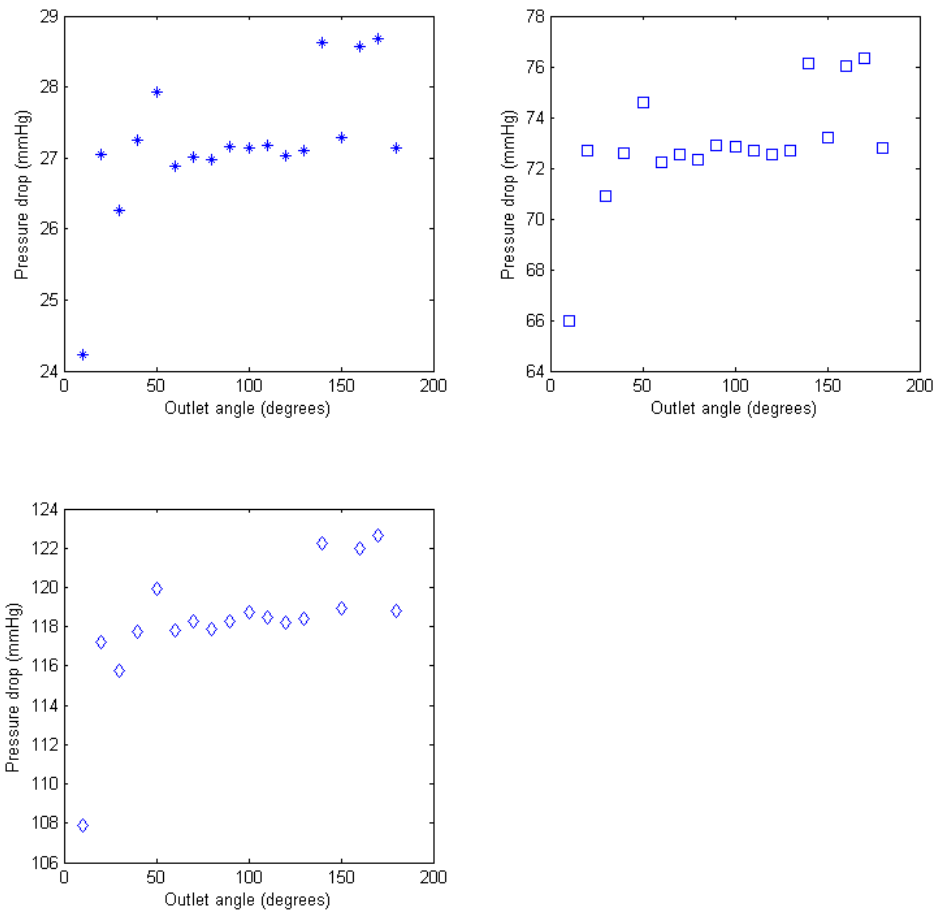

Figure 4.2-1: The total pressure drop as a function of the outlet angle for different Reynolds numbers (for CFD laminar flow simulations). The inlet angle was kept at an angle of 20 degrees. Re=459 (upper left), Re=852 (upper right) and Re=1134 (lower left). The Reynolds numbers correspond to the flow rates 70, 131 and 173 ml/min.

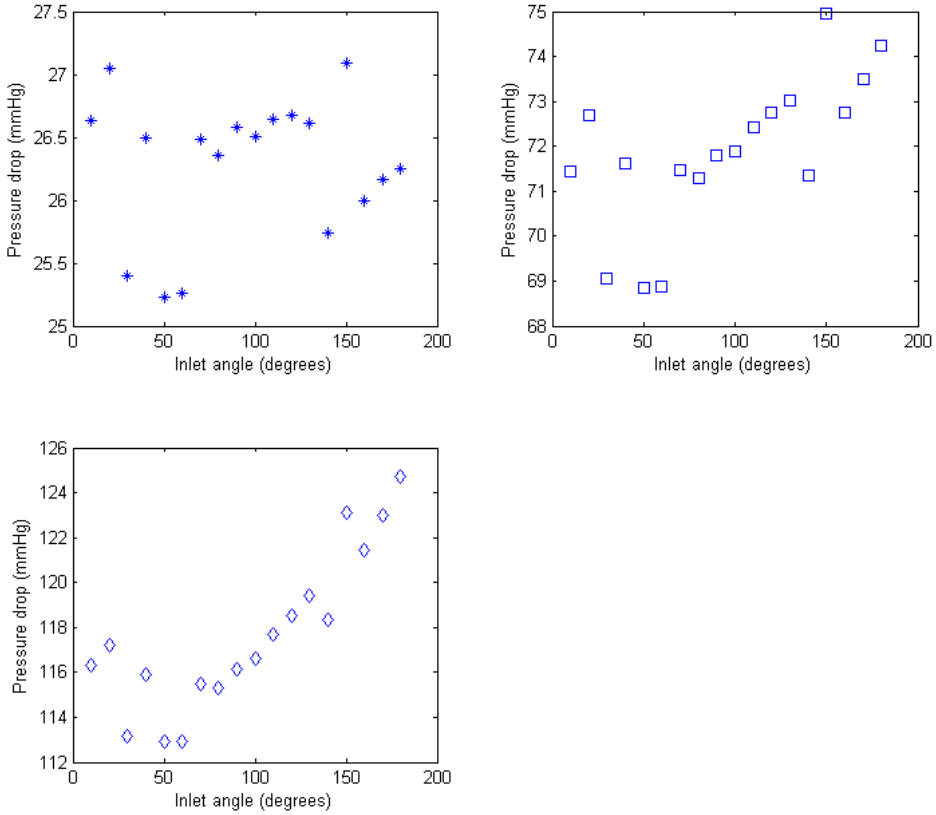

Figure 4.2-2: The total pressure drop as a function of the inlet angle for different Reynolds numbers (for CFD laminar flow simulations). The outlet angle was kept at an angle of 20 degrees. Re=459 (upper left), Re=852 (upper right) and Re=1134 (lower left). The Reynolds numbers correspond to the flow rates 70, 131 and 173 ml/min.

To further investigate geometrical effects, the stenosis diameter was varied in the laminar flow simulations to observe the change in total pressure drop over the aqueduct model (*Figure 4.2-3*). The results showed a strong diameter dependency, where an increase in the stenosis diameter by only three percent (i.e. 0.03 mm) yielded a total pressure drop that was considerably lower than that of the 1.0 mm stenosis diameter simulations. Turbulent flow simulations were also performed but yielded a similar reduction, thus those results are not presented.

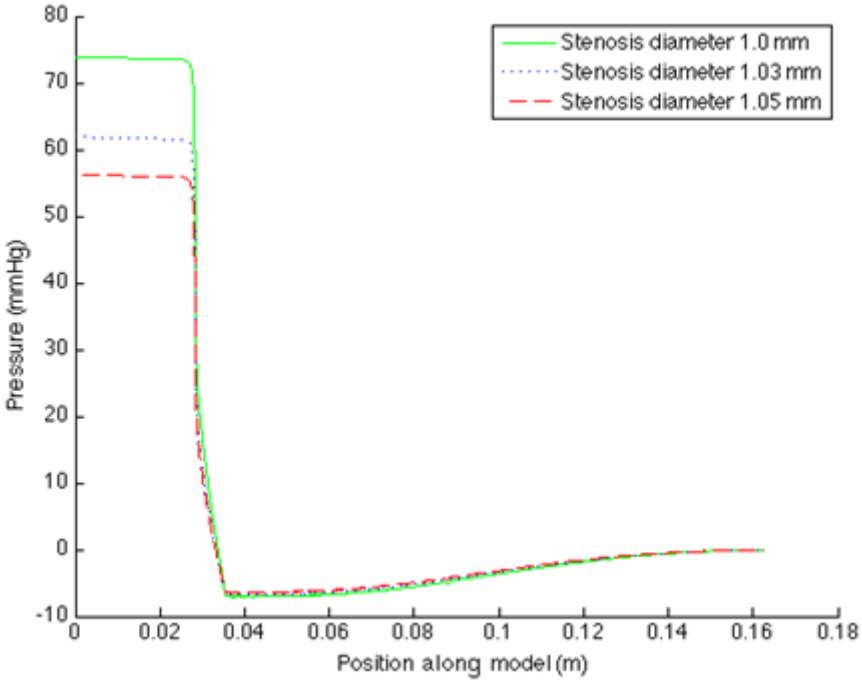

Figure 4.2-3: The pressure behavior for the aqueduct model, smooth inlet, for different stenosis diameters. The results are all extracted from laminar model CFD simulations under a constant flow rate of 130 ml/min.

4.3 Pulsatile effects on the pressure drop

The Womersley number for the problem configuration, according to (2.1.13), was approximately $\Omega \approx 3.86$, implying that a phase shift between the flow rate oscillations and the pressure gradient oscillations might be introduced, as well as possible damping of the flow rate oscillations. Since (2.1.13) only include parameters that were held constant, the Womersley number was the same for all measurements.

For the full pulse, corresponding to a volume of 0.4 ml, the laminar model simulations failed to converge while the turbulence model predicted a much higher peak-to-peak pressure drop than the experimental measurements showed (see *Figure 4.3-1* for the 1.0 mm artery model results). The results also showed that the predicted pressure drop curve was not symmetric, despite a symmetric sinusoidal flow rate input, where the crests were farther from the mean pressure drop value than the troughs.

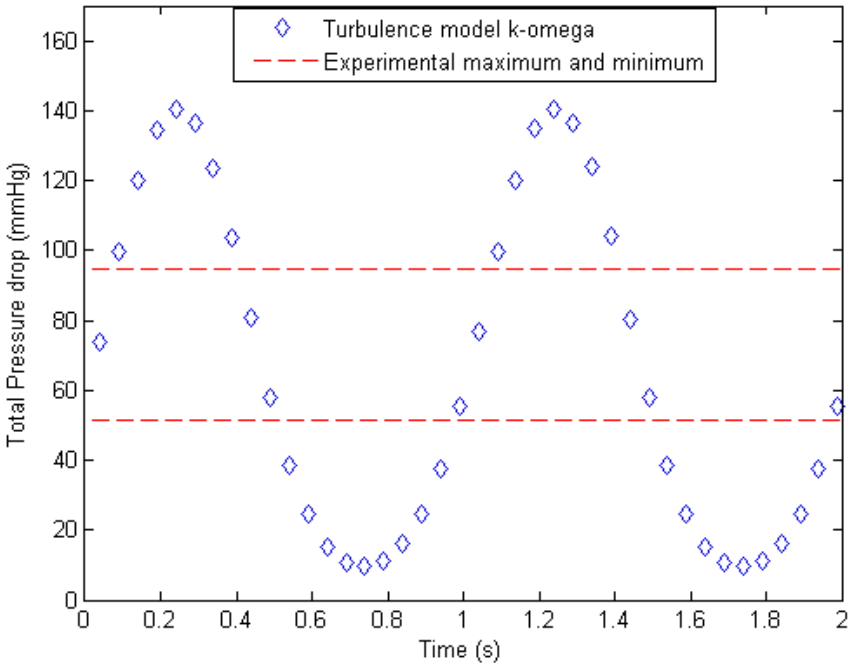

Figure 4.3-1: The total pressure drop as a function of time for pulsatile flow through the 1.0 mm artery stenosis model, corresponding to a volume pulse of 0.4 ml and a mean flow rate of 129 ml/min. A converging solution was only acquired for the $k-\omega$ turbulence model simulation.

The pulse size was investigated by applying the acquired pressure results from the laboratory experiments (from *Appendix E*) as a pressure inlet condition to the CFD models. The resulting flow rate behavior led to the conclusion that a pulse of 0.1 ml would yield approximately the correct pressure amplitude size, a serious reduction from 0.4 ml. The CFD results for this reduced pulse, together with the experimental results, can be seen in *Table 4.3-1*. The results showed that the systolic-diastolic differences (or peak-to-peak values) for the pressure drop were much closer to that of the experiments for the reduced pulse size of 0.1 ml compared to the full 0.4 ml pulse. The results also showed that the peak-to-peak pressure drop increased slightly for increasing mean flow rates, both in the experiments as well as in the CFD simulations, despite keeping the pulse size constant. In addition, the peak-to-peak pressure drop was found to be slightly larger for the abrupt inlet measurements compared to the smooth inlet measurements (true for the CFD simulations as well).

Table 4.3-1: The difference in systolic and diastolic pressure drops for the different models and mean flow rates. The CFD results represent a volume pulse of 0.1 ml and the experimental results a pulse of 0.4 ml.

Stenosis model	Mean flow rate (ml/min)	Experimental peak-to-peak pressure drop (mmHg)	Peak-to-peak pressure drop, laminar model (mmHg)	Peak-to-peak pressure drop, turbulence model (mmHg)
Aqueduct model, smooth inlet	130	39.2	36.5	31.6
Aqueduct model, abrupt inlet	131	39.5	39.1	33.1
Aqueduct model, smooth inlet	173	42.0	47.7	41.6
Aqueduct model, abrupt inlet	172	44.2	50.8	43.9
Artery model 1.0 mm	129	43.2	36.3	33.2

To further estimate how large the pulses through the stenosis models were in reality, the experimental results for the total pressure drop versus the flow rate, from the constant flow measurements (*Section 4.1.2* and *Appendix E*), were fit to polynomial functions (one for each stenosis model) in order to get a mathematical description of the flow rate dependency (see *Figure 4.3-2* and *Appendix F*). By inserting the maximum and minimum pressure drop values acquired from the pulsatile flow experiments into the resulting equations, the oscillatory flow rate amplitude (A_{osc}) was approximated. Equation (3.2.3) was then used to find the approximate volume of the pulses ($A_{osc} => V_{inserted}$). The collected results can be seen in *Table 4.3-2*. The results pointed to a major reduction in the volume pulse, relatively close to the pulse approximated by applying the pressure inlet condition in the simulations, for all stenosis models. Applying the same procedure to the pressure data from the previous study [4], where an extra resistance was added downstream of the stenosis outlet, the pulse size was estimated to have been even smaller than 0.1 ml.

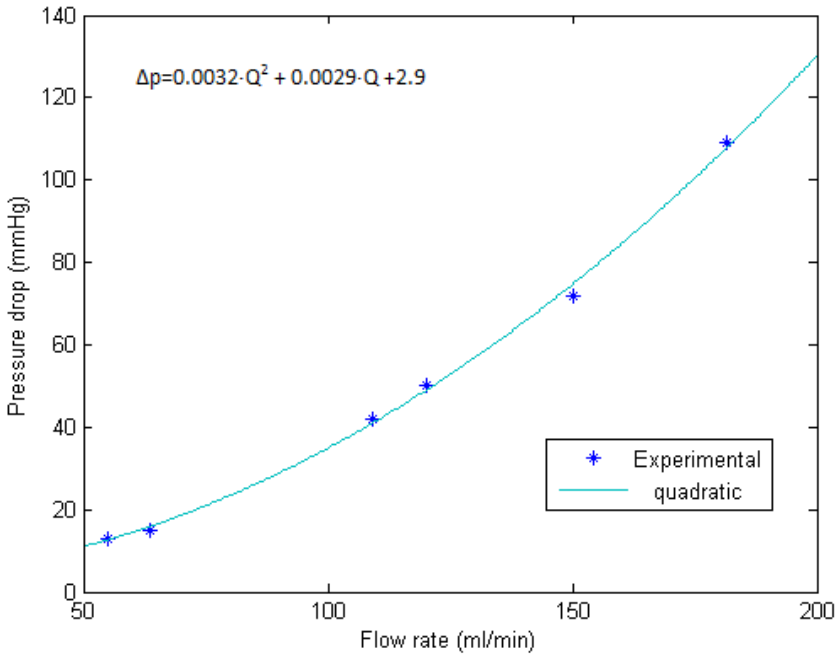

Figure 4.3-2: A quadratic fit for the pressure vs. flow rate data for the aqueduct model, with the abrupt narrowing proximal to the flow. The coefficient of determination, R^2, was 0.9983 for the quadratic fit.

Table 4.3-2: The estimated pulse volumes and the corresponding mean flow rates for the different stenosis models under pulsatile flow. The numbers in parenthesis are based on data from the study previously published [4].

Stenosis model	Mean flow rate (ml/min)	Estimated pulse volume (ml)
Aqueduct model, smooth proximal	131	0.13
Aqueduct model, abrupt proximal	132	0.12
Artery stenosis model 1.0 mm	129 (126)	0.11 (0.06)
Artery stenosis model 1.5 mm	(203)	(0.08)

4.4 Removing the catheter sensor

The total pressure drop was also measured with the *Likvor CELDA® System* so the catheter tip pressure sensor could be removed, simplifying the flow geometry. This was done to observe possible effects that the catheter tip pressure sensor had on the pressure drop. Since the *Likvor CELDA® System* only measured the total pressure drop, the pressure behavior inside the stenosis region could not be measured. The results for these additional measurements showed that the time-average of the total pressure drop, for pulsatile flow, was considerably lower for the no-catheter measurements compared to the measurements with the catheter, for similar flow rates (see *Figure 4.4-1*). There was a difference of about 30 mmHg between the two, for the 1.0 mm artery model, implying a major effect from the catheter tip pressure sensor. The graph in *Figure 4.4-1* also shows that the laminar simulations captured the difference in total pressure drop between the catheter and no catheter measurements.

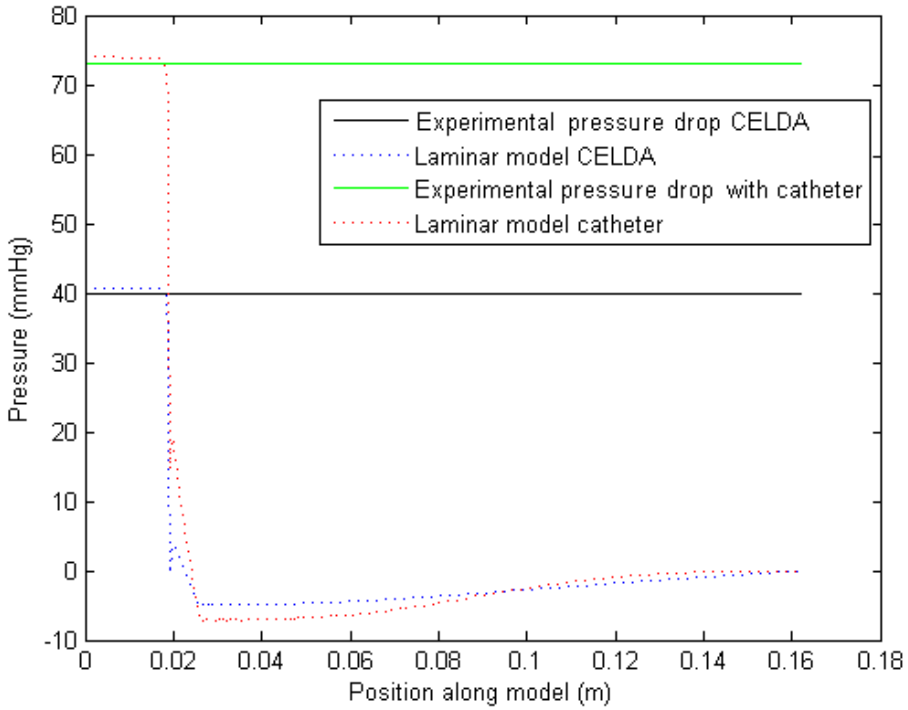

Figure 4.4-1: The time-averaged total pressure drop (one value) over the 1.0 mm artery stenosis model for pulsatile flow, with and without the catheter sensor (mean flow rates were 129 ml/min and 125 ml/min, respectively). The resulting pressure curves along the stenosis model for the laminar flow simulations are also included. CELDA corresponds to the no-catheter measurements.

For the *CELDA* measurements, low Reynolds number $k-\varepsilon$ turbulence model simulations were included in addition to the laminar and $k-\omega$ turbulence model simulations. The results for the 1.0 mm artery model can be seen in *Figure 4.4-2* and *Figure 4.4-3*, for a flow rate of 125 ml/min. The laminar and $k-\omega$ turbulence model results were very similar to the ones corresponding to the catheter measurements. The low Reynolds number model, however, predicted both the same pressure drop as seen in the experiments (approximately) and the steep adverse pressure gradient present during the catheter measurements.

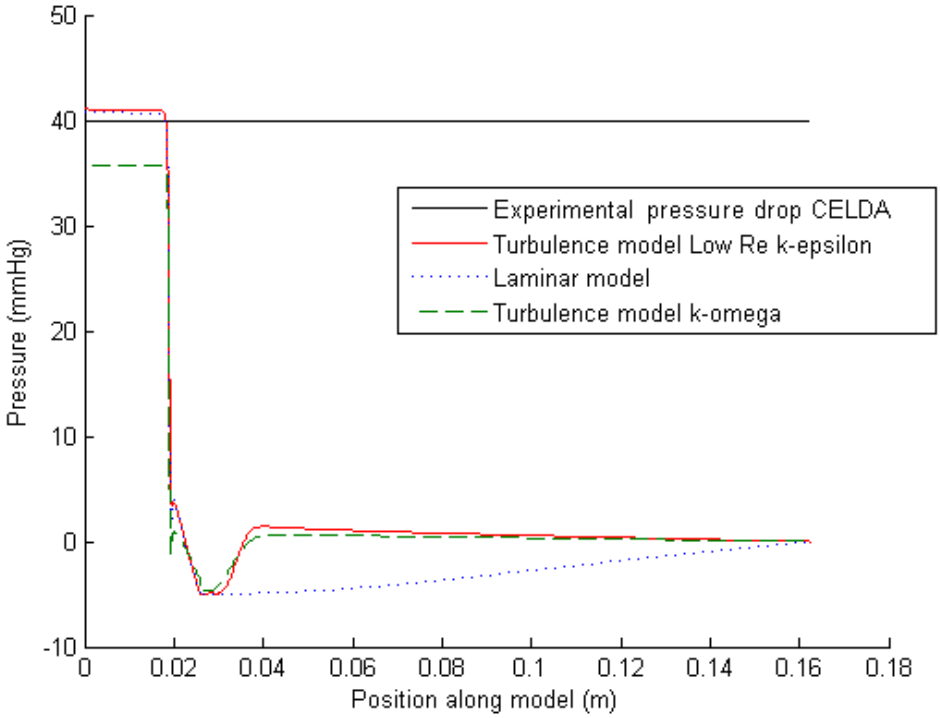

Figure 4.4-2: CFD results for the pressure along the 1.0 mm artery stenosis model and the experimentally estimated total pressure drop (one value) are presented. The results correspond to the no catheter (*CELDA*) measurements under pulsatile flow, mean flow rate 125 ml/min.

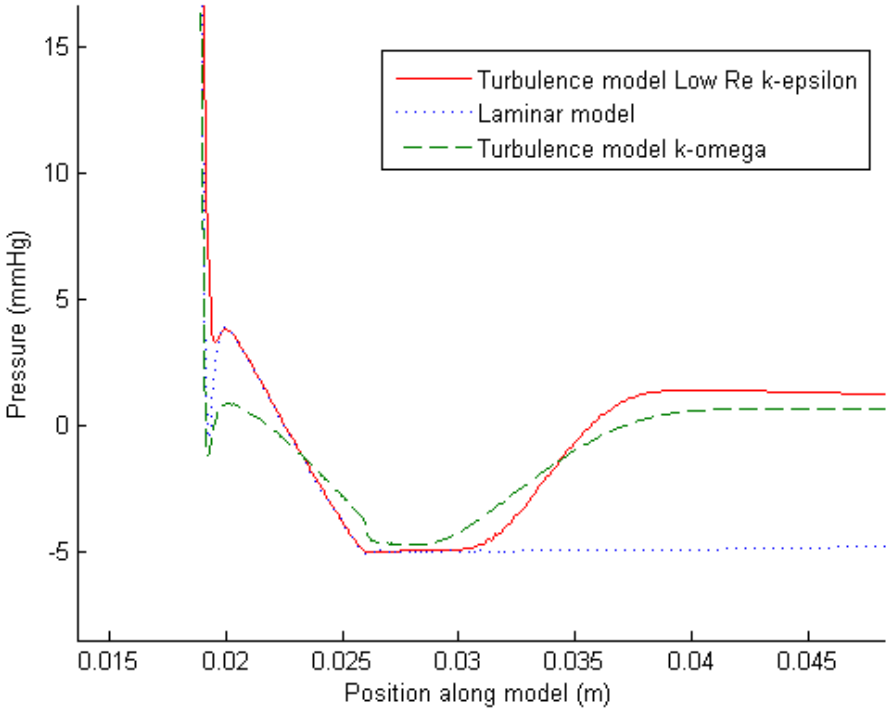

Figure 4.4-3: Close-up of the pressure along the 1.0 mm artery stenosis model corresponding to the no catheter (*CELDA*) measurements under pulsatile flow, mean flow rate 125 ml/min, for the CFD simulations.

5 Discussion and Conclusion

5.1 Discussion

The experimental results agreed with the ones previously found [4], including already established pressure behavior such as a major pressure decrease over the stenosis and a small pressure recovery downstream of the stenosis outlet (*Figure 4.1-2*, *Figure 4.1-5* and *Figure 4.1-6*). In addition, the results verified the occurrence of flow separation at the stenosis outlet for the stenosis models used, which was further implied by the CFD simulations (*Figure 4.1-1* to *Figure 4.1-6*). The precise length of the separation region at the stenosis outlet was difficult to determine due to the catheter tip pressure sensor being adjusted manually, but the length of the separation zone never exceeded 15 mm (see *Appendix E*). It is worth noting that the pressure fluctuated considerably just after the point of flow separation, especially for the measurements with the more abrupt stenosis outlet. Based on the constant flow measurements, the pressure drop seemed to have a slightly non-linear dependence on the flow rate within the tested flow interval (see *Appendix F*), something that was also implied by the approximated flow rate dependency in (2.1.10). Regarding flow regimes, the experimental measurements could not verify whether flow was laminar or turbulent. Based on the Reynolds numbers for the measurements (*Appendix C*) it is possible that both laminar and turbulent flow occurred during the measurements. However, the Reynolds numbers at the model inlet always predicted laminar inflow.

For the 1.0 artery model, the laminar simulations showed promise when used to determine the time-averaged pressure behavior up to the stenosis outlet, for pulsatile flow, but could not describe the observed pressure recovery correctly (*Figure 4.1-1*). For the constant flow measurements, the total pressure drop was close to the experimental results for both artery models, for intermediate flow rates that is (*Figure 4.1-7* and *Figure 4.1-8*). For the aqueduct model, the laminar flow simulations overestimated the pressure drop for both flow directions (*Figure 4.1-5*, *Figure 4.1-6*, *Figure 4.1-9* and *Figure 4.1-10*). However, the pressure inside the stenosis region was fairly close to the experimental values for this model as well. Thus if investigations of pressure inside the stenosis region are of interest, then the laminar model might suffice. However, the inability to correctly describe the behavior of the adverse pressure gradient (or pressure recovery) hinders studies of the flow downstream of the stenosis.

The turbulence $k-\omega$ model simulations better predicted the length of the separation zone (*Figure 4.1-1*, *Figure 4.1-5* and *Figure 4.1-6*) and yielded fairly accurate pressure drops for the aqueduct model while underestimating the pressure drop for the artery models (*Figure 4.1-7* to *Figure 4.1-10*). However, the wall lift-off (*Appendix D*) was quite large compared to the dimensions of the geometry, i.e. the model diameter, possibly indicating that the chosen turbulence model approach was not a good fit for this flow problem. The strange behavior in the stenosis region for the abrupt inlet simulation (*Figure 4.1-5*) further indicates this. However, without knowing for sure if the flow in the experiments was laminar or turbulent (or both), it is difficult to draw any final conclusions. Despite these facts, when comparing the resulting pressure behavior in the experiments with that of the CFD simulations, it is strongly indicated that, at least, the flow at the stenosis outlet was turbulent, and that turbulence modeling is needed in order to correctly describe the flow separation there (for the flow rates tested). The introduction of turbulence in stenoses, for laminar inflow, has also been discussed in similar studies [7, 37]. The introduction of turbulence was also indicated by the results

acquired for the *CELDA* measurements and the corresponding CFD simulations (*Figure 4.4-2* and *Figure 4.4-3*) where the low Reynolds $k-\varepsilon$ turbulence model predicted the expected pressure behavior along the entire stenosis model (if assuming similar pressure recovery as for the annulus/catheter measurements).

When investigating flow in both directions through the aqueduct model, the change in stenosis inlet/outlet geometry did not seem to have any major effect on the total pressure drop, although the pressure drop was slightly larger for the abrupt inlet, something both the experiments and laminar CFD simulations agreed on (*Table 4.1-1*). This is also consistent with the angle study of *Section 4*.2, based on CFD simulations. The results in *Figure 4.2-1* and *Figure 4.2-2* showed that the total pressure drop was not very sensitive to changes in the stenosis inlet and outlet shapes for angles over 40-50 degrees, except for high flow rates where the pressure drop was more sensitive to changes in the inlet angle. Thus having the abrupt inlet proximal to the flow is more likely to yield a slightly larger pressure drop since all stenosis models used in this thesis had angles above 40 degrees. The sensitivity at the inlet is reasonable, since more abrupt contractions can greatly affect the separation zone created there, while separation at the outlet happens immediately, unless the enlargement is very smooth. Similar results for the outlet angle have been shown in other publications [16, 38].

One important aspect that the experiments and the CDF simulations did not agree on is the difference in the total pressure drop between the 1.0 mm artery model and the aqueduct model (also 1.0 mm in stenosis diameter) that was observed during the experimental measurements (*Table 4.1-1*), for similar flow rates ($\approx 130\ ml/min$). This result was contradicted by the CFD simulations, where the difference in pressure drop between the two stenosis models was very small (*Table 4.1-1*). Since neither the results for the two flow directions (*Table 4.1-1*) nor the CFD angle study (*Figure 4.2-1* and *Figure 4.2-2*) could explain the observed pressure drop difference, it is unlikely that this difference was caused by different stenosis inlet/outlet shapes. One of the most important geometric parameters is the stenosis diameter, indicated both by the CFD diameter study (*Figure 4.2-3*) as well as the theoretical expressions (2.1.5) and (2.1.8). These results indicate that only a small diameter increase is needed for a notable decrease in pressure drop, at least when the catheter is present. Thus possible deviations in stenosis diameter, from 1.0 mm, in any of the models, could be a major contributor to the unexpected difference in pressure drop between the two stenosis models. Uncertainties in the pressure and flow rate measurements could also have contributed, but due to the low variations in both the pressure and flow measurements (see *Appendix E*) this would only explain a small part of the observed difference.

For the pulsatile flow measurements, the pressure variations, due to the oscillations, increased with increasing net flow rates (*Table 4.3-1*), both for the experimental measurements and CFD simulations, despite the fact that the pulse volume and the pulsation rate were kept constant. This result is in line with the theoretical expression in (2.1.15). The results also indicated a slight increase in the pressure variations for the abrupt inlet compared to the smooth inlet, though no major differences were observed (true for both the simulations and experimental measurements). The CFD simulations also indicated non-symmetrical pressure drop variations (*Figure 4.3-1*) despite the symmetrical flow rate input, which highlights the non-linear flow rate dependency. However, the pulses through the stenosis models were estimated to have been much smaller than those the syringe pump was programmed to produce. These damped oscillations could be due to elasticity of the tubes connecting the stenosis models to the syringe pump. The only way the pulsations could travel was within the flow line, thus making it probable that the tubes were expanded more and more as the

resistance increased at the stenosis end. This would agree with the fact that the estimated pulse sizes for the measurements from the previous study [4], where an extra resistance was added at the end of the stenosis models, were about half the size compared to the ones of this thesis (see *Table 4.3-2*). Other than elasticity, the Womersley number for the problem configuration, according to (2.1.13), also imply possible damping of the flow rate ($\Omega \approx 3.86$), though no such damping was observed in the CFD simulations. It is possible that the simulations were unable to recreate this effect, something that should be investigated by performing a frequency study, both experimentally and in the simulations.

5.2 Conclusions

This thesis has shown that flow separation takes place at the stenosis outlet, extending downstream of the point of separation, for all flow rates and stenosis models investigated. The CFD simulations showed that the laminar and turbulent flow simulations could not fully describe the velocity and pressure distributions throughout the stenosis models, separately, hence it is highly probable that a method that can handle both laminar and turbulent flow is needed. The low Reynolds number turbulence model implemented in *COMSOL* showed promising results on this front and warrants further investigation.

The peak-to-peak pressure drop ($\Delta p_{sys} - \Delta p_{dia}$) for pulsatile flow was shown to increase for increasing net flow rates, despite the fact that the pulse volume going through the stenosis models were kept at constant volume and pulsation rate. However, the results also indicated that the experimental approach introduced severely diminished pulse sizes, compared to what was expected. The most likely reasons for this are elasticity in the tubes along the flow line and/or damping due to the high frequency of the oscillations. Since knowledge of the oscillating flow rate is essential, the experimental setup should be further investigated and possibly revised.

For the aqueduct model, the pressure variations, and mean total pressure drop, showed a slight increase when the model was positioned with the abrupt stenosis inlet proximal to the flow, compared to the smooth inlet results, although no major difference was observed for the two flow directions. The CFD simulations further implied that the pressure drop was largely unaffected for large discharge angles, indicating that the transition has to be very smooth for there to be any substantial impact on the pressure drop, for the range of flow rates tested. The observed difference in pressure drop between the aqueduct model and the artery model of the same diameter could not be fully explained. The CFD simulations and the theoretical predictions indicated that the pressure drop was strongly dependent on the stenosis diameter, thus unexpected differences in the stenosis diameters is a likely reason for this observed difference in pressure drop. This also indicates that an accurate assessment of the stenosis diameter is of utmost importance when comparing pressure distributions for different stenosis models.

In addition, the chosen approach for measuring pressure inside the stenosis models (with the catheter pressure sensor) was shown to introduce a major increase in the total pressure drop as well as complicating the geometry of the problem, making simulations more difficult to perform.

5.3 Limitations and Future work

One of the main limitations of this thesis was the inability to confirm whether the flow in the experiments was laminar or turbulent. The collected results indicate the possibility of both types of flow, which makes simulations more difficult. Currently there are no turbulence models implemented in *COMSOL* that are designed with the aim to handle global flow transitions (from laminar flow to turbulent flow), but the low Reynolds $k-\varepsilon$ model showed promise when applied to the problem in question and should be evaluated further. It might also be a good idea to try additional turbulence models. One model worth trying is the low Reynolds $k-\omega$ model since it resolves the boundary layers and has been found to yield good results in similar studies [7, 37]. As of yet it is not implemented in *COMSOL*, but it could be implemented manually. Large Eddy Simulations (LES) could be an alternative, where the small scale turbulent eddies are modeled while the large scale turbulent eddies are computed directly. However, LES comes at a higher computational cost than the RANS approach, and the method is not implemented in *COMSOL* at this time. Another possible way to continue this project would be to try and manually introduce turbulence, in the experiments, to further evaluate the turbulence models tested in this thesis.

The experimental measurement method should be further evaluated due to elasticity of the tubes being a highly probable cause of the diminished pulsations. The effects of different pulsation frequencies should also be investigated to determine the frequency dependency. Another alternative could be to continue the CFD studies with elastic vessels. It is an advantage of *COMSOL* that it can handle combined physics problems (Multiphysics) such as fluid structure interactions (FSI), which is needed for studies of flow through elastic vessels. Furthermore, the ability to construct the geometry and the mesh in *COMSOL* makes the software easy to use and eliminates the need for additional meshing software. One of the disadvantages with *COMSOL* is that it might be slightly limited regarding options for transitional and turbulent flow, at this time. For this reason, other software with more options for CFD, and turbulence modeling in particular, could be of interest. Another option is to manually implement the desired turbulence models in *COMSOL*.

One additional problem with the current equipment is the need to insert a catheter for measuring pressure within the stenosis models. This complicates the geometry, and due to bending of the catheter, it is difficult to fully recreate this geometry in the simulations. In addition, if the diameter sensitivity is as strong as the CFD simulations suggest, when the catheter is included (*Figure 4.2-3*), it will be difficult to measure the stenosis diameters, of the experimental models, to the accuracy needed, since as little as tens of micrometers will have a major effect on the results. Despite these problems, the laminar flow simulations managed to capture the increase in the pressure drop (roughly 30 mmHg) due to the addition of the catheter, for the 1.0 mm artery model. Thus the approximation of a stationary and centered catheter (in the simulations) was indeed reasonable.

References

[1] World Health Organization (WHO). 2013. The 10 leading causes of death in the world 2000 and 2011, http://www.who.int/mediacentre/factsheets/fs310/en/, (Accessed 2013-09-12).

[2] Mount Sinai Hospital, New York. 2013. Fighting Coronary Artery Disease, http://www.mountsinai.org/patient-care/service-areas/heart/areas-of-care/heart-attack-coronary-artery-disease, (Accessed 2013-09-12).

[3] Cheng C, Tempel D, van HR, van der BA, Grosveld F, Daemen MJ, et al. Atherosclerotic lesion size and vulnerability are determined by patterns of fluid shear stress. *Circulation*. 2006 Jun 13;113(23):2744–53.

[4] Eklund A, Bäcklund T, Henein MY. Natural angioplasty as a mechanical effect of exercise. *International Journal of Cardiology*. 2013 Oct 3;168(3):3083-5.

[5] Cinalli G, Spennato P, Nastro A, Aliberti F, Trischitta V, Ruggiero C, Mirone G, Cianciulli E. Hydrocephalus in aqueductal stenosis. *Childs Nervous System.* 2011 Oct;27(10):1621-42.

[6] Malm J, Eklund A. Idiopathic normal pressure hydrocephalus. *Practical Neurology.* 2006;6:14-27.

[7] Ghalichi F, Deng X, De Champlain A, Douville Y, King M, Guidoin R. Low Reynolds number turbulence modeling of blood flow in arterial stenoses. *Biorheology*. 1998 Jul-Oct;35(4-5):281-94.

[8] Schirmer CM, Malek AM. Computational fluid dynamic characterization of carotid bifurcation stenosis in patient-based geometries. *Brain and Behavior*. 2012 Jan;2(1):42-52.

[9] Howden L, Giddings D, Power H, Aroussi A, Vloeberghs M, Garnett M, Walker D. Three-dimensional cerebrospinal fluid flow within the human ventricular system. *Computer Methods in Biomechanics and Biomedical Engineering*. 2008 Apr;11(2):123–133.

[10] Zamir M. 2000. *The Physics of Pulsatile Flow*. New York: Springer-Verlag New York, Inc. Chapter 1.

[11] Holman J.P. 1986. *Heat Transfer*. Sixth edition. McGraw-Hill, Inc. Chapter 5.

[12] Björklöf, D. 1991. *Givarteknik för mätning i processer*. First edition. Sweden: Almqvist och Wiksell. Chapter II-2.

[13] Moody L.F. Friction Factors for Pipe Flow, *Transactions of the ASME*. 1944 Nov;66(8): 671–684. Made available by the Department of Chemical Engineering, Michigan Technological University, Houghton, MI, and found at http://www.chem.mtu.edu/~fmorriso/cm310/MoodyLFpaper1944.pdf, Accessed (2013-10-24)

[14] Pontiga F, Gaytán SP. An experimental approach to the fundamental principles of hemodynamics. *Advances in Physiology Education*. 2005 Sep;29(3):165-171.

[15] Azzopardi, Barry J. Enlargement, flow and pressure change in. Thermopedia^{TM}. DOI: 10.1615/AtoZ.e.enlargement_flow_and_pressure_change_in.

[16] Rosa S, F.T. Pinho. Pressure drop coefficient of laminar Newtonian flow in axisymmetric diffusers. *International Journal of Heat and Fluid Flow*. 2006 April;27(2):319-328.

[17] Abdelall FF, Hahn G, Ghiaasiaan SM, Abdel-Khalik SI, Jeter SS, Yoda M, et al. Pressure drop caused by abrupt flow area changes in small channels. *Experimental Thermal and Fluid Science*. 2005 Apr;29(4):425-434.

[18] Rennels Donald C, Hudson Hobart M. 2012. *Pipe flow: A Practical and Comprehensive Guide.* Hoboken, New Jersey: John Wiley & Sons, Inc.

[19] Azzopardi, Barry J. Contraction, flow and pressure loss in. Thermopedia^{TM}. DOI: 10.1615/AtoZ.c.contraction_flow_and_pressure_loss_in.

[20] Oliviera P.J, Pinho F.T, Schulte A. A general correlation for the local loss coefficient in Newtonian axisymmetric sudden expansions. *International Journal of Heat and Fluid Flow*. 1998 Dec;19(6):655-660.

[21] Zamir M. 2000. *The Physics of Pulsatile Flow*. New York: Springer-Verlag New York, Inc. Chapter 4.

[22] Chung T.J. 2010. *Computational fluid dynamics*. Second edition. Cambridge: Cambridge university press. Chapter 2.

[23] COMSOL Multiphysics User's Guide Version 4.3. 2013. COMSOL. p. 683.

[24] COMSOL Multiphysics User's Guide Version 4.3. 2013. COMSOL. p. 699.

[25] Chung T.J. 2010. *Computational fluid dynamics*. Second edition. Cambridge: Cambridge university press. Chapter 21.

[26] Wilcox David C. 1998. *Turbulence Modeling for CFD*. Second edition. Anaheim: DCW Industries.

[27] Figure from Wikipedia. 2013. Law of the wall (English). http://en.wikipedia.org/wiki/File:Law_of_the_wall_(English).svg. (Accessed in 2013-09-30). This file is licensed under the Creative Commons Attribution-Share Alike 3.0 Unported and 2.5 Generic license found at http://creativecommons.org/licenses/by-sa/3.0/deed.en. Author: aokomoriuta.

[28] CFD Module User's Guide. 2013. COMSOL. p. 127.

[29] CFD Module User's Guide. 2013. COMSOL. p. 132-133.

[30] COMSOL Multiphysics User's Guide Version 4.3. 2013. COMSOL. p. 676.

[31] Figure from Wikipedia. 2013. Finite element 1D illustration2. http://en.wikipedia.org/wiki/File:Finite_element_method_1D_illustration2.svg. (Accessed in 2013-09-30). This file is licensed under the Creative Commons Attribution-Share Alike 3.0 Unported licence (http://creativecommons.org/licenses/by-sa/3.0/deed.en). Author: Krishnavedala.

[32] COMSOL Multiphysics User's Guide Version 4.3. 2013. COMSOL. p. 675-676.

[33] CFD Module User's Guide. 2013. COMSOL. p. 119-120.

[34] CFD Module User's Guide. 2013. COMSOL. p. 104-105.

[35] CFD Module User's Guide. 2013. COMSOL. p. 105-106.

[36] CFD Module User's Guide. 2013. COMSOL. p. 106-107.

[37] Varghese SS, Frankel SH. Numerical modeling of pulsatile turbulent flow in stenotic vessels. *Journal of Biomechanical Engineering*. 2003 Aug;125(4):445-60.

[38] Rennels Donald C, Hudson Hobart M. 2012. *Pipe flow: A Practical and Comprehensive Guide.* Hoboken, New Jersey: John Wiley & Sons, Inc. Chapters 10 and 11.

Appendices

Appendix A

Derivation of annulus pressure drop

By starting with the Navier-Stokes system of equations for incompressible flow of a Newtonian fluid (here in differential form)

$$\nabla \cdot \vec{u} = 0 \tag{A.1}$$

$$\rho\left(\frac{\partial \vec{u}}{\partial t} + \vec{u} \cdot \nabla \vec{u}\right) = -\nabla p + \mu \nabla^2 \vec{u} + \vec{f}, \tag{A.2}$$

where ∇ is the del operator, the pressure drop can be derived for constant laminar flow through a straight annulus. Since the geometry in this thesis was placed horizontally and no outer body forces, other than gravity, were present, the f term vanishes. By using cylindrical coordinates, equation (A.1) becomes

$$\frac{1}{r}\frac{\partial(\rho r u_r)}{\partial r} + \frac{1}{r}\frac{\partial(\rho u_\theta)}{\partial \theta} + \frac{\partial(\rho u_z)}{\partial z} = 0. \tag{A.3}$$

By assuming that the only non-zero velocity component is in the direction of the flow (i.e. along the z-axis), and making use of axial symmetry (no angle dependency), equation (A.3) reduces to

$$\frac{\partial u_z}{\partial z} = 0. \tag{A.4}$$

Using (A.4) the momentum equations (A.2) for steady flow are reduced to

$$\mu\left[\frac{1}{r}\frac{d}{dr}\left(r\frac{du_z}{dr}\right)\right] = \frac{\partial p}{\partial z} \tag{A.5}$$

$$-\frac{\partial p}{\partial r} = 0. \tag{A.6}$$

Because of (A.6) and axial symmetry, it can be seen that the pressure only changes in the z-direction. In addition, for fully developed steady flow, the velocity does not change in the direction of the flow, implying that u_z is a function of r only. Since the LHS of (A.5) only depends on r and the RHS only depends on z, both sides of (A.5) must be constant. Integrating (A.5) with respect to r yields

$$u_z = -\frac{1}{4\mu}\left(-\frac{\partial p}{\partial z}\right)r^2 + c_1 lnr + c_2 \tag{A.7}$$

where the constants c_1 and c_2 are determined by the boundary conditions at the walls ($u_z = 0$)

=> $$u_z = \frac{1}{4\mu}\left(-\frac{\partial p}{\partial z}\right)\left[\frac{\ln\left(\frac{r}{r_1}\right)}{\ln\left(\frac{r_2}{r_1}\right)}(r_2^2 - r_1^2) - (r^2 - r_1^2)\right] \tag{A.8}$$

with r_1 and r_2 being the smaller and larger radius of the annulus pipe, respectively. Integrating (A.8) over the cross-section of the pipe

$$Q = \int_{r_1}^{r_2} u_z(r) 2\pi r dr \tag{A.9}$$

gives an expression for the flow rate

$$Q = \frac{\pi(r_2^2 - r_1^2)}{8\mu}\left(-\frac{\partial p}{\partial z}\right)\left[r_2^2 + r_1^2 - \frac{r_2^2 - r_1^2}{\ln\left(\frac{r_2}{r_1}\right)}\right]. \tag{A.10}$$

Since the pressure gradient in the z-direction is constant, it can be expressed as

$$-\frac{\partial p}{\partial z} = const = \frac{\Delta p}{L} \tag{A.11}$$

where L is the length of the pipe section and Δp is the pressure difference over the same section. Together (A.10) and (A.11) yield the final expression for the pressure drop

$$\Delta p = \frac{8\mu Q L}{\pi(r_2^2 - r_1^2)}\left[\frac{\ln\left(\frac{r_2}{r_1}\right)}{(r_1^2 + r_2^2)\ln\left(\frac{r_2}{r_1}\right) - (r_2^2 - r_1^2)}\right], \tag{A.12}$$

$$r_1 \leq r \leq r_2$$

which is equivalent to (2.1.7). Inserting (A.12) in (A.8) yields the velocity profile described by (2.1.12).

NOTE: In a similar fashion, the pressure drop and velocity profile for Poiseuille flow can be derived using the same principles and starting equations.

Appendix B

The mesh study

The computational mesh, dividing the computational domain into smaller elements, was evaluated in order to minimize errors in the CFD simulations. Since the geometry of the problem contained sharp edges at the stenosis inlet and outlet, mesh refinements were made in those areas. In addition, the mesh was refined along the line of flow separation, similar to the mesh constructed in the *COMOL* model library file: *Turbulent flow over a backward facing step*[3] (see *Figure B-1*). In addition, the number of finite elements (and thus also the number of degrees of freedom) was increased, in succession, to investigate whether the quantities of interest (pressure drop and recirculation length) were dependent on the mesh chosen. These mesh studies, for the different stenosis models, are presented below (*Table B-1* to *Table B-6*). The results show that the solution was mesh dependent, since the quantities of interest varied even for very fine meshes that consisted of a large amount of elements. In addition, the recirculation length for the laminar model simulations increased when the number of elements was increased, which is the opposite of what was expected, since the laminar model already overestimated the recirculation length for coarse meshes. Thus the pressure drop was the primary quantity considered when choosing the mesh, and the recirculation length was the secondary. However, the pressure drop seemed to fluctuate even for very dense meshes, but these fluctuations were quite small even when comparing the finest and coarsest meshes. Thus, for all models, a slightly coarser mesh was chosen to improve the simulation speed, settling for a number of degrees of freedom around 500k. The turbulence model studies for the 1.5 mm artery stenosis model and aqueduct model with smooth inlet were very similar to the ones seen in *Table B-5* to *Table B-6* and are not presented.

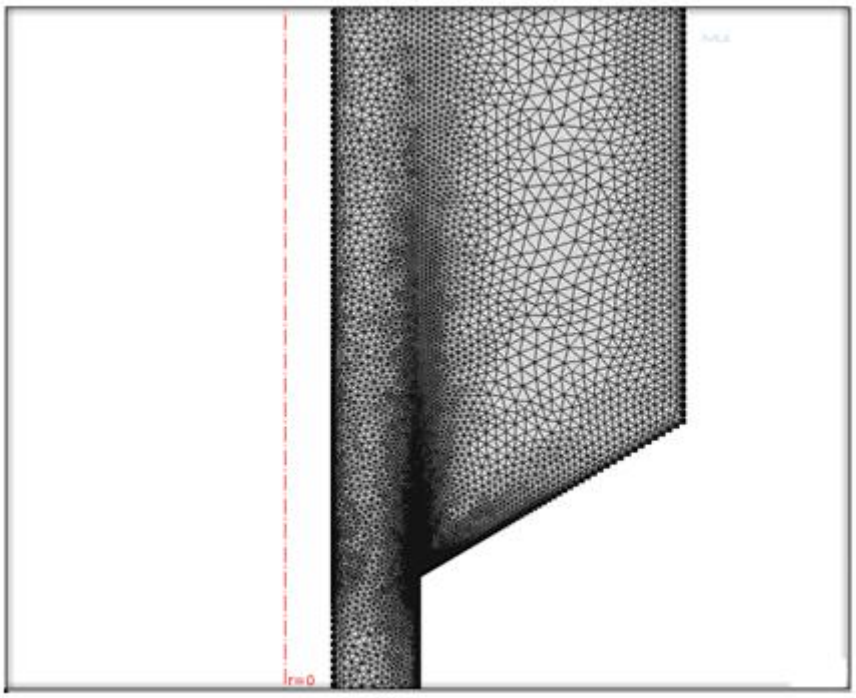

Figure B-1: The mesh refinements along the line of flow separation. The red dashed line represents the boundary of axial symmetry.

[3] The model can be found in the CFD Module Library Manual (2013).

Table B-1: Mesh study for the laminar simulations applied to the 1.0 mm artery stenosis model and for a flow rate of 129 ml/min. Brown represents the mesh chosen.

Physics induced setting	Domain mesh setting	Boundary mesh setting	Total Pressure drop (mmHg)	Point of reattachment along the model (m)	Number of domain elements	Degrees of freedom
Normal	Coarse	Fine	72,52	0,104	72670	128997
Fine	Normal	Finer	71,64	0,114	123943	211317
Finer	**Fine**	**Extra fine**	**73,99**	**0,14**	**305578**	**508686**
Extra fine	Finer	Extremely fine	72,9	0,1585	750381	1219953
Extremely fine	Extra fine	Extremely fine	72,71	0,1615	1376404	2160810

Table B-2: Mesh study for the laminar simulations applied to the 1.5 mm artery stenosis model and for a flow rate of 203 ml/min. Brown represents the mesh chosen.

Physics induced setting	Domain mesh setting	Boundary mesh setting	Total Pressure drop (mmHg)	Point of reattachment along the model (m)	Number of domain elements	Degrees of freedom
Normal	Coarse	Fine	21,155	0,089	67208	120906
Fine	Normal	Finer	21,842	0,092	130856	221832
Finer	**Fine**	**Extra fine**	**21,658**	**0,1055**	**307099**	**511428**
Extra fine	Finer	Extremely fine	20,965	0,1162	737221	1200795
Extremely fine	Extra fine	Extremely fine	21,24	0,117	1382746	2171025

Table B-3: Mesh study for the laminar simulations applied to the aqueduct model (smooth stenosis inlet) and for a flow rate of 130 ml/min. Brown represents the mesh chosen.

Physics induced setting	Domain mesh setting	Boundary mesh setting	Total Pressure drop (mmHg)	Point of reattachment along the model (m)	Number of domain elements	Degrees of freedom
Normal	Coarse	Fine	70,98	0,1383	69525	124416
Fine	Normal	Finer	71,98	0,1383	116847	200811
Finer	**Fine**	**Extra fine**	**74,3**	**0,155**	**324098**	**536886**
Extra fine	Finer	Extremely fine	73,54	>0.173	747355	1215660

Table B-4: Mesh study for the laminar simulations applied to the aqueduct model (abrupt stenosis inlet) and for a flow rate of 131 ml/min. Brown represents the mesh chosen.

Physics induced setting	Domain mesh setting	Boundary mesh setting	Total Pressure drop (mmHg)	Point of reattachment along the model (m)	Number of domain elements	Degrees of freedom
Normal	Coarse	Fine	77,395	0,1287	67777	121833
Fine	Normal	Finer	76,69	0,129	111037	191943
Finer	**Fine**	**Extra fine**	**76,42**	**0,1605**	**275216**	**463638**
Extra fine	Finer	Extremely fine	77,77	0,1635	790486	1280883

Table B-5: Mesh study for the turbulence model simulations applied to the 1.0 mm artery stenosis model and for a flow rate of 129 ml/min. Brown represents the mesh chosen.

Physics induced setting	Domain mesh setting	Boundary mesh setting	Total Pressure drop (mmHg)	Point of reattachment along the model (m)	Number of domain elements	Degrees of freedom
Normal	Coarse	Fine	60,445	0,0365	90229	297255
Fine	**Normal**	**Finer**	**58.53**	**0.0365**	**139505**	**439865**
Finer	Fine	Extra fine	59,41	0,0365	378614	1129050

Table B-6: Mesh study for the turbulence model simulations applied to the aqueduct model (abrupt stenosis inlet) and for a flow rate of 131 ml/min. Brown represents the mesh chosen.

Physics induced setting	Domain mesh setting	Boundary mesh setting	Total Pressure drop (mmHg)	Point of reattachment along the model (m)	Number of domain elements	Degrees of freedom
Normal	Coarse	Fine	57,7	0,0387	85705	285670
Fine	**Normal**	**Finer**	**57,26**	**0,0387**	**133356**	**423120**
Finer	Fine	Extra fine	57,0	0,0386	330437	1008305

Appendix C

The Reynolds numbers

The Reynolds number was calculated using equation (2.1.1) in both parts of the stenosis models, i.e. the regular tube section and the stenosis region, for all measurements performed (see *Table C-1* to *Table C-5*). The effective diameter of the model tube and stenosis region were used as the characteristic length for respective regions and the mean velocities were calculated from (2.1.2) using the known flow rate and cross-sectional areas. The Reynolds numbers predicted laminar inflow for all measurements performed, while the Reynolds numbers within the stenosis region either bordered or surpassed the lower limit of the transition region for cylindrical pipe flow, i.e. $Re > 2000$. The only exceptions were the constant flow measurements with the lowest flow rates, where the Reynolds numbers were clearly below 2000 in both regions. Due to these facts, it is difficult to determine whether the flow was laminar, turbulent or both (i.e. transitional). It is also possible that the inserted catheter sensor introduced some degree of turbulence.

Table C-1: The average Reynolds numbers for the pulsatile flow measurements.

Model	Mean flow rate (ml/min)	Inlet Reynolds number	Stenosis Reynolds number
Aqueduct smooth inlet	130	864	2135
Aqueduct abrupt inlet	131	871	2152
Artery 1.0 mm	129	858	2119
Aqueduct smooth inlet	173	1150	2841
Aqueduct sharp inlet	172	1143	2825

Table C-2: The Reynolds numbers for the constant flow measurements with the 1.0 mm artery stenosis model.

Flow rate (ml/min)	Inlet Reynolds number	Stenosis Reynolds number
58	386	953
119	791	1955
150	997	2464
194	1290	3186

Table C-3: The Reynolds numbers for the constant flow measurements with the 1.5 mm artery stenosis model.

Flow rate (ml/min)	Inlet Reynolds number	Stenosis Reynolds number
56	372	673
118	784	1417
169	1124	2030
196	1303	2354
236	1569	2834
274	1822	3291

Table C-4: The Reynolds numbers for the constant flow measurements with the aqueduct model (smooth narrowing as stenosis inlet).

Flow rate (ml/min)	Inlet Reynolds number	Stenosis Reynolds number
57	379	936
63	419	1035
126	838	2070
179	1190	2940

Table C-5: The Reynolds numbers for the constant flow measurements with the aqueduct model (abrupt narrowing as stenosis inlet).

Flow rate (ml/min)	Inlet Reynolds number	Stenosis Reynolds number
55	366	903
64	425	1051
109	725	1790
120	798	1971
150	997	2464
182	1210	2989

Appendix D

The velocity profiles

The velocity profiles just upstream of the stenosis inlet for the CFD simulations were compared to the theoretical expressions presented in *Chapter 2*. The results show that the laminar model closely predicted the Poiseuille velocity profile (*Figure D-1*), while there was a minimal difference between the laminar model and the theoretical expression for annulus flow (*Figure D-2*). The turbulence $k-\omega$ model made use of wall functions, thus the velocity was not zero at the grid points closest to the wall (*Figure D-3*). The velocity profile was also much flatter when compared to the laminar flow profile, which is a trademark for turbulent flow. Since no well known expression for the turbulent velocity profile in an annulus could be found, there were no theoretical expressions to compare to. The low Reynolds number model, which was applied only for the no-catheter simulations, showed a velocity profile in between the laminar and the fully turbulent analytical profiles (*Figure D-4*). It is worth noting that if the turbulence intensity was lowered at the inlet, then the velocity profile from the low Reynolds number model simulation coincided with the theoretical expression for laminar flow. But because of the low intensity, the solution did not fully converge and thus it is not presented.

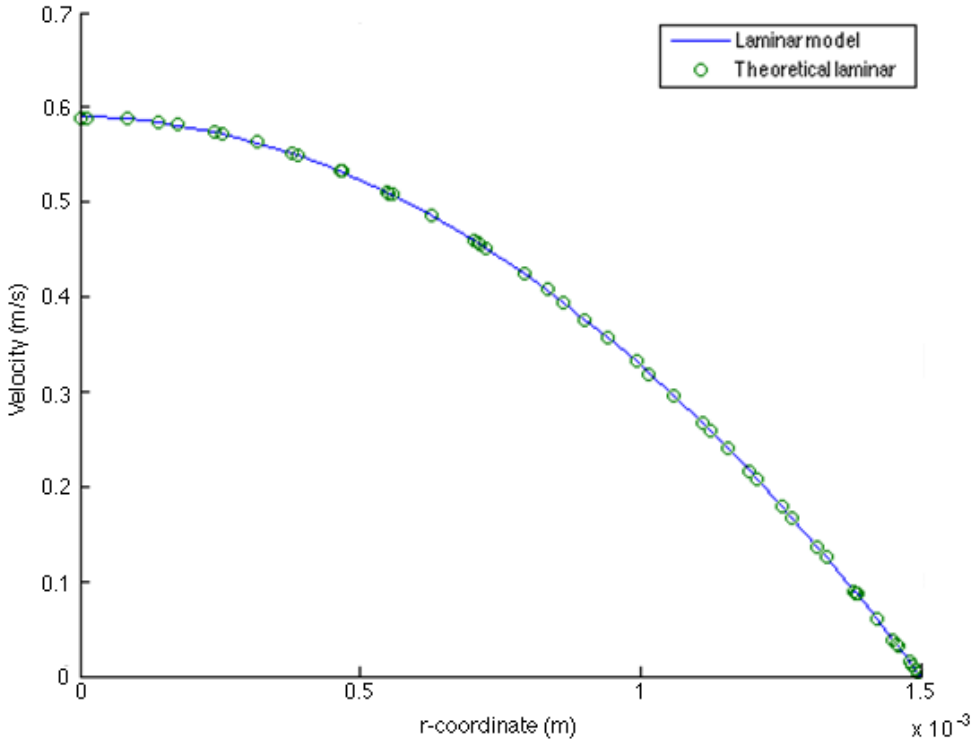

Figure D-1: The velocity profile for cylindrical pipe flow right before the stenosis inlet according to the theoretical expression for laminar flow (circles) and the laminar CFD simulations (line). The flow rate was 125 ml/min.

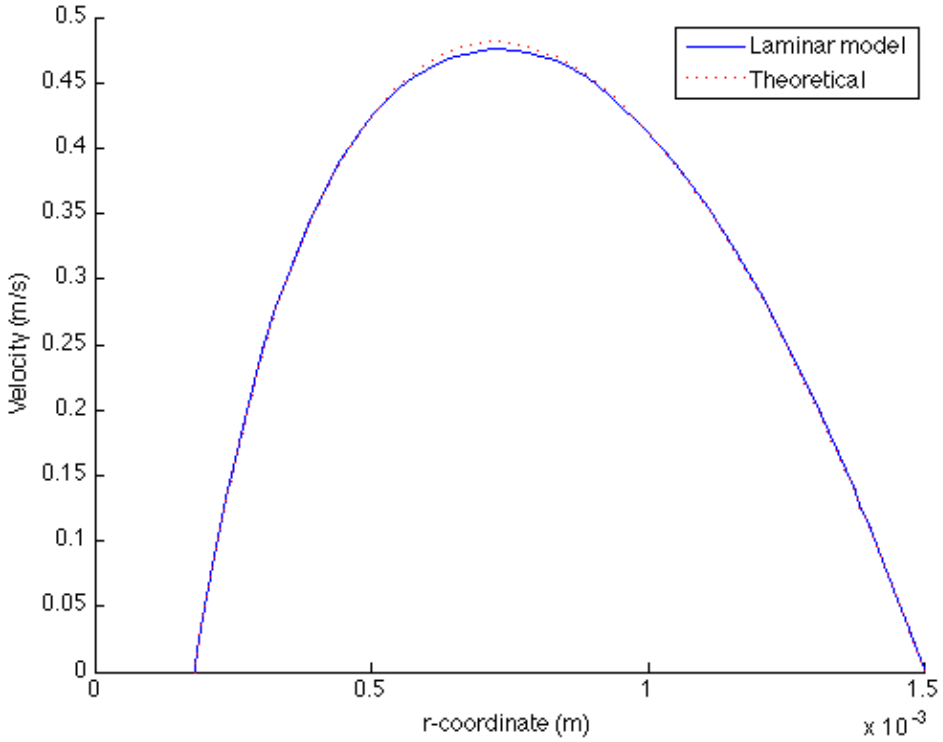

Figure D-2: The velocity profile for annulus flow right before the stenosis inlet according to the theoretical expression for laminar flow (dotted line) and the laminar CFD simulations (full line). The flow rate was 129 ml/min.

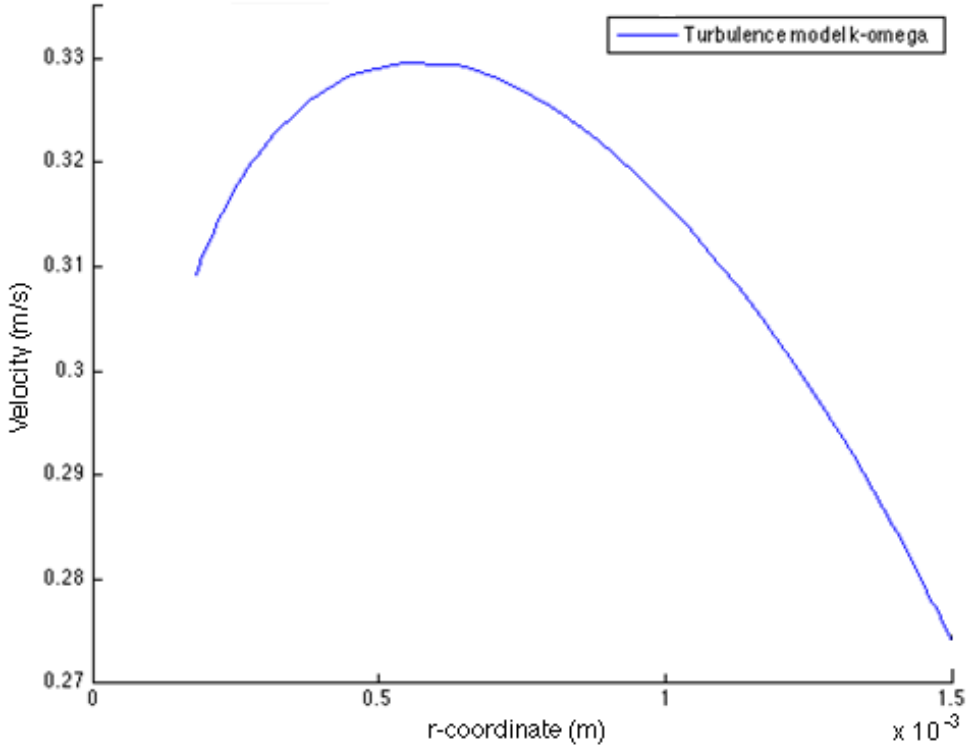

Figure D-3: The velocity profile for annulus flow right before the stenosis inlet according to the turbulent $k-\omega$ model simulations. The flow rate was 129 ml/min.

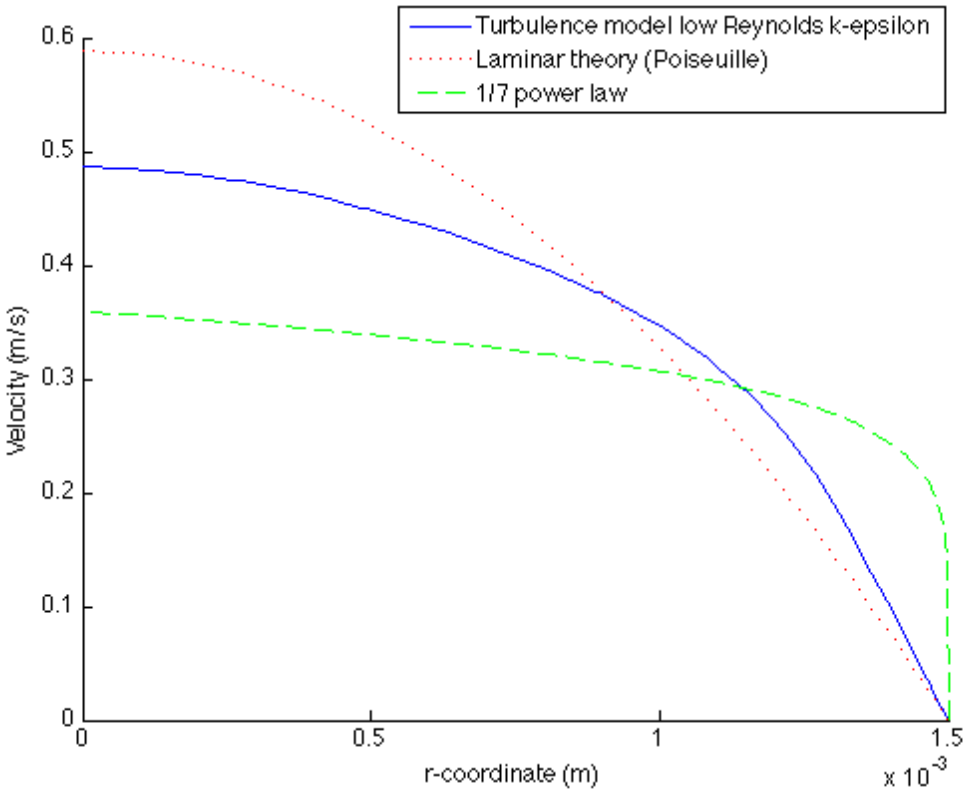

Figure D-4: The velocity profile for cylindrical pipe flow right before the stenosis inlet according to the theoretical expression for laminar flow (dotted), the low Reynolds $k-\varepsilon$ model simulations (full), and the 1/7th power law (dashed). The flow rate was 129 ml/min.

Poiseuille and annulus pressure drops

To further evaluate the accuracy of the CFD simulations, the pressure drop for straight channels was investigated for both Poiseuille and annulus flow. This was accomplished by removing the non-linear term in the Navier-Stokes equations (2.2.7) in the CFD simulations, creating what is known as Stokes flow, hence removing any convective effects. All pressure losses can then approximately be described by the expressions in (2.1.6) and (2.1.7) for Poiseuille and annulus flow, respectively. The results (*Table D-1*) showed that the pressure gradients (i.e. $\Delta p/L$) acquired by CFD were close to the theoretical values, for all parts of the stenosis model geometry. The largest difference was observed for the annulus stenosis region. However, the effects of this difference did not yield any major difference in the pressure drop because of the short length of the stenosis (*Figure D-5*). The same comparison was made for a finer mesh but it did not affect the results. It should also be noted that the catheter did not occupy the final stretch to the model outlet, hence the comparison with the Poiseuille pressure gradient in *Figure D-5*. The differences between the theoretical and CFD pressure gradients are likely due to the flow not being fully developed everywhere in the simulations (the theory is based on fully developed flow).

Table D-1: The theoretical and laminar flow simulation pressure gradients in the artery 1.0 mm stenosis model, neglecting convective effects. For annulus flow, the smaller diameter corresponded to the catheter diameter (0.36 mm). The flow rate was 129 ml/min.

Type of flow	Theoretical pressure gradient $\Delta p/L$ (mmHg/m)	Laminar model pressure gradient $\Delta p/L$ (mmHg/m)
Poiseuille flow, diameter 3.0 mm	-7.71	-7.69
Annulus flow, large diameter 3.0 mm	-14.23	-14.29
Annulus flow, large diameter 1.0 mm	-2583	-2680

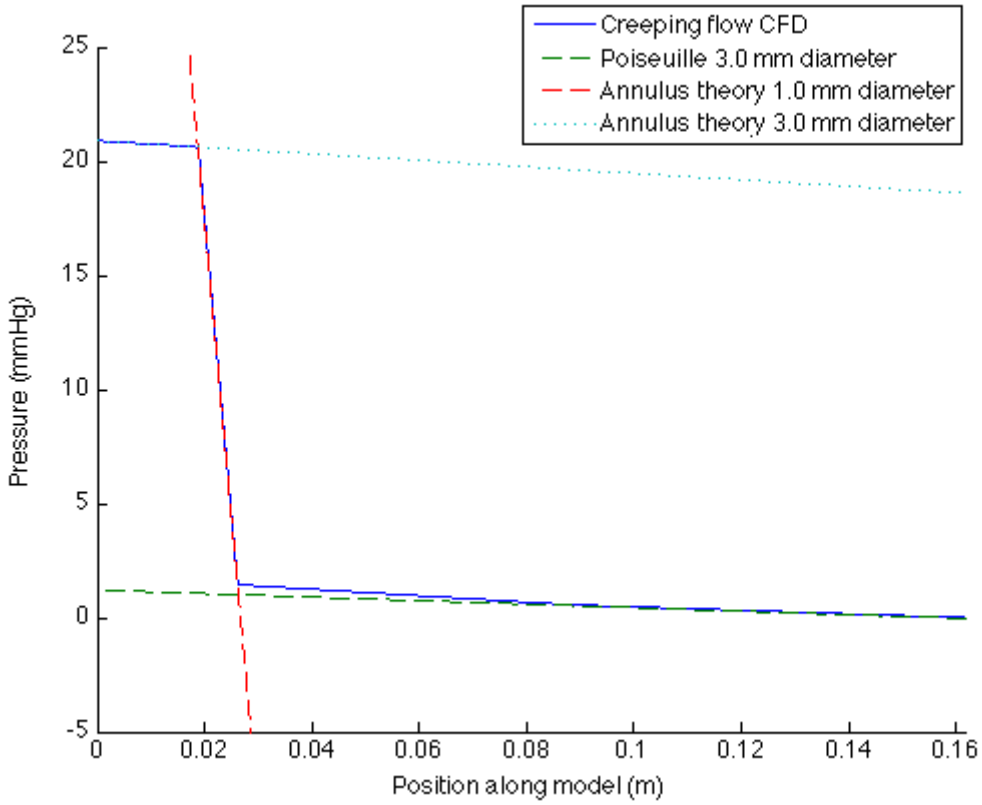

Figure D-5: Comparison of the pressure gradients for the CFD simulations and theoretical relations for cylindrical (Poiseuille) and annulus flow when convective effects have been neglected. The results correspond to the 1.0 mm artery model and a flow rate of 129 ml/min. The diameters for annulus flow presented in the legend correspond to the larger diameter of the annulus, the smaller diameter corresponded to the catheter diameter (0.36 mm).

The wall lift-off

The wall lift-off is an important quantity to consider when utilizing wall functions to describe boundary layers for turbulent flow. The $k-\omega$ model, utilizing wall functions, was used in this thesis, thus the wall lift-off had to be investigated. All simulation yielded similar results, thus only one example was included (see *Figure D-6* and *Figure D-7*). The results showed that the wall lift-off in viscous units was 11.06 everywhere, which was recommended by *COMSOL*. On the other hand, the wall lift-off, which should be much smaller than the geometry of the problem ($D = 3.0\,mm$), was quite large in all parts of the stenosis models except for the stenosis region and directly downstream of the stenosis outlet.

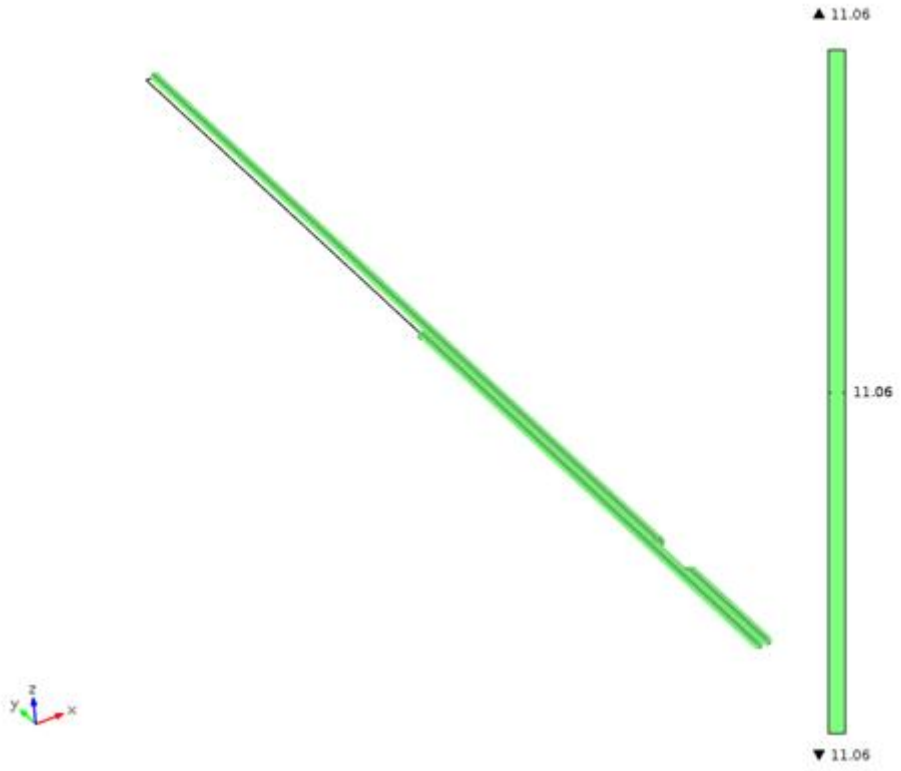

Figure D-6: The wall lift-off in viscous units for the turbulence $k-\omega$ model simulations.

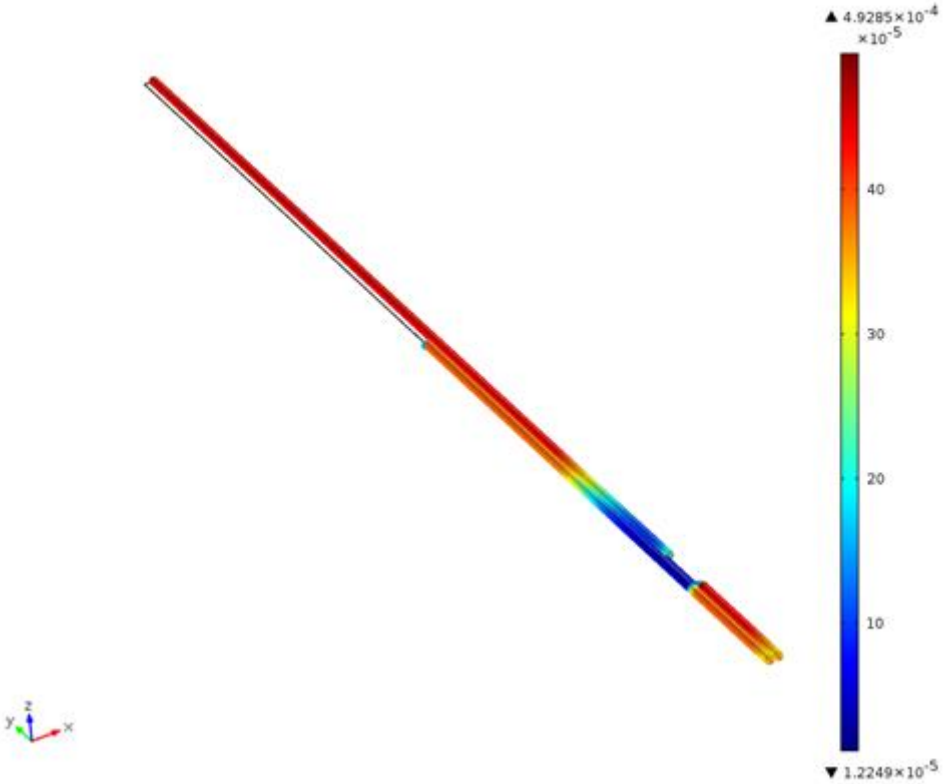

Figure D-7: The wall lift-off (in meters) for a typical turbulence $k-\omega$ model simulation.

The moving catheter

During the experimental measurements of the pressure along the stenosis models, the catheter had to be repositioned for each measurement, since the catheter sensor only had one specific sensor point. However, for the CDF simulations it was desirable to keep the catheter stationary in the position corresponding to the final measurement point (see *Figure 3.1-3*) in order to minimize the computational time needed for the simulations. For this reason, the pressure behavior along one of the three stenosis models was compared for stationary and moving catheter simulations (*Figure D-8*). For the moving catheter simulations, the pressure values were documented at the point of the sensor, i.e. 3.05 centimeters from the endpoint of the catheter, for all measurement points. For the stationary catheter simulations, the pressure was measured in a continuous central line along the stenosis model. The results were very similar for both simulations, thus the stationary catheter approach was used throughout.

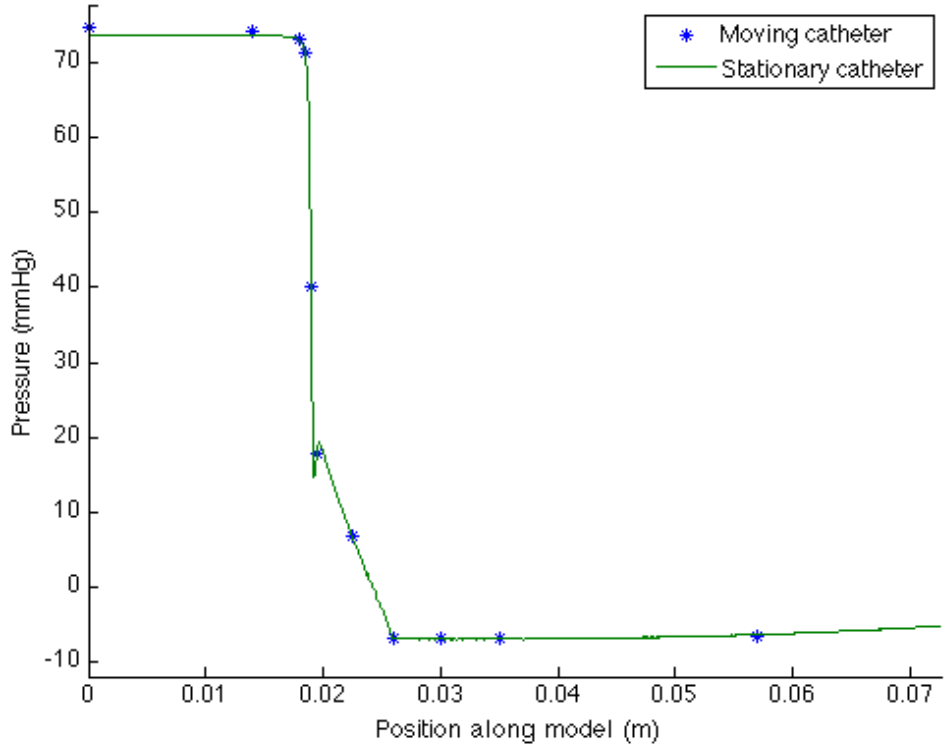

Figure D-8: Pressure along the 1.0 mm artery stenosis model for both stationary and moving catheter simulations. The flow rate was 129 ml/min.

Appendix E

Pulsatile flow measurement data

The experimental results for the pulsatile flow measurements are presented in *Table E-1* to *Table E-6*, the first table containing flow rate data and the other five containing pressure data. All pressure values, in every measurement point, are averages of six measurements (from six series of measurements).

Table E-1: Flow rate data for the pulsatile flow measurements.

Model stenosis	Mean flow rate (ml/min)	Standard deviation mean flow rate (ml/min)
Artery model 1.0 mm	128.75	1.07
Aqueduct model smooth inlet	129.91	1.56
Aqueduct model abrupt inlet	130.65	0.88
Aqueduct model smooth inlet	173.00	1.33
Aqueduct model abrupt inlet	171.63	1.31

Table E-2: Pressure data for the aqueduct model (smooth stenosis inlet) measurements under pulsatile flow. Mean flow rate was 130 ml/min.

Position along model (mm)	Systolic catheter pressure (mmHg)	Diastolic catheter pressure (mmHg)	Mean catheter pressure (mmHg)	Systolic-diastolic difference (mmHg)	Standard deviation mean pressure (mmHg)
8.5	79.2	40.0	59.6	39.2	1.1
18.5	78.3	40.2	59.3	38.2	1.4
26.8	79.0	40.2	59.6	38.8	1.8
28.5	72.0	36.2	54.1	35.8	7.0
32.0	13.7	6.7	8.8	7.0	1.2
35.5	0.5	- 3.5	- 2.8	4.0	2.9
38.5	- 4.7	-12.8	- 8.8	8.2	3.0
43.5	- 1.3	- 5.8	- 3.6	4.5	1.1
48.5	1.0	- 0.7	0.2	1.7	0.7
53.5	1.5	- 0.3	0.6	1.8	0.8

Table E-3: Pressure data for the aqueduct model (abrupt stenosis inlet) measurements under pulsatile flow. Mean flow rate 131 ml/min.

Position along model (mm)	Systolic catheter pressure (mmHg)	Diastolic catheter pressure (mmHg)	Mean catheter pressure (mmHg)	Systolic-diastolic difference (mmHg)	Standard deviation mean pressure (mmHg)
2.0	80.0	40.5	60.3	39.5	1.7
12.0	79.3	39.7	59.5	39.7	0.9
22.0	80.8	41.7	61.3	39.2	1.9
25.5	8.0	2.0	5.0	6.0	2.1
29.0	- 1.3	- 7.7	- 4.5	6.3	1.9
30.7	- 1.7	- 8.3	- 5.0	6.7	1.6
33.7	- 0.5	- 6.3	- 3.4	5.8	1.6
38.7	2.8	- 0.3	1.3	3.2	1.7
43.7	2.8	0.5	1.7	2.3	1.3
56.0	2.5	0.3	1.4	2.2	1.0

Table E-4: Pressure data for the 1.0 mm artery stenosis model measurements under pulsatile flow. Mean flow rate 129 ml/min.

Position along model (mm)	Systolic catheter pressure (mmHg)	Diastolic catheter pressure (mmHg)	Mean catheter pressure (mmHg)	Systolic-diastolic difference (mmHg)	Standard deviation mean pressure (mmHg)
0.0	94.5	51.3	72.7	43.2	1.4
14.0	94.7	51.3	72.3	43.3	2.2
19.0	96.8	54.2	74.0	42.7	2.3
22.5	11.8	5.7	8.3	6.2	1.8
26.0	- 2.5	- 7.7	- 6.3	5.2	1.7
57.0	1.2	- 1.0	0.0	2.2	0.0

Table E-5: Pressure data for the aqueduct model (smooth stenosis inlet) measurements under pulsatile flow. Mean flow rate 173 ml/min.

Position along model (mm)	Systolic catheter pressure (mmHg)	Diastolic catheter pressure (mmHg)	Mean catheter pressure (mmHg)	Systolic-diastolic difference (mmHg)	Standard deviation mean pressure (mmHg)
8.5	113.2	71.2	92.0	42.0	3.0
18.5	112.7	71.0	91.3	41.7	3.1
26.8	113.2	71.8	92.3	41.3	3.6
28.5	107.2	68.6	88.2	38.6	3.3
32.0	19.7	12.2	16.0	7.5	3.2
35.5	- 4.0	- 9.2	- 6.5	5.2	0.8
38.5	- 7.2	- 17.2	- 11.7	10.0	3.8
43.5	- 2.7	- 9.3	- 6.0	6.7	3.5
48.5	1.3	- 1.2	0.3	2.5	0.5
53.5	1.0	- 0.8	0.2	1.8	0.8

Table E-6: Pressure data for the aqueduct model (abrupt stenosis inlet) measurements under pulsatile flow. Mean flow rate 172 ml/min.

Position along model (mm)	Systolic catheter pressure (mmHg)	Diastolic catheter pressure (mmHg)	Mean catheter pressure (mmHg)	Systolic-diastolic difference (mmHg)	Standard deviation mean pressure (mmHg)
2.0	116.7	72.5	94.3	44.2	2.0
12.0	115.5	72.2	93.6	43.3	1.9
22.0	119.8	78.2	99.1	41.7	5.5
25.5	9.2	3.2	6.2	6.0	1.7
29.0	- 7.3	- 13.7	- 10.3	6.3	2.0
30.7	- 7.5	- 15.7	- 11.3	8.2	1.5
33.7	- 3.3	- 11.3	- 7.3	8.0	1.6
38.7	0.7	- 3.0	- 1.2	3.7	1.5
43.7	0.7	- 1.0	- 0.2	1.7	1.2
56.0	0.5	- 1.3	- 0.4	1.8	1.3

Constant flow measurement data

The pressure drops for the constant flow measurements, corresponding to *Figure 4.1-7* through *Figure 4.1-10*, are presented in *Table E-7* to *Table E-10*. All constant flow measurements were performed with the catheter pressure sensor. The resulting pressure drops for the CFD simulations are also included.

Table E-7: The total pressure drop over the 1.0 mm artery stenosis model for a set of constant flow rates. Both the experimental and CFD results are presented. Flow rates are presented by the measured mean value (± standard deviation).

Flow rate (ml/min)	Experimental pressure drop (mmHg)	Pressure drop, laminar model (mmHg)	Pressure drop, turbulence model (mmHg)
57.55 (±1.21)	12.0	20.4	12.5
118.75 (±1.27)	64.0	64.8	49.5
149.59 (±1.55)	92.0	95.8	77.7
193.98 (±1.35)	144.0	152.2	127.9

Table E-8: The total pressure drop over the 1.5 mm artery stenosis model for a set of constant flow rates. Flow rates are presented by the measured mean value (± standard deviation).

Flow rate (ml/min)	Experimental pressure drop (mmHg)	Pressure drop, laminar model (mmHg)	Pressure drop, turbulence model (mmHg)
56.11 (±0.93)	-3.0	3.6	1.7
117.70 (±1.16)	8.0	8.9	6.5
169.11 (±0.84)	16.0	15.9	12.8
195.65 (±0.51)	20.0	20.4	17.0
235.90 (±1.41)	28.0	28.1	24.2
273.73 (±3.08)	43.0	36.4	32.4

Table E-9: The total pressure drop over the aqueduct model (smooth stenosis inlet) for a set of constant flow rates. Flow rates are presented by the measured mean value (± standard deviation).

Flow rate (ml/min)	Experimental pressure drop (mmHg)	Pressure drop, laminar model (mmHg)	Pressure drop, turbulence model (mmHg)
56.45 (±1.37)	13.0	19.6	11.9
63.33 (±1.00)	17.0	23.4	14.8
125.50 (±1.06)	51.0	70.0	54.0
179.33 (±2.00)	99.0	130.6	106.1

Table E-10: The total pressure drop over the aqueduct model (abrupt stenosis inlet) for a set of constant flow rates. Flow rates are presented by the measured mean value (± standard deviation).

Flow rate (ml/min)	Experimental pressure drop (mmHg)	Pressure drop, laminar model (mmHg)	Pressure drop, turbulence model (mmHg)
54.88 (±1.00)	13.0	18.6	10.8
63.67 (±1.32)	15.0	23.6	14.4
108.50 (±0.80)	42.0	56.8	41.8
120.00 (±0.5)	50.0	66.9	50.6
149.82 (±1.08)	72.0	99.4	79.1
181.67 (±2.18)	109.0	142.0	116.0

Appendix F

Polynomial fit for the constant flow measurements

The polynomial approximation made to the constant flow rate measurements are presented in *Figure F-1* to *Figure F-4*, including residuals and norm of the residuals corresponding to the polynomial fit. It should be noted that the polynomial in *Figure F-4* was fit to badly distributed points that most certainly explains the smaller error residuals compared to the polynomial fits in *Figure F-1* to *Figure F-3*.

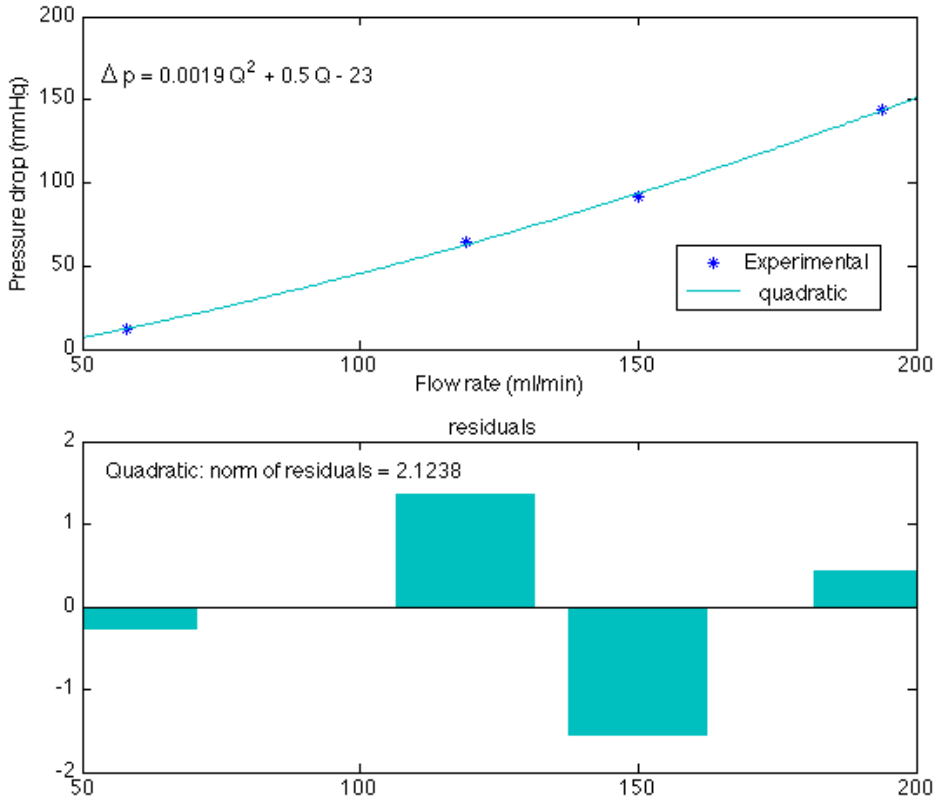

Figure F-1: The pressure drop vs. flow rate for the 1.0 mm artery model and the corresponding quadratic fit with residuals. The coefficient of determination, R^2, was 0.9995 for the quadratic fit.

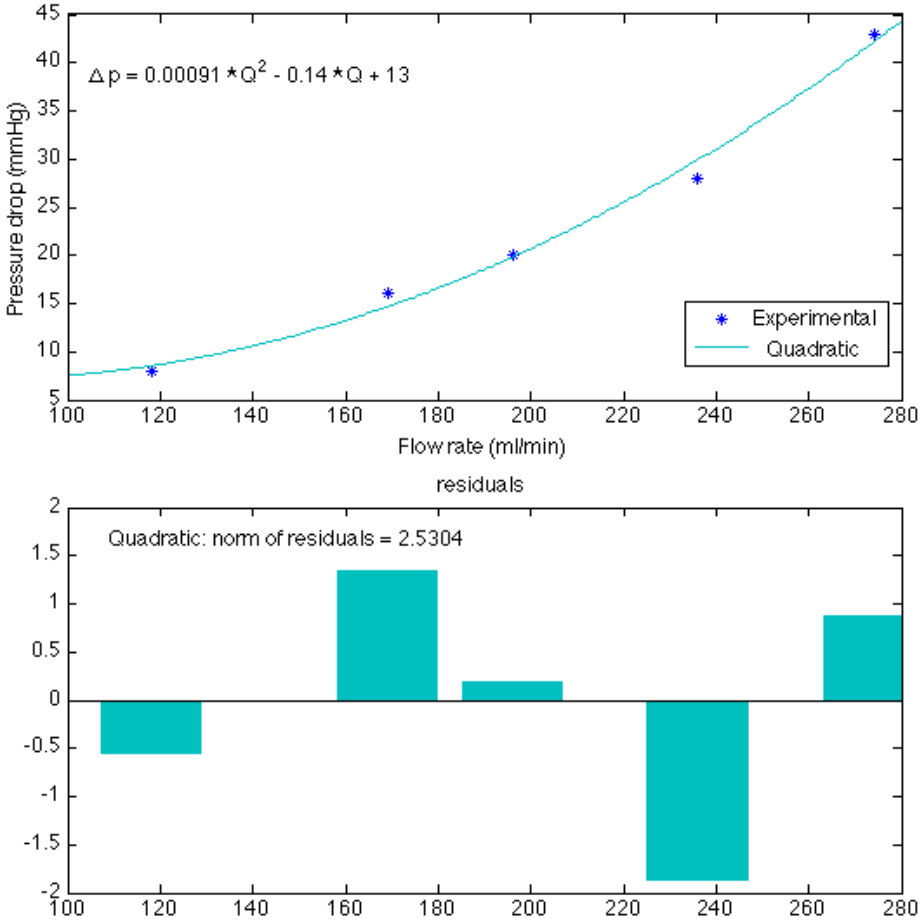

Figure F-2: The pressure drop vs. flow rate for the 1.5 mm artery model and the corresponding quadratic fit with residuals. The coefficient of determination, R^2, was 0.9910 for the quadratic fit.

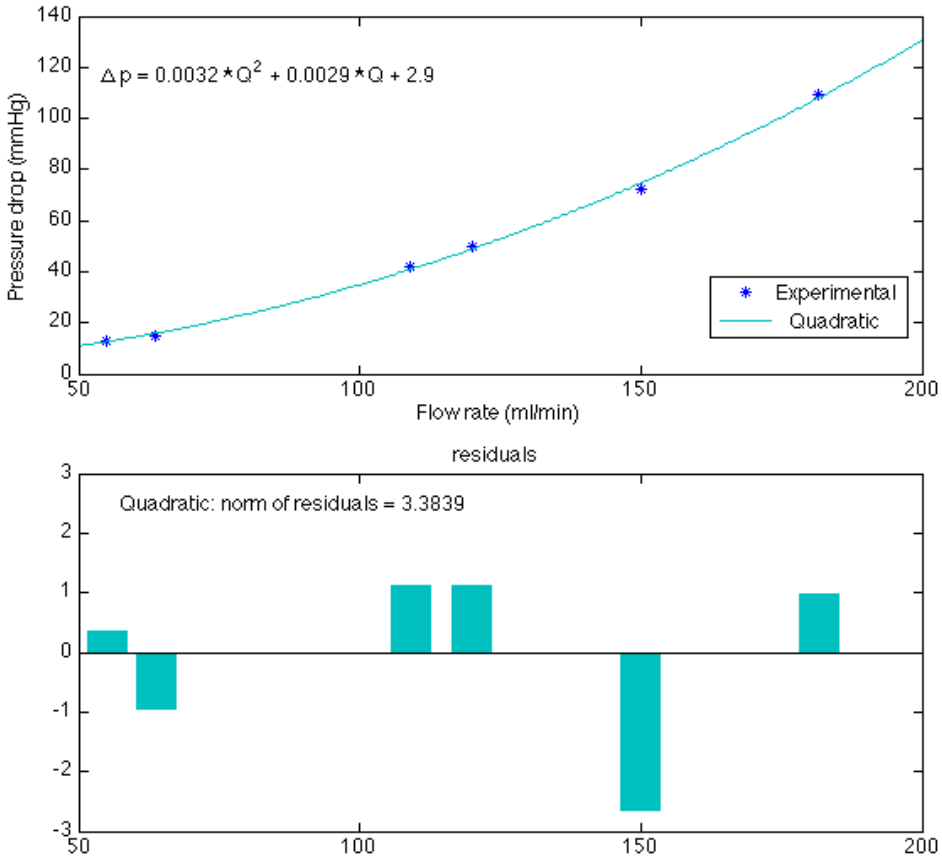

Figure F-3: The pressure drop vs. flow rate for the aqueduct model (abrupt stenosis inlet) and the corresponding quadratic fit with residuals. The coefficient of determination, R^2, was 0.9983 for the quadratic fit.

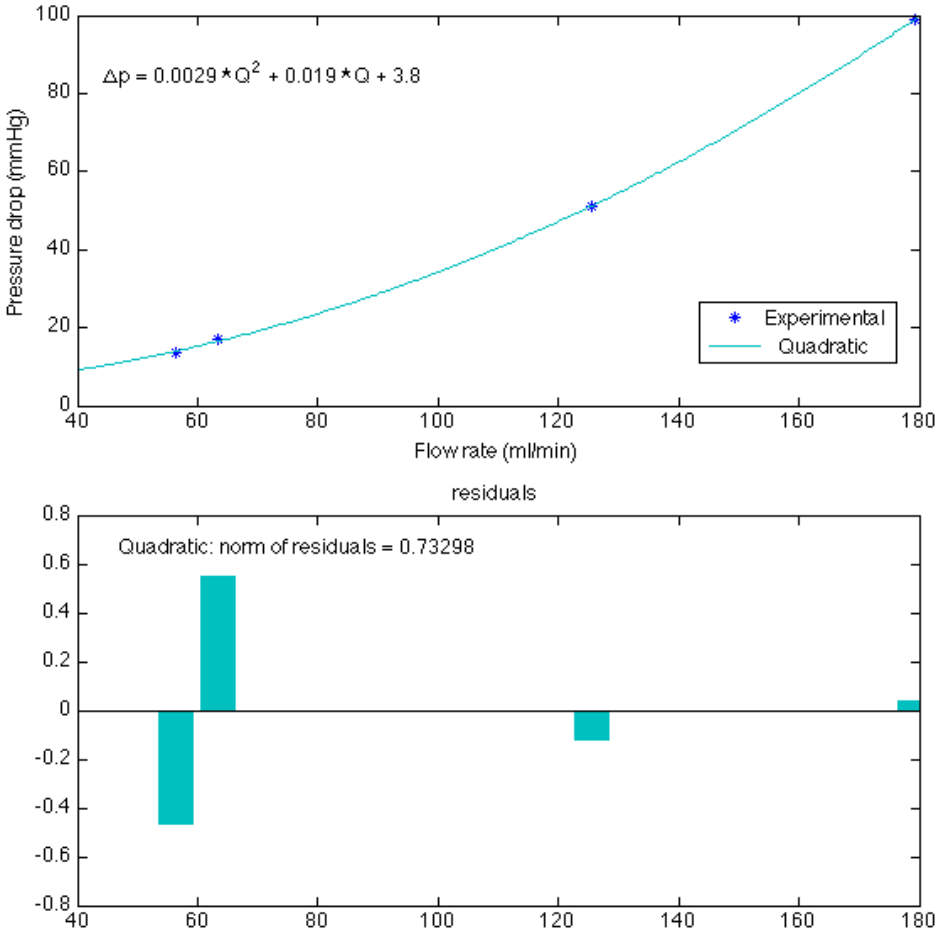

Figure F-4: The pressure drop vs. flow rate for the aqueduct model (smooth stenosis inlet) and the corresponding quadratic fit with residuals. The coefficient of determination, R^2, was 0.9999 for the quadratic fit.